Gas Phase Preparation of Magnetic Nanoparticle Hydrosols

Thesis submitted for the degree of

Doctor of Philosophy

at the University of Leicester

by

Sıtkı Aktaş

Condensed Matter Physics Group

Department of Physics and Astronomy

University of Leicester

2014

Gas Phase Preparation of Magnetic Nanoparticle Hydrosols

Sıtkı Aktaş

Abstract

The main purpose of this work was to produce nanoparticles with a pure iron core, a narrow size distribution and a high saturation magnetisation in order to improve their effectiveness in the hyperthermia treatment of tumours and in Magnetic Resonance Imaging (MRI) diagnosis.

Gas phase Fe nanoparticles in a liquid suspension have been produced by co-deposition with water vapour in ultra-high vacuum (UHV) conditions. The water was injected from outside the vacuum as a molecular beam onto a substrate maintained at 77 K and formed an ice layer with a UHV compatible vapour pressure. Various coating ligands were added to the injected water in an attempt to stabilise the nanoparticle hydrosols.

Transmission Electron Microscopy (TEM) images confirmed that the nanoparticles had a pure iron core with a thin oxide shell and a narrow size distribution with the most probable diameter of either 8.55 or 16 nm depending on the source conditions. It was found that short chain molecules are more effective in stabilising the gas phase nanoparticles. The size distribution of the nanoparticles in liquid suspensions analysed by a Nanosight LM10 particle sizer showed that, of the ligands tested, sorbitol and DMSA are the most suitable to prevent the agglomeration of the gas phase produced hydrophobic nanoparticles. UV-visible spectral measurements showed that DMSA coated nanoparticles transform into an oxide in a short time. In addition, a magnetometry study of sorbitol-coated iron nanoparticles showed that oxidation of the nanoparticles erodes the pure iron core to about 5 nm diameter in two months.

MRI measurements of the sorbitol-coated iron nanoparticles show that their relaxivity is five times higher than commercial iron oxide nanoparticle suspensions (Resovist®). On the other hand, specific absorption rate (SAR) measurements of the nanoparticles by two different designs of heating coils were not accurate due to the low concentration of nanoparticle in solution. Hence, the heating performance of the nanoparticles was determined theoretically using a new model published by Vallejo-Fernandez [Vallejo-Fernandez 2013], which includes the heating mechanisms active over the whole size range of particles. The results show that the SAR of the pure iron core nanoparticles is significantly higher than iron oxide nanoparticles.

Core-shell nanoparticle can also be produced in the gas phase by passing the core nanoparticles through hot crucible loaded with the shell material under UHV conditions. Composite Fe@FeO-Ag nanoparticles which can be used for multifunctional medical applications have been produced. It was also found that heating the nanoparticles in the gas phase using the empty crucible enabled the control of the nanoparticles' shapes, which was found to change their MRI relaxivity.

Acknowledgments

First and foremost I would like to express my deepest gratitude to my supervisor Professor Chris Binns for his excellent guidance, caring, patience, and providing me with an excellent atmosphere for doing research. I would like to thank Dr. Steve Baker for his insightful comments and suggestions.

Special thanks to Mr Stuart Thornton who as a good friend, was always willing to help and give his best suggestions. It would have been a lonely lab without him...

I warmly acknowledge all members of CMP group and Department of Physics and Astronomy for friendship.

I want to thank Dr.Leonardo Lari and Dr. Roland Kröger for high-quality TEM images and NCSR Demokritos in Greece for magnetic measurements.

I sincerely thank Turkish Ministry of National Education for providing me with a scholarship to carry out this research. I am also grateful to my beloved friends for their support in Leicester.

To my parents who are the most dearest to me with their unequivocal support and prayers. I also thank my beloved brothers and sisters, Hatice, Necati, Naci, Fatma and İbrahim, for their moral support.

Last, but not least, my heartfelt appreciation goes to my wife, Gül; without her love and support, it would not have been possible to write this thesis.

This thesis is dedicated to my beloved wife,
Gül
for her love, endless support
and encouragement

Contents

List of Figures

List of Tables

Chapter 1

Introduction

In the last few decades, despite intensive research with some success in treatment, cancer has the highest mortality rate in most countries [Salunkhe 2014]. Comparison of the death rate from cancer, normalised to the increased life expectancy with the other major illnesses (heart disease, stroke and influenza) shows that the probability of a person dying of cancer today is the same as fifty years ago [Davies 2013]. The standard cancer therapies are based on surgery, chemotherapy, irradiation and combinations of all of these. However, there are some acute physiological side effects of these treatment techniques on the patient. Therefore intensive research has been carried out to find alternate treatment techniques to reduce or eliminate side effects on patients by using nanotechnology.

Magnetic nanoparticles with diameters in the range 1-100 nm have attracted great interest in interdisciplinary research due to their unique properties which are very different from the bulk material. In particular they have attracted significant interest in medicine to solve certain persistent problems in conventional diagnosis and treatment. For example, to carry drugs to specific parts of the body, by applying an external field to drug-loaded magnetic nanoparticles, which can be delivered to a specific place without any side effects [Dobson 2006]. Also, in Magnetic Particles Imaging (MPI) which is a new imaging technique, by using the response of the magnetic nanoparticles to an applied field it is possible to probe their concentration in the body [Weizenecker 2009, Binns 2014 b]. Magnetic nanoparticles can also be used as contrast agents in Magnetic Resonance Imaging (MRI) [Pankhurst 2009]. Furthermore, magnetic

nanoparticles have an important ability in cancer treatment by heating the tumour in response to an applied alternating magnetic field, which is called Magnetic Nanoparticle Hyperthermia (MNH) [Binns 2012, Pankhurst 2009].

Hyperthermia refers to an abnormally high body temperature, which is often caused by illnesses. Besides this it refers to treatment by artificially produced heat. Hyperthermia is used to increase the temperature of a living organism sufficiently high to damage and kill the cancer cells or make them weaker against the standard therapies. Since tumours have poor blood flow, they are more acidic due to the lack of oxygen. Therefore tumour tissues tend to be more susceptible to heat shock than healthy tissues.

The concept of using the hyperthermia is not new. The first medical textbook, the Edwin Smith Surgical papyrus, written more than 5000 years ago, involves a description of a patient with a tumour in the breast treated with hyperthermia [Nielsen 2001]. Also Hippocrates (479-377 B.C) pointed out the importance of the hyperthermia treatment with his following saying "*Those who cannot be cured by medicine can be cured by surgery. Those who cannot be cured by surgery can be cured by fire [hyperthermia]. Those who cannot be cured by fire, they are indeed incurable."* [DeNardo 2008]. Also, the effect of increasing the body temperature (hyperthermia) on cancer treatment was reported by de Kizowitz in 1779 and Busch in 1866 [Roussakow 2013].

The historical use of hyperthermia involved heating the whole body, which is very dangerous, while more, recently various methods have been developed to focus heat at the tumour site such as ultrasound, microwaves, etc. [DeNardo 2008]. Additionally, radiofrequency probes or "thermo seeds" have been inserted into cancers by surgery to increase the local temperature without damaging the healthy tissues. In 1957, 20-100

nm iron oxide nanoparticles were injected into the lymphatic channels to treat metastatic cancer in lymph nodes [Gilchrist 1957]. Thanks to this work further research has been carried out in cancer treatment by using the combination of the magnetic nanoparticles and an Applied Magnetic Field (AMF).

In general, MNH uses magnetic nanoparticles which have several layers such as a magnetic core coated with a layer to stabilise the nanoparticles in suspension and a further shell with biological targeting molecules to bind selectively to tumour cells and protect them from the immune system [Binns 2012]. The nanoparticles are placed in tumour tissue and are heated in an alternating magnetic field, from the normal human body temperature of 36-37º C to 42º C or more, in order to kill the tumour [Binns 2010]. This approach can destroy the tumours with minimal damage to healthy tissues and, therefore, limit negative side effects.

The first time magnetic nanoparticles were used for hyperthermia treatment combined with external beam radiotherapy for human clinical trials was in 2007 to treat brain cancer in 14 patients [Maier-Hauff 2007]. The magnetic nanoparticles used in the treatment were 12 nm magnetite nanoparticles with an Fe concentration of 112 mg/ml. The amplitude of the AMF was between 2-15 kA/m with a frequency of 100 kHz. In 2010 the second clinical trial was carried out on 59 patients [Maier-Hauff 2011]. The results show that life expectancy was increased with MNH treatment compared with the standard treatment. Also some clinical trials were carried out for prostate cancer [Johannsen 2010]. The clinical trials showed that the main problem of the treatment was the difficulty of producing a sufficiently high temperature rise throughout the whole tumour.

The clinical application of MNH showed there are no negative side effects with the treatment. However, the main restriction of the method is that the nanoparticles used do not generate sufficient heat. Generally iron oxide nanoparticles are favoured for hyperthermia treatment due to their biocompatibility. However, their ability to produce heat is limited by their low saturation magnetisation (see chapter 5). The heating efficiency of available magnetic nanoparticles cannot be increased by raising the magnetic field amplitude and field frequency since there is an upper limit of the field times frequency ($H\ x\ f$) product which can be safely applied to the body [Atkinson 1984].

For efficient magnetic hyperthermia, the magnetic nanoparticles are required to have a low toxicity and a high magnetization in order to minimize the doses needed for the required temperature increase. Hence, the main purpose of this project was to produce pure iron core nanoparticles, which are stabilised in a liquid suspension. These need to be coated with a biocompatible shell since Fe is highly toxic [Hergt 2006].

A number of techniques are available to produce nanoparticles with a narrow size distribution such as chemical, biological and physical methods [Binns 2012]. It is possible to produce large amounts of nanomaterials with a good size control and with a biocompatible surfactant layer by chemical method. In biological method, natural process in bacteria is used to grow nanoparticles in hydrosol (relatively cheap), however, size control over a wide range is difficult. The main disadvantage of these synthesis techniques is that the production only of oxide nanoparticles. Besides this, the high vacuum gas-phase methods is used to synthesis reactive materials in a clean environment with a good size control (1-20 nm) and remain pristine without being converted to oxide [Baker 2000].

Hence to try and overcome the problems mentioned above, pure Fe nanoparticles have been produced in gas phase under ultra-high vacuum (UHV) conditions, with two different shells (FeO_x and Ag) and the results are reported in this thesis. Pure iron core nanoparticles have a four times higher saturation magnetisation than iron oxide. So it is crucial to produce pure Fe core nanoparticles with a narrow size distribution in a liquid suspension. When the Fe nanoparticles contact with air they start to oxidise and form a biocompatible thin oxide shell which makes potentially them suitable for medical applications. Besides this, it is also possible to passivate the nanoparticles by coating them with a shell material that is biocompatible such as Ag. Coating the pure iron nanoparticles with a shell protects the magnetic core against oxidation, without a drastic reduction of the saturation magnetisation. The coating would also facilitate the attachment of biological molecules to the nanoparticles' surface.

The most useful way to understand the effectiveness of the nanoparticles in producing heat is their Specific Absorption Rate (SAR), which describes the ratio of energy converted into heat per unit time and mass (W/g). The SAR value depends strongly on the strength and frequency of the external magnetic field as well as the size and shape of the nanoparticles.

Gas phase produced magnetic nanoparticles also have great potential as MRI contrast agents due to their higher relaxation performance. In general, the relaxivity of nanoparticles depends on the size and saturation magnetisation of the nanoparticles. Resovist® is the clinically available nanoparticle suspension for MRI diagnosis. Hence producing new nanoparticles which have a higher saturation magnetisation than Resovist® is vital for more sensitive diagnosis. Also gas-phase-produced nanoparticles might be used for the diagnosis of cancer by MRI or MPI after treatment by MNH.

The structure of the thesis is as follows. In chapter 2, the method of the production of pure Fe core nanoparticles and the deposition of the nanoparticles as a liquid suspension in UHV conditions is detailed. The method of synthesis of core-shell nanoparticles and the concentration calculation for the final solution is also described. In addition the chapter shows the methods used for heating the nanoparticle suspensions to determine their SAR and to obtain the size distributions and the optical properties of the samples.

In chapter 3, the behaviour of superparamagnetic and blocked particles is reviewed with reference to basic concepts of magnetism. The heating mechanisms of the nanoparticles exposed to an alternating magnetic field and their MRI relaxivity are explained. This chapter also describes theory of the stabilisation of the magnetic nanoparticles in liquid suspensions.

In chapter 4, Transmission Electron Microscopy (TEM) analysis, stabilisation and size distribution of gas phased produced $Fe@FeO_x$ nanoparticles in liquid suspensions are presented. This chapter also describes the UV-visible optical measurements of the $Fe@FeO_x$ nanoparticles.

Chapter 5 presents the magnetic measurements of $Fe@FeO_x$ nanoparticles with MRI results. It also explains the measured and modelled SAR value of the $Fe@FeO_x$ nanoparticles produced with two different size distributions.

The last data chapter 6 presents the core-shell nanoparticle systems, when the Cu and Fe nanoparticles were coated with Ag shells. Beside in situ analyses of the shell thickness with the quadrupole mass filter, TEM analyses were also employed to determine the shell thickness and final structure of the nanoparticles. Shape control of the nanoparticles and its effect on their magnetic properties is introduced as well.

Finally the conclusions and future work are presented in chapter 7.

CHAPTER 2

Experimental and Measurement Techniques

This chapter presents details about the technique used for the production of magnetic nanoparticles and the measurement techniques used to characterise these nanoparticles. The liquid suspensions of magnetic nanoparticles were produced by using an ultra-high vacuum (UHV) compatible sputter gas aggregation source (Superb Leicester University Mesoscopic Particle Source-SLUMPS). The magnetic heating tests of the nanoparticle suspension were carried out using radio frequency heating (RF heating). The size distributions of suspension were determined by a Nanosight LM10 instrument. UV-visible absorption spectra of liquid suspensions were determined by a Thermo Scientific Evolution 220 UV-visible Spectrophotometer.

2.1 Sample Synthesis

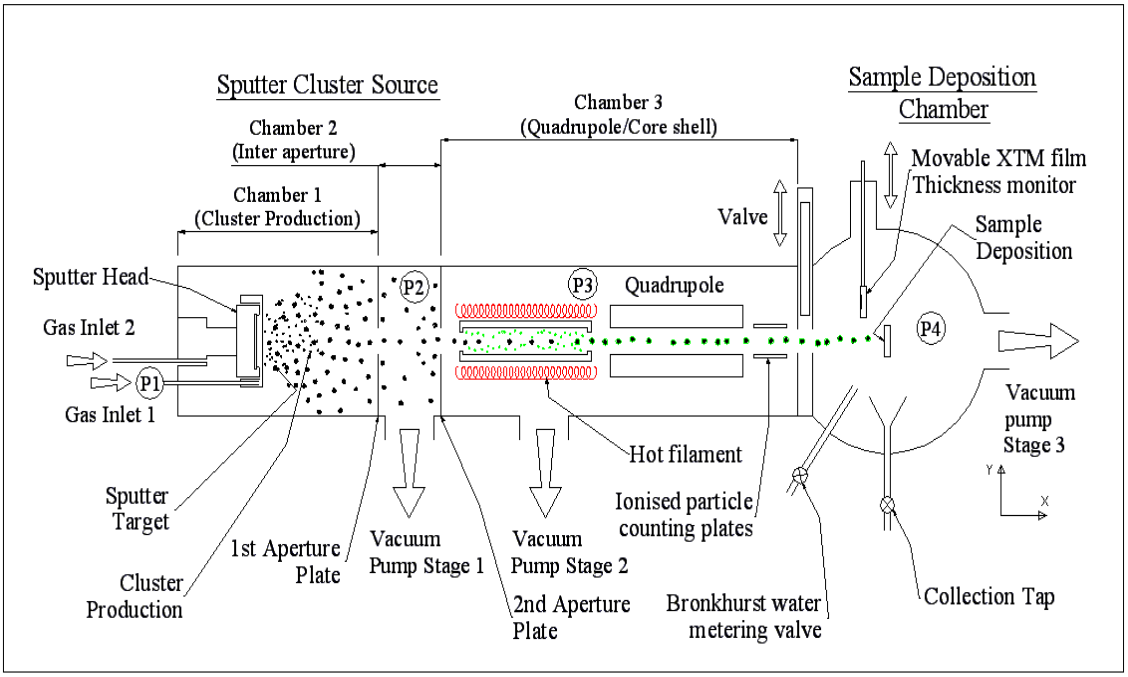

Figure 2.1 Schematic diagram of SLUMPS. For details, see text.

SLUMPS is the in-house gas aggregation source capable of producing clean nanoparticles in the size range of 5-15 nm with a narrow size distribution [Binns 2012]. It is based on the NCU200 source built by Oxford Applied Research Ltd and its design is similar to the original sputter nanoparticle source reported by Haberland et al [Haberland 1992]. It consists of a dc magnetron sputtering unit and an aggregation region, a shell evaporator for core-shell nanoparticle production, a quadrupole mass filter, two parallel ionised particle counting plates and a deposition chamber. The schematic diagram of SLUMPS is displayed in figure 2.1 and a photograph is shown in figure 2.2. The UHV condition is obtained by using three turbo molecular pumps (Edward STPA 1303C), backed by three scroll pumps (Edward XDS35i) (see figure 2.2). When the source is operating, these pumps create a pressure gradient delineated by four characteristic pressures (P_1, P_2, P_3 *and* P_4) indicated in figure 2.1.The main parts of the SLUMPS and the method to produce nanoparticles suspended in liquid suspensions are described below.

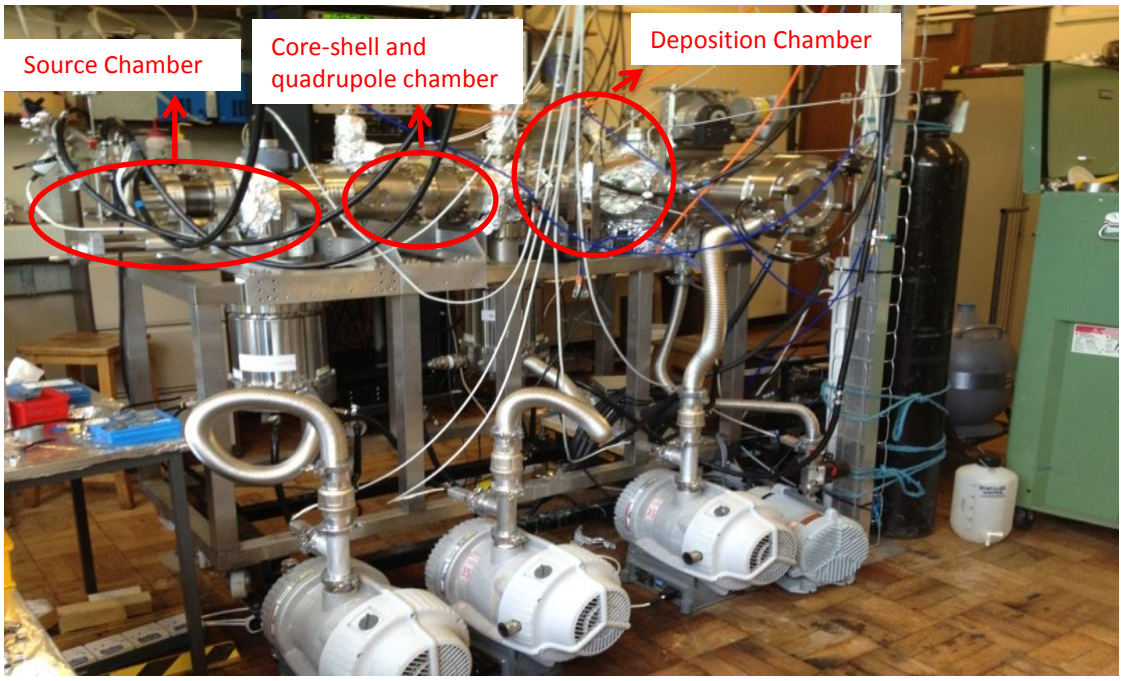

Figure 2.2: View of SLUMPS showing; three turbo pumps backed by three scroll pumps used to provide UHV conditions throughout the source.

2.1.1 Cluster Production

The magnetron gas aggregation technique forms nanoparticles of the desired size by employing magnetron sputtering at a relatively high Ar pressure (~ 1 mbar) to generate an atomic vapour from a target, which condenses into clusters in the Ar. The cluster source consists of a dc sputtering unit, a linear motion drive to adjust the length of the aggregation region and an aperture through which clusters emerge and form a free beam in high vacuum.

2.1.1.1 DC Magnetron Sputtering

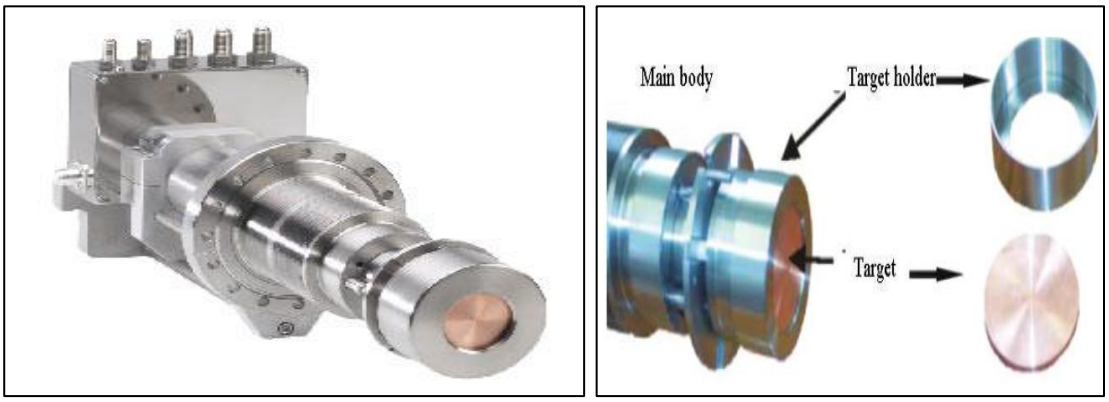

(a) (b)

Figure 2.3: (a) An external view of the NC200U source. (b) Target arrangement inside the magnetron.

An NCU 200 nanocluster source was employed for producing nanoparticles. Figure 2.3 (a) shows an external view of the water-cooled magnetron sputter head. A target disc (Fe ~ purity of 99.8%) of diameter 50.8 mm and 0.5 mm thickness is mounted into the magnetron and target holder attached (figure 2.3 (b)) to act as a clamp. Finally, an earthed outer can is attached with a 0.3 mm gap from the target. After introducing Ar (purity of 99.999%) around the target, a dc voltage (between 180 to 195 V, 20 to 25 W) is applied between the target (cathode) and outer can (anode). This ionises argon atoms and accelerates them onto the target surface which dislocates atoms from the target to

produce a vapour. The process produces secondary electrons, which maintain the plasma. A magnet situated behind the target is used to confine the secondary electrons and Ar ionisation producing a focused sputtering region and an increased efficiency of sputtering. The released target atoms travel with the gas flow into the aggregation chamber. Molecular Dynamic simulations [Binns 2012] have shown that the typical velocity of nanoparticles is approximately 50 ms^{-1}.

2.1.1.2 Gas Aggregation

Two gas inlets are used to introduce Ar gas to the sputter head and aggregation region in order to improve the efficiency of production of clusters and their removal from the aggregation region. Ar gas is injected from one of the gas inlets via a leak valve to directly above the target. The Ar flow is controlled by adjusting the P_1 pressure, which is monitored by a pirani gauge connected to just before the leak valve, in the range 35-50 mbar. The second gas inlet is placed behind the target and its pressure is monitored by observing pressure P_3. Due to the design of our sputter head we cannot measure the real operating pressure so gauge pressure at P_1 is used as a comparator to set up the system. Hence the real operator pressure in aggregation region is of the order of 0.5 to 2 mbar. During the particle growth, the length of the aggregation region varies between the 40 to 112 mm. Owing to the high proportion of the surface atoms on the clusters, during the formation process; they are very reactive so they have to be produced in an ultra-clean environment. In order to obtain UHV pressure before starting the particle production, all chamber are baked out during two days. Hence without Ar introduced, SLUMPS rests at a background pressure in the UHV region ($3x10^{-9}$ mbar or better).

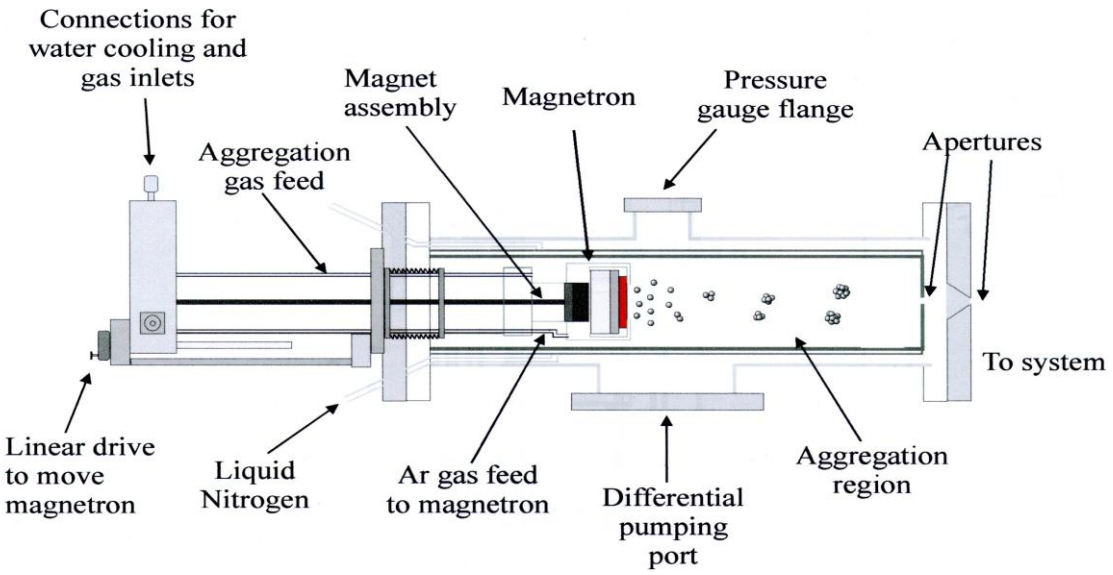

Figure 2.4: Schematic overview of the nanocluster source and its main components.

The nanoparticle source has cooling water maintained at ~15 ºC piped to the target and to the wall of the condensation chamber. Alternatively, liquid nitrogen can be used for cooling [Haeften 2009] . The length of the aggregation region can be adjusted by means of a linear drive to move the magnetron as shown in figure 2.4. This varies the aggregation length and the residence time within the aggregation region, which enables control of the cluster size distribution [Banerjee 2008].

Just after the sputtering process, the liberated atoms have a large kinetic energy which must be reduced to commence the cluster formation. This is achieved by repeated collisions between the sputtered atoms and aggregation gas (Ar). The initial nucleation of the nanoparticles requires three-body collisions where the heat of bonding of the metal atoms is carried away by an Ar atom.

The clusters travel with the gas flow to the first and second aperture because of the pressure gradient. The pressure between first and second aperture (P_2), chamber 2, is about 10^{-3} mbar during the sputtering process and is monitored by a penning gauge.

2.1.2 Shell Evaporator to form Core-Shell Nanoparticles

After passing through the second aperture, clusters enter the shell evaporator. This is a heated crucible open at both ends and aligned axially with the cluster beam that coats the core material with a shell of another material in the gas phase in UHV-clean conditions. Before the coating procedure, the empty alumina crucible was placed in the shell evaporator and the system was pumped down to approximately 10^{-8} mbar. The crucible was then heated to a higher temperature than required to evaporate the shell material in order to outgas the crucible. After that the system was vented and the crucible filled with the shell material. The crucible is wound with a heating element and surrounded by heat shields and a water tank as illustrated in figure 2.5.

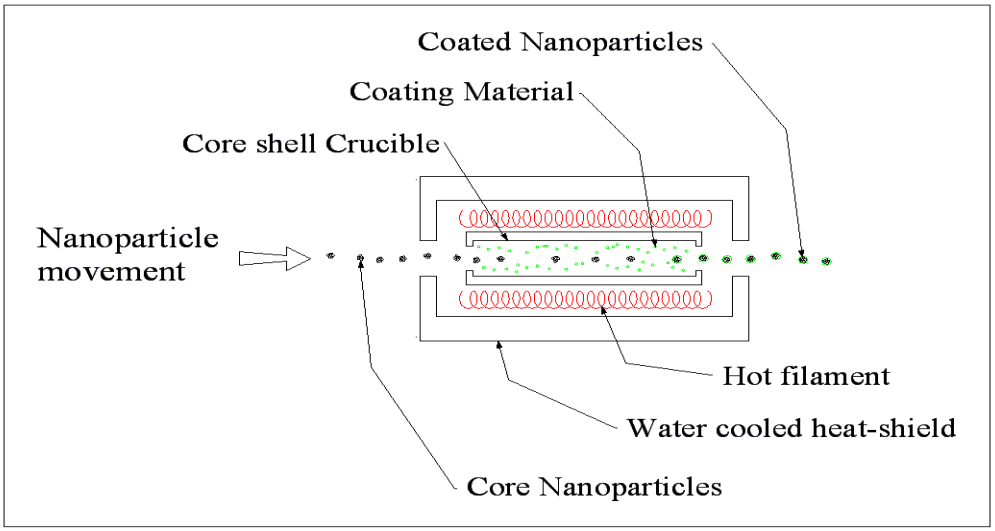

Figure 2.5: Illustration of the method of making core-shell nanoparticles.

In the shell coating process, any material can be used if it can be evaporated in vacuum at a suitable temperature. The vapour pressure of the shell material is controlled by the temperature of the crucible. The thickness of the shell is calculated from the increase in mass of the core particles, which is detected by using an ultra-high mass quadrupole mass filter.

2.1.2.1 Calculation of the Thickness of the Shell Material

The thickness of the shell material can be calculated using the mass spectrum of the core nanoparticles and after coating with the shell material (see figure 2.6). The black data represents the mass spectrum of the core nanoparticles, which is recorded with the shell evaporator cold. The red data shows the mass spectrum of the core-shell nanoparticles with the crucible temperature increase to the desired value. Using the shift of the two mass spectra, the shell thickness can be calculated as illustrated below.

Firstly, the diameter of the core nanoparticle needs to be determined. From the mass spectrum the core material mass is given by,

$$m = \frac{M_{core}}{N_A \times 10^3} \text{ (kg)} \qquad 2.1$$

where m (kg) is the mass of the core nanoparticle, M_{core} (Daltons) is the observed peak of the mass spectrum (see figure 2.6) and N_A is the Avogadro number, which is $6.02214129 \times 10^{23}$ mol^{-1}.

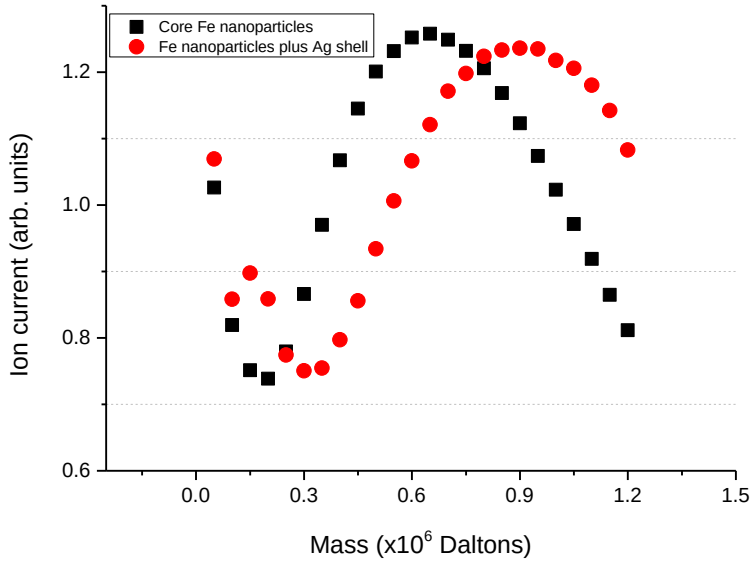

Figure 2.6: Mass spectrum of the core Fe and Fe@Ag core-shell nanoparticles obtained using the quadrupole mass filter.

The volume of the core material (V_{core}) is determined by the equation,

$$V_{core} = \frac{m}{\rho} (\mathrm{m}^3) \quad 2.2$$

where ρ is the bulk density of the core material. The diameter of the nanoparticles is calculated using equation 2.3.

$$d_{core} = (\frac{6V_{core}}{\pi})^{1\ 3} \quad 2.3$$

From the difference in the peak of the mass spectra of core and core-shell materials, the mass of the shell is given by

$$m = (\frac{M_{(core-shell)} - M_{core}}{N_A \times 10^3}) \quad 2.4$$

The volume of the shell (V_{shell}) material is determined using equation 2.2; however, the shell material bulk density should be used. The total volume of the core-shell nanoparticle is given by

$$V_{core-shell} = V_{core} + V_{shell} \quad 2.5$$

The diameter of the core-shell nanoparticles ($d_{(core-shell)}$) is determined by equation 2.3 and the thickness of the shell material is given by

$$thickness\ of\ the\ shell\ material = d_{(core-shell)} - d_{core} \quad 2.6$$

2.1.3 Quadrupole Mass Filter

A home built quadrupole mass filter was used to analyse and filter charged particles from the NC200U nanocluster source. During the filtering process, the flux of the nanoparticles decreased so the quadropule was only used to measure the mass spectrum of the gas phase nanoparticles before the deposition. Mechanically the quadrupole

assembly is composed of four rods and a detector plate on which the cluster ion current can be measured as illustrated in figure 2.7.

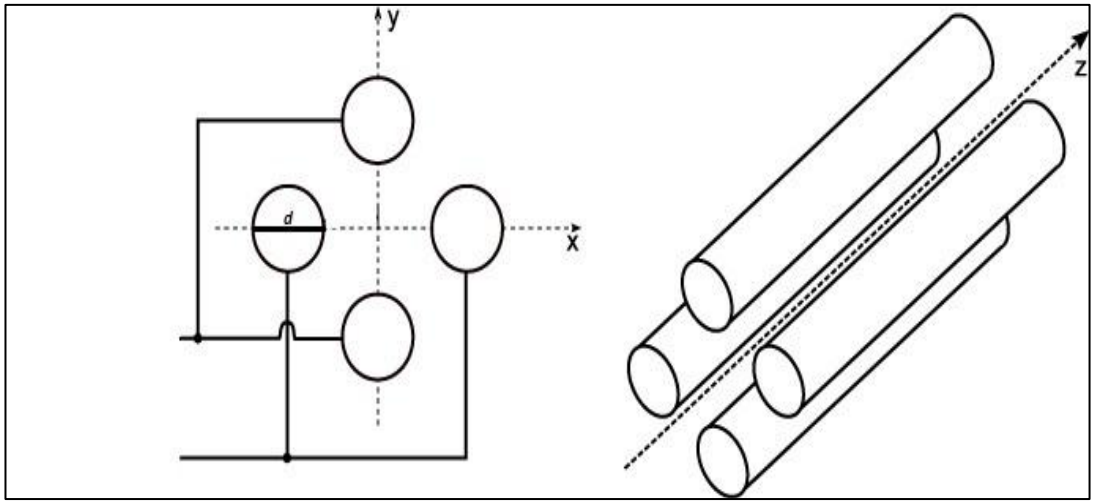

Figure 2.7: Schematic view of quadrupole assembly which is composed of four rods. The opposite rods are electrically connected each other.

The opposite rods are electrically connected to each other. A voltage which has a dc and ac component (of frequency f), $U + V\cos 2\pi ft$ is applied to one pair of poles and the negative (- $U - V\cos 2\pi ft$) is applied to the other pair (see figure 2.7). The cluster ions passing through the axis of the quadrupole oscillate because of the electric field. Clusters can be selected according to their mass-to-charge ratio by the quadrupole electric field set to a value such that ions of a defined mass will be transmitted to the ion detector plate. The parameters which can be varied to allow clusters of a particular mass to pass through the filter are U, V and f.

The mass (M) is directly related to the amplitude of the ac voltage (V) and inversely proportional to the square of the frequency (f) applied to the poles

$$M = 7 \times 10^7 (\frac{kV}{f^2 d^2}) \qquad 2.7$$

where d is the diameter of the poles and k is a correction factor. The frequency applied to the poles determines the mass range that can be measured. While monitoring the ion

current from the quadrupole exit, scanning V allows a mass spectrum of the cluster beam to be acquired. The quadrupole does not require an ioniser before the entrance aperture since the nanocluster source produces a high proportion of ionised clusters. While operating the quadrupole mass filter, frequency and U V rate were set up to 5 kHz and 0.12, respectively.

Ion steering plates, fitted after the quadrupole mass filter (see figure 2.1), can be used to separate the ionised cluster beam from the neutral cluster beam. This is achieved by applying a bias voltage to the plates and causes separate deflected beams of positive and negative ions. The deflector plates are also used to measure the ion current by measuring the current following in the power supply circuit.

2.1.4 Deposition of Nanoparticles into Water

It is required to produce magnetic nanoparticles in a liquid suspension for biomedical applications. Therefore, the final stage of particle production is the deposition of the nanoparticles into water while the whole system is under the UHV which maintains clean conditions during the whole process as illustrated in figure 2.8.

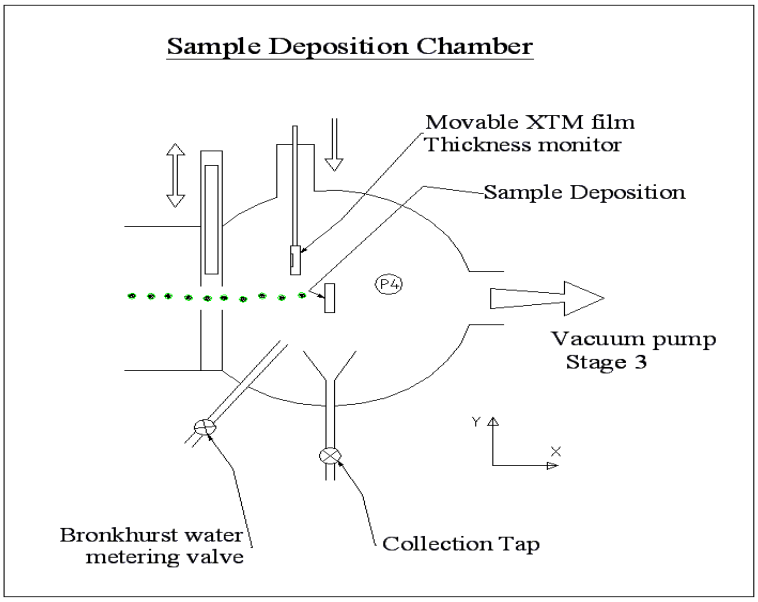

Figure 2.8: Side cross-section of the water deposition chamber which includes the LN_2 tank for sample deposition, movable XTM film thickness monitor and water meter valve.

The liquid nitrogen (LN_2) tank is placed in the deposition chamber after the valve, which allows control of the deposition chamber separately from the rest of the system. The technical problem with injecting water into a UHV system is the high vapour pressure of water at room temperature. Therefore, the tank is filled with LN_2 and cooled to 77 K prior to starting the deposition. The vapour pressure of crystalline ice is less than 10^{-14} mbar at 77 K though the condensation methods make it more suitable to use the value for amorphous ice, which is approximately 10^{-12} mbar [Kouchi 1987]. This is still too low to contaminate the particles during their formation [Binns 2012]. Also this system has the flexibility to use any liquid whose vapour pressure is adequately low at 77 K or above. The water vapour is introduced into the vacuum chamber as a molecular beam at a rate controlled by a Bronkhurst liquid flow controller and typically of the order of 1.2 ml/hour.

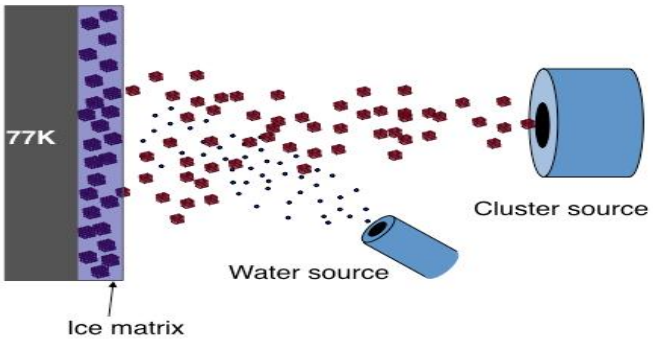

Figure 2.9: In the UHV clean condition, the nanoparticles are deposited into an ice matrix on the LN_2 tank [Binns 2012].

Before depositing the nanoparticles, the valve was closed and the water vapour was injected into chamber for about 60 minutes to have a layer of ice on the substrate. Even with the substrate at 77 K, when opening the water flow control valve, an increase in pressure (P_4) to ~ 10^{-7} mbar was observed because of the small proportion of water molecules reflected from the surface. The pressure gradient in the system prevents this level of water vapour contaminating the nanoparticles upstream. After that the valve was opened and the nanoparticles were deposited onto the same surface and embedded

within the ice matrix (see figure 2.9). The deposition process was continued until the required amount of sample had been produced. After that the deposition chamber was isolated and vented to clean nitrogen while the ice was allowed to melt. A petri dish was placed in a metal cup suspended under the tank and was used to collect the suspension.

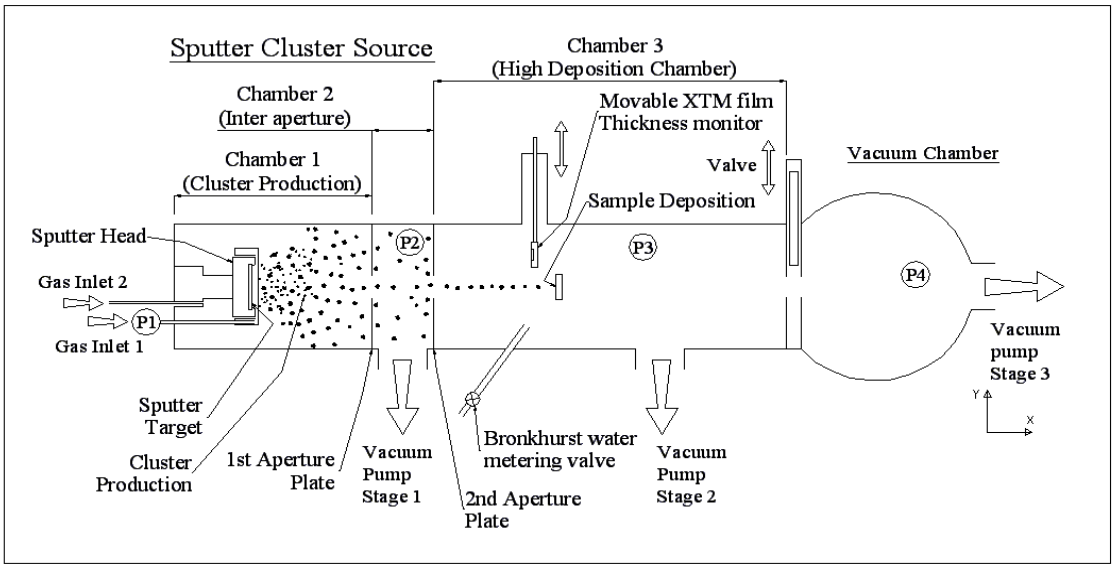

Figure 2.10: The LN_2 tank is placed after the second aperture to produce higher concentration sample.

It was found that the nanoparticle deposition rate in the final deposition chamber after the shell evaporator and quadrupole limited the density in the collected suspensions to less than 0.1 mg/ml, which is too low for an effective heating test. In order to produce suspensions with a higher density, an LN_2 tank was placed after the second aperture where the particle deposition rate is an order of magnitude higher than the deposition chamber though this limited the process to producing pure Fe nanoparticles only. During these depositions the valve between P_3 and P_4 regions was kept open to improve the vacuum at the deposition region. The water and nanoparticle depositions were carried out until the required amount of sample was deposited and then the system was vented with clean nitrogen. The ice was either allowed to melt into a petri dish under the LN_2 tank or it was collected outside the chamber.

The volume fraction of nanoparticle in the liquid suspension can be varied by changing the deposition rates of the particles and water vapour. The UHV chamber is equipped with a crystal thickness monitor (XTM) mounted on a linear transition stage for moving it in and out of the beam in order to measure the cluster flux (see figure 2.8 or 2.10). During the process, the nanoparticle deposition rate was measured every 10 minutes and was used to calculate the concentration of nanoparticles in the liquid suspension.

2.1.4.1 Calculation of the Concentration of Liquid Suspension

It is vital to determine the amount of the magnetic nanoparticles in a liquid suspension as this is required to calculate the SAR (see equation 2.15). Hence, during the deposition process, the deposition rate of the nanoparticles and water flow rate was recorded and used to calculate the concentration of the suspension.

The size of the nanoparticle deposition area was determined by depositing onto the substrate without water deposition and measuring the spot area as shown in figure 2.11.

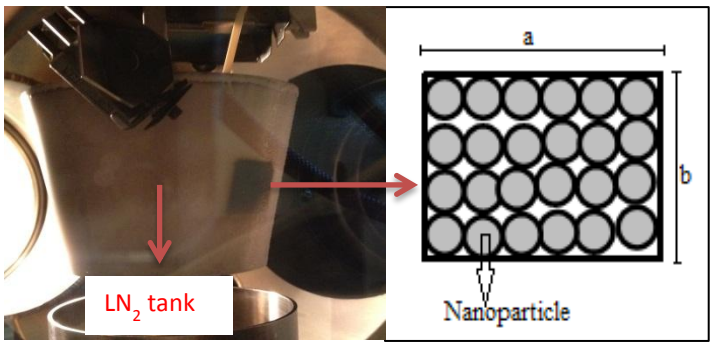

Figure 2.11: The spot that occurs after the deposition of the nanoparticles. a and b represent width and height of the spot respectively.

Using the area of the spot and the deposition rate during the process, the material volume can be calculated using

$$V(\mathrm{cm}^3) = a \times b \times d_{rate} \times 10^{-8} \times t_{dep.} \qquad 2.8$$

where $a(\mathrm{cm})\ and\ b(\mathrm{cm})$ represent the width and height of the spot respectively, d_{rate} is the average deposition rate (Å sec) during the process and $t_{dep.}$ is the deposition time (sec).

The total material mass (g), M_T, is calculated using the bulk density (ρ) of the target material

$$M_T = V \times \rho \quad (\mathrm{g}) \qquad 2.9$$

The concentration of the liquid suspension was determined using the total material mass and the amount of deposited water(d_{water}) and is given by

$$Concentration\ of\ the\ suspension = \frac{M_T\,(mg)}{d_{water}(ml)} \qquad 2.10$$

2.2. Magnetic Heating Tests

The magnetic heating experiment was used to determine the Specific Absorption Rate (SAR) of the nanoparticle suspensions by measuring the change in the temperature. The magnetic heating set up is illustrated in figure 2.12 and figure 2.13.

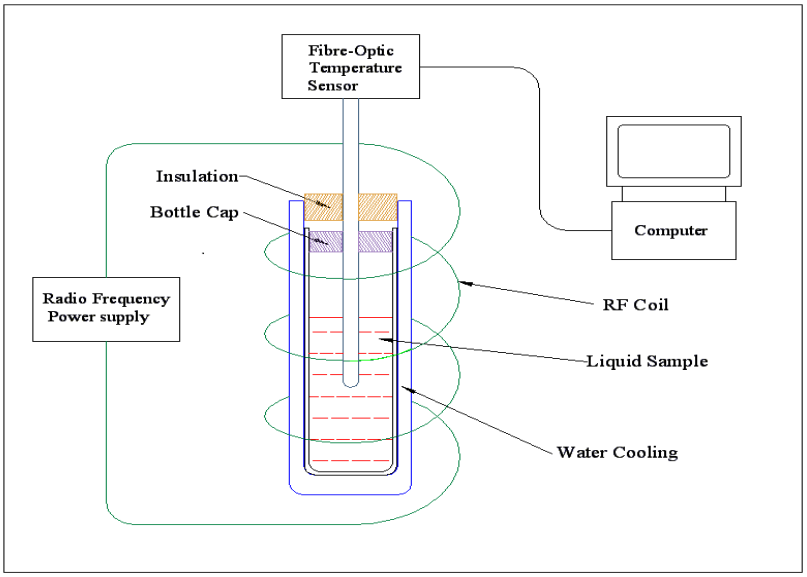

Figure 2.12: The magnetic heating experiment set up. For details, see text.

The sample was placed in a coil with a diameter of 67.4 mm containing 27 turns of copper wire, which was connected to a radio frequency (RF) power supply. The RF heater can generate an alternating magnetic field at a number of frequencies (60-225 kHz). When the heater is switched on, a significant amount of heating is produced by the copper wire because of resistive heating, which radiates onto the sample. Hence a plastic water pipe of diameter 50 mm was placed inside the heating coil to inhibit the heat transfer between the heated copper wire and the sample. In addition, a stable background temperature is essential to determine the real temperature increase of nanoparticles; therefore the system was connected to an external water chiller and a constant flow of water around the induction coil acted as a heat sink.

In this experiment, making a sensitive temperature measurement is vital since magnetic heating does not lead to a large increase. Hence a Photon Control fibre optic temperature sensor was placed into the sample through the bottle cap to avoid inductive heating of a thermometer. The sample was put in a glass cylinder which was surrounded by an insulating cylinder and was held in the middle of the induction coil. The insulating cylinder was made of polystyrene and was used to create a stable background temperature.

To begin with the background temperature was measured for 10 minutes with the RF heater switched off. Then the heater was turned on till the temperature was stable again at a higher value. This took about 30 minutes and at that point the heater was switched off, until the temperature returned to its starting value (see figure 2.14). The temperature was measured every second and the data logged on a computer.

The field × frequency ($H\times f$) product of the magnetic heating set up shown in figure 2.12 was limited to the Atkinson and Brezovich limit which will be discussed in section

2.2.1. On the other hand, nanoparticles might produce more heat at a higher field × frequency ($H \times f$) product which is still a safe dose limit for brain tumours as explained in the theoretical chapter (see figure 3.7). Hence a second magnetic heating set-up which had a higher field and frequency range was designed and is shown in figure 2.13.

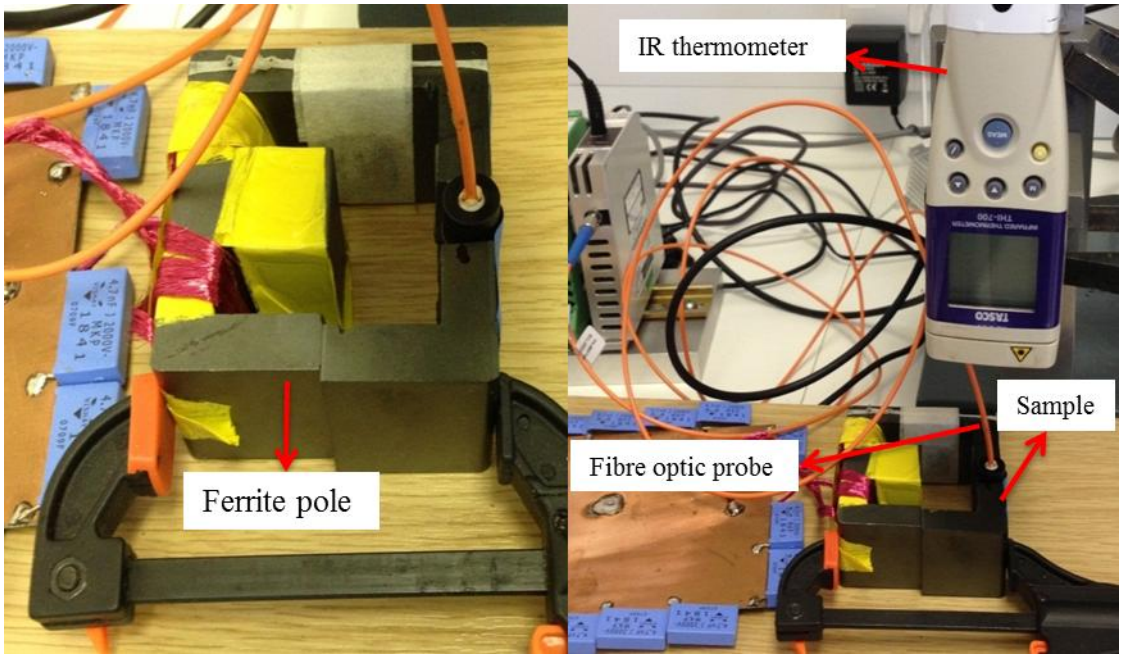

Figure 2.13: Pictures of the magnetic heating set-up to generate higher field and frequency.

As shown in figure 2.13, in the second set up ferrite pole pieces were used to boost the field amplitude within an 8 mm gap where the sample was placed. A fibre optic sensor was used to measure the sample temperature. This device did not have any cooling to stop the resistive heating of the plates so an (IR) infrared thermometer pyrometer was used to measure the coil temperature to determine the background temperature. However, it was essential to carefully adjust the IR thermometer distance from the surface which was determined by two laser beams from the thermometer crossing at the same point. The range of the alternating magnetic field amplitude was between 10 and 20 mT and could be altered by adjusting the gap between the pole pieces and the

voltage of the applied power. The frequency of the Applied Magnetic Field (AMF) could be varied from 60 to 250 kHz.

2.2.1 Safe Dose of AMF and Frequency

The SAR values of the magnetic nanoparticles depend strongly on the strength and the frequency of the oscillating magnetic field as well as the size and shape of the nanoparticles. However, the field amplitude and frequency product must be limited to avoid unwanted heating of healthy tissue that is caused mainly by eddy current loss [Kita 2010] and reduces the selectivity of the treatment.

In 1984 Atkinson and Brezovich [Atkinson 1984] investigated the effect that inductive magnetic frequencies would have on the patient and established an upper limit of the field × frequency ($H\times f$) product, which is about 4.85×10^8 A $m^{-1}s^{-1}$. Some studies have reported that the use of magnetic field amplitudes higher than 80 kAm^{-1} at 150 kHz seriously affected an animal body [Kita 2010]. Hence for all frequencies the field strength was set to the maximum safe limit for human exposure. For the first magnetic heating set up (see figure 2.12) this was set to the Atkinson-Brezovich limit of 4.85×10^8 A $m^{-1}s^{-1}$ while for the second one the product was set an order of magnitude higher, which has been shown to be safe for certain types of tumour [Pankhurst 2009, Binns 2014 b] (see chapter 3, section 3).

2.2.2 Calculation of SAR

The SAR describes the ratio of energy converted into heat per unit time and mass (W/g). It is also sometimes called the specific loss power (SLP) or specific heating power (SHP). Using the temperature curves from the magnetic heating, the SAR of the

magnetic nanoparticles can be calculated. The SAR can be calculated using two different methods, which depend on the coil used for heating test.

2.2.2.1. Calculation of SAR from the First Magnetic Heating Coil Test

In order to determine the SAR using the first magnetic heating coil, the pure water temperature curve was measured under the same experimental conditions and compared with the nanoparticle suspension. Figure 2.14 illustrates a model of the expected temperature curve produced for both pure water and a nanoparticle suspension in pure water by magnetic heating.

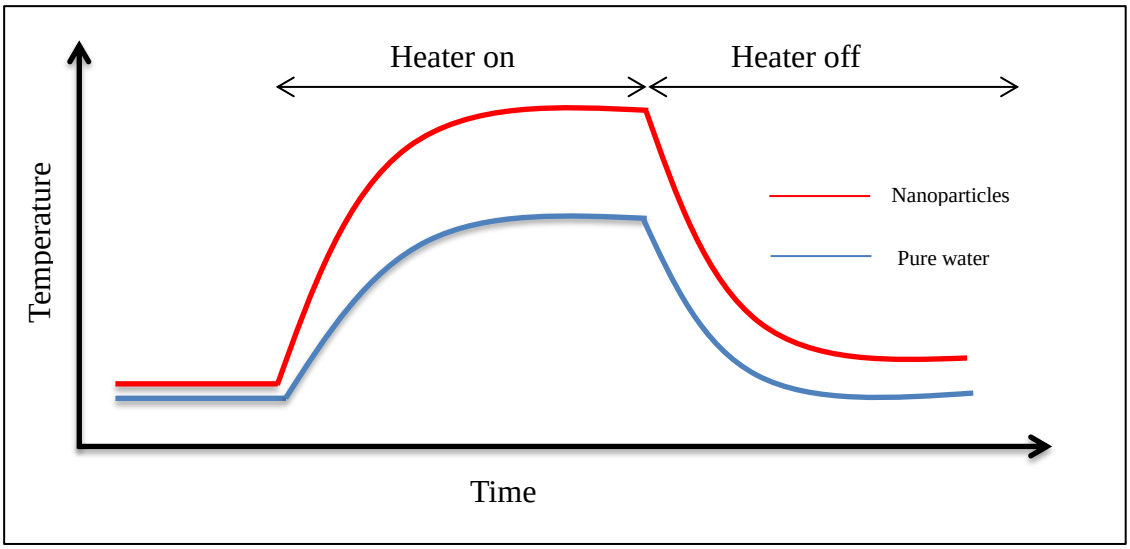

Figure 2.14: A model of expected temperature curves for pure water and a nanoparticle suspension.

It is possible to determine the heat transfer between coil and sample, the energy lost to the environment and most importantly, the magnetic heating by modelling the temperature curves.

The model for pure water is calculated by using equation 2.11, when the alternating magnetic field is on

$$T_{M_{pure\ water}} = \frac{[P_A - P_L\ T_R - T_S\ ]}{C_{H_2O}} + T_P \qquad 2.11$$

where $T_{M_{pure\ water}}$ is the model temperature (˚C), which is used in the model to fit the data, T_R is the real temperature (˚C) which is actually measured, T_S is the starting temperature (˚C), which is the average temperature before the heater is switched on, P_A is the ambient power (W), which is the transferred heat from the coil, P_L is the power loss factor (W) (heating lost to the environment), T_P is the previous calculated temperature value for for T_M (˚C) and C_{H_2O} is the specific heat of water (J/˚C). For instance, the first value for T_P is the initial temperature before the heater is switched on. The second value the T_P will be the first calculated value of T_M and so on.

When the magnetic field is switched off, the temperature for cooling is calculated by using equation 2.12.

$$T_{M_{pure\ water}} = T_P - \frac{P_L(T_R - T_S)}{C_{H_2O}} \qquad 2.12$$

The ambient power and power loss factor from equations 2.11 and 2.12 are obtained by optimising the fit between the calculated and measured curves. Then the magnetic heating power (P_B)(W) can be calculated by determining the model temperature for the nanoparticles and is given by

$$T_{M_{nanoparticles}} = \frac{[P_B + P_A - P_L\ T_R - T_S\ ]}{C_{H_2O}} + T_P \qquad 2.13$$

The cooling model of nanoparticles is calculated from equation 2.12.

The fits were optimised by applying a goodness of fit parameter, given by

$$fit\ parameter = \sum_{i=1}^{n}(T_M - T_R)^2 \qquad 2.14$$

The SAR is found by the equation

$$SAR = \frac{P_B}{m_{nanoparticle}} \text{ (W g)} \qquad 2.15$$

where $m_{nanoparticle}$ is the mass of the nanoparticles inside the liquid suspension.

2.2.2.2. Calculation of SAR from the Second Magnetic Heating Coil Test

As shown in figure 2.13, the second coil does not have any water cooling system so due to resistive heating there is a significant radiative heat transfer between the sample and the coil. Thereby the coil temperature is monitored by an IR thermometer during the heating test and extracted from the sample temperature as a background.

The magnetic heating power (P_B) can be calculated by determining the model temperature for the nanoparticles without any ambient power as shown in equation 2.16.

$$T_{M_{nanoparticles}} = \frac{[P_B - P_L\ T_R - T_S\ ]}{C_{H_2O}} + T_P \qquad 2.16$$

The cooling model of nanoparticles is calculated from equation 2.12.

Using equation 2.14 the model curve is fitted to the data curve and the SAR of the nanoparticles is determined from equation 2.15.

2.2.2.3 The Lowest Concentration Limit of Nanoparticles for Accurate Heating Tests

Concentration is an important parameter for an accurate heating test of nanoparticles. At low concentrations it is difficult to obtain the heat change due to the magnetic

nanoparticles since this is less than the ambient heating. Hence to determine the lowest concentration limit for which the SAR can be measured, 10 nm diameter commercially available ferrofluid (Magnacol) was diluted by factors of 10, 20, 30 and 40 with pure xylene and tested at the same frequency (112 kHz) and field (7.94 A/m) conditions as for the samples. Also, the theoretical SAR value for the ferrofluid was calculated assuming a saturation magnetisation (M_s) of 1.6×10^5 A/m and an anisotropy constant *(K)* of 2.3×10^4 J/m^3, which were obtained from Magnacol.

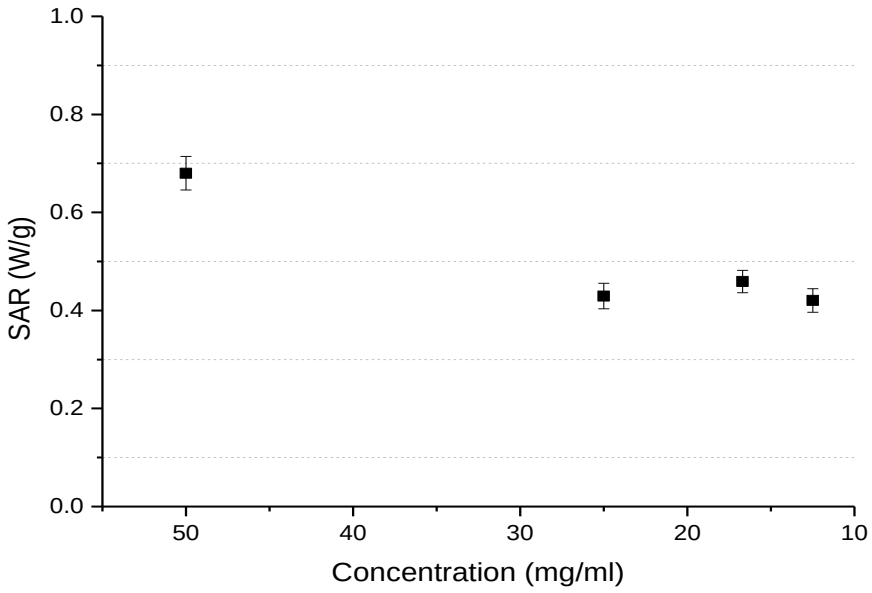

Figure 2.15: Measured SAR of the ferrofluid at different concentrations.

Figure 2.15 shows the SAR value of ferrofluid at four different concentrations. It shows that the concentration of ferrofluid (SAR ~ 0.5 W/g) should be at least 10 mg/ml. If we assume that the SAR of Fe nanoparticles is about 150 W/g (calculated), the lowest concentration should be at least 0.06 mg/ml.

Using the heating mechanisms of the nanoparticles (see chapter 3), the theoretical SAR of the nanoparticles was calculated to be 0.63 W/g which is in good agreement with the experimental results.

2.2.3. Comparing the Heating Performance of the Nanoparticles

Comparing the SARs of the nanoparticles used by different groups is a problem because of the use of different magnetic field frequencies and amplitudes, often much higher than the safe limit determined by Atkinson and Brezovich. In order to compare the fundamental performance of magnetic nanoparticles under the same conditions, Kallumadil et al [Kallumadil 2009] have suggested an equation to convert SAR to an Intrinsic Loss Parameter (ILP) as given below.

$$ILP = \frac{SAR}{H^2 f} \qquad 2.17$$

where H and f are the amplitude and frequency of the applied field respectively. This is independent of the parameters of the system and a helpful tool to make direct comparisons between different heating measurements of nanoparticles.

ILP is only appropriate for the susceptibility heating mechanism so it will not be appropriate for our samples in which hysteresis heating generates the majority of the total heat (see chapter 5). So a new way has been suggested to compare the performance of the materials by scaling to $H_0 \times f = 4.85 \times 10^8\ \mathrm{Am^{-1}s^{-1}}$ for all samples [Binns 2014 b].

2.3. Size Measurement of the Magnetic Nanoparticles in a Liquid Suspension

Accurately determining the size of magnetic nanoparticles is another vital aspect in order to compare theoretical and experimental values since the SAR depends on the size of the particles. Therefore the size distributions of the particles were measured by directly imaging the scattering light from each particle and analysing its Brownian motion using a Nanosight LM10 instrument.

2.3.1. NanoSight LM10

The Nanosight instrument produces a video of a number of nanoparticles moving under Brownian motion in a liquid suspension when illuminated by the laser light. The laser illumination device is mounted under a microscope objective as illustrated in figure 2.16. Particles pass through the laser beam path and are observed by the instrument as small points of light moving rapidly.

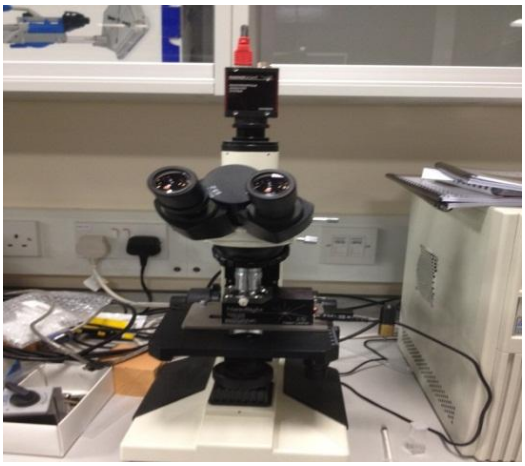

Figure 2.16: A picture of NanoSight.

Such motion can be tracked using a conventional CCD camera, which is used to capture video clips of the particle suspension while the laser is on. The Brownian motion recorded by the video is than analysed by software that determines the size distribution.

NanoSight is limited to sizing metal nanoparticles larger than about 10 nm. However, it enables a choice of which particles are analysed. This is a good characteristic to observe the isolated particle size in a liquid where agglomeration has occurred.

2.4. UV-visible Spectra Measurement

A Thermo Scientific Evolution 220 UV-visible Spectrophotometer (see figure 2.17) was employed for the UV-visible spectra measurement of the liquid suspensions.

Figure 2.17: A picture of UV-visible Spectrophotometer.

In UV-visible spectroscopy, a sample is probed with photons of wavelength in the range of ultraviolet-visible light and absorbance is measured relative to an appropriate control. This instrument is capable of measuring liquid samples with a volume less than 1 µl and collects spectra in the range 200-1100 nm. A Xenon flash lamp, which has a high intensity in the UV and visible regions of the spectrum, is used and does not need any warm-up time allowing instant measurements.

Chapter 3

Theoretical Approach

Recently there has been enormous interest in the magnetic properties of nanoparticles, which allow them to be exploited in biomedical applications such as Magnetic Nanoparticle Hyperthermia (MNH) [Binns 2012] and enhanced imaging for Magnetic Resonance Imaging (MRI) [Binns 2014 b, Chaughule 2012]. In this chapter, the basic concept of magnetism, superparamagnetic and blocked nanoparticles, the heating mechanism of magnetic nanoparticles, the medical limitation of applied fields, MRI and stabilisation of magnetic nanoparticles in liquid suspension will be briefly described.

3.1 Basic Concept of Magnetism

When a magnetic material is exposed to a magnetic field of strength H, the individual atomic moments in the material contribute to its overall response; the magnetic induction is given by

$$B = \mu_0 (H + M) \tag{3.1}$$

where μ_0 is permeability of free space, and the magnetisation $M = mN\ V$ is the magnetic moment per unit volume, where m is the magnetic moment of an atom and N/V is the number of atoms per unit volume.

All materials can be regarded as magnetic to a certain extent, because all materials respond to magnetic fields. However, they are conveniently categorised based on their volumetric magnetic susceptibility, χ, where:

$$M = \chi H \tag{3.2}$$

describes the relationship between the magnetic field H and magnetisation M induced in the material by the magnetic field.

Most material exhibits little magnetism in the presence of a magnetic field and are classified as paramagnets and diamagnets. The χ value for paramagnets is in the range of $10^{-6} - 10^{-1}$ and magnetic susceptibility for diamagnets is similar to the paramagnets but it is negative, which means that the magnetisation and the magnetic field are in opposite directions. However, some materials display ordered magnetic states and are magnetic without requiring a magnetic field; these are classified ferromagnets and ferrimagnets.

Ordered magnetic materials have much larger χ values than paramagnetic or diamagnetic materials due to the exchange coupling interactions between the electrons within the materials and χ tends to infinity in the case of spontaneous magnetisation.

It is worth mentioning that the susceptibility in ordered materials also depends on the Applied Magnetic Field (AMF) H which gives rise to the characteristic sigmoidal shape of the $M - H$ curve, with M approaching a saturation value at high fields. This gives rise to open $M - H$ curves called hysteresis loops. Figure 3.1 schematically illustrates a magnetisation vs field $(M - H)$ hysteresis loop.

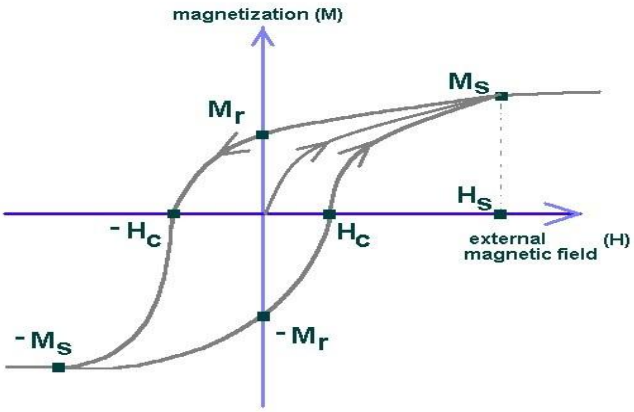

Figure 3.1: A typical magnetisation *vs* field *(M-H)* hysteresis loop.

The magnetisation of materials achieves its maximum value when the magnetic field is sufficiently large. The value is called the saturation magnetisation M_s and all the spins within a magnetic material align with the AMF. When the AMF is returned to zero, the material still has a residual magnetic moment which is called the remanent magnetisation M_r . To bring the material back to zero magnetisation, a magnetic field in the negative direction should be applied, and the magnitude of this is called the coercive field H_C .

In the case of samples containing magnetic particles, the particle size partly affects the shape of the hysteresis loop. Particles with sizes of the order of microns have a multidomain structure, similar to a bulk material. For smaller single domain particles, hysteresis is only observed if the particles are large enough to be magnetically blocked (see section 3.1.2). Below a critical size the particles are superparamagnetic (see section 3.1.1) and there is no hysteresis.

3.1.1 Superparamagnetic Nanoparticles

Superparamagnetism is a type of magnetism which is observed in single-domain fine magnetic nanoparticle systems showing close similarities to atomic paramagnetism. The size range of superparamagetic nanoparticles could be around a few nanometers to a couple of tens of nanometers, depending on the materials. In a single-domain particle, all the individual magnetic moments of atoms in a nanoparticle are locked together and form a single giant magnetic moment. Even though superparamagnetic nanoparticles share some similarities with paramagnetic samples such as a Curie temperature and a lack of hysteresis, the magnitude of χ is greatly enhanced.

In the superparamagnetic regime, the atomic spins in each nanoparticle are locked together by the exchange interaction to produce a single giant moment for the particle.

Application of a magnetic field induces the particle moments to orientate towards the field with some thermal disorder and this process continues until all spins are oriented with increasing magnetic field and saturation occurs. However, removing the magnetic field allows the particles to return to the randomly aligned state with no net moment. Superparamagnetic nanoparticles have a very high initial susceptibility because reorienting the large nanoparticle moments can be achieved with a relatively low field [Varadan 2008]. When the field is removed, all spins freely reorientate due to thermal energy so that in order to demagnetize the system, no external field is required. Therefore superparamagnetic nanoparticles have no coercivity. This leads to the anhysteretic, but still sigmoidal, $M - H$ curve as illustrated in figure 3.2.

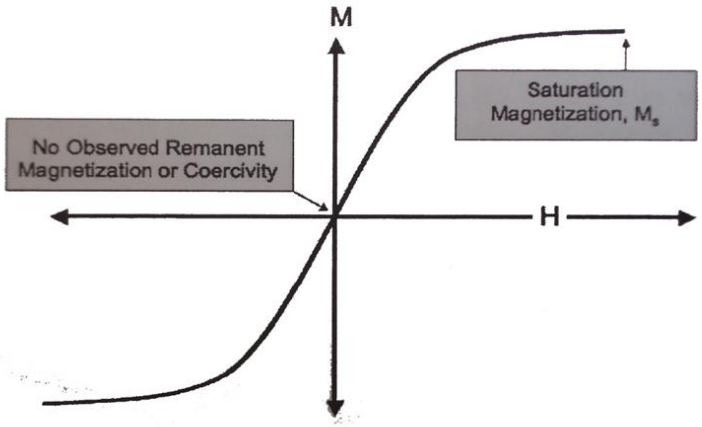

Figure 3.2: Hysteresis loop for superparamagnetic material.

In superparamagnetism, the magnetic moment of particles is free to fluctuate in response to thermal energy, however, below a certain temperature, there is not enough thermal energy to realign the magnetic moments so coercivity occurs. This temperature is called the "*blocking temperature*" which will be described in section 3.1.2. Below this temperature, nanoparticles show ferromagnetic behaviour.

3.1.2 Blocked Nanoparticles

The anisotropy K of the material is a key parameter to determine the pointing directions of the cluster magnetic moments in the absence of a magnetic field. The anisotropy of a system of particles can arise from magnetocrystalline anisotropy and also shape, stress and surface anisotropy. It is generally experimentally observed that individual nanoclusters have a uniaxial anisotropy [Binns 2002 a].

For uniaxial anisotropy there is an energy barrier that separates two antiparallel spin directions. The size of the energy barrier leads to two distinct types of behaviour of magnetic nanoparticles. If the energy barrier is very small compared to the atomic thermal energy, the magnetisation will be driven to either direction at very high frequency by the inherent thermal energy within the particle. In this state the particles are superparamagnetic as described in the previous section with an average magnetisation of zero until an external magnetic field is applied and the particle magnetisation will tend to be aligned with the field. If, on the other hand, the energy barrier is very large relative to the atomic thermal energy, the particle magnetisation is stuck or "*blocked*" in a given direction till it is reversed by an external field. The blocking temperature of nanoparticles can be estimated in terms of the barrier height and thermal energy, using the Arrhenius Law:

$$\tau = \tau_0 \, e^{\left(\frac{\Delta E}{k_B T}\right)} \qquad 3.3$$

where τ_0 is a natural fluctuation lifetime which has been measured to be ~10^{-9} s [Jackson 2000]. $\Delta E = KV$ is the energy barrier where K is the anisotropy constant of the material and V is the volume of the single nanoparticle. $k_B T$ is the thermal energy where k_B is Boltzmann's constant and T(K) is the temperature.

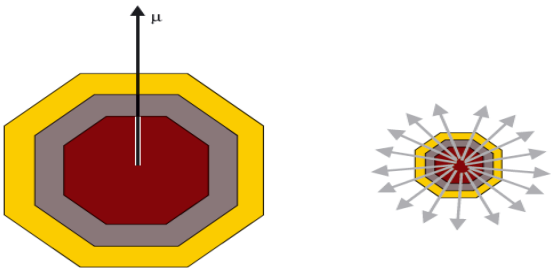

Figure 3.3: (a) Blocked magnetic nanoparticles. (b) Superparamagnetic nanoparticles [Binns 2010].

The heating mechanisms of magnetic nanoparticles depend on whether the particles are blocked or superparamagnetic at room temperature (T~300 K) at which most experiments are performed. Therefore it is important to determine the blocked size for single nanoparticles from equation 3.3 [Binns 2014 a].

$$d = \left(\frac{6k_B T \log \tau \tau_0}{\pi K}\right)^{1\ 3} \qquad 3.4$$

where d is the diameter of a single nanoparticle.

It should be noted that the observation of superparamagnetism is dependent not only on temperature, but also on the measurement time τ_m [Pankhurst 2003]. When the measurement time (τ_m) is much bigger than the relaxation time ($\tau \ll \tau_m$), particles appear superparamagnetic, while when $\gg \tau_m$, the *"blocked"* state of the system is observed.

3.2 Heating Mechanism of Magnetic Nanoparticles

The heating mechanism of magnetic nanoparticles in a liquid suspension in response to an AMF depends strongly on the size distribution of nanoparticles and normally more than one mechanism is active. The most widely used model assumes that nanoparticles are superparamagnetic [Rosensweig 2002] but in practical terms suspensions contain a

size range that crosses the boundary between superparamagnetic and blocked particles. Various theories have been developed to cover larger particles as well [Hergt 2008, Hergt 2010].

Recently, Vallejo-Fernandez et al published a new model which includes the heating mechanism of the whole size range of particles [Vallejo-Fernandez 2013]. With this model, it is possible to calculate the heating ability of nanoparticles from the superparamagnetic to the blocked state. Theoretical details will be given below but the basic physics underlying the heating mechanisms is illustrated in figure 3.4. Figure 3.4 (a) shows that superparamagnetic nanoparticles which are the smallest nanoparticles, have no permanent magnetic moment in zero field since their magnetic moment fluctuates on the timescale of nanoseconds [Binns 2014 b]. When a magnetic field is applied, all the magnetic moments develop a magnetisation along the applied field and it follows the field when it oscillates. Due to the finite lifetime of nanoparticle magnetic moments, a phase lag between the magnetisation and the applied field occurs. This phase lag is determined by an imaginary (loss) component of the susceptibility (χ'') and its magnitude determines the amount of power produced by the nanoparticles. This mechanism is called susceptibility heating [Vallejo-Fernandez 2013].

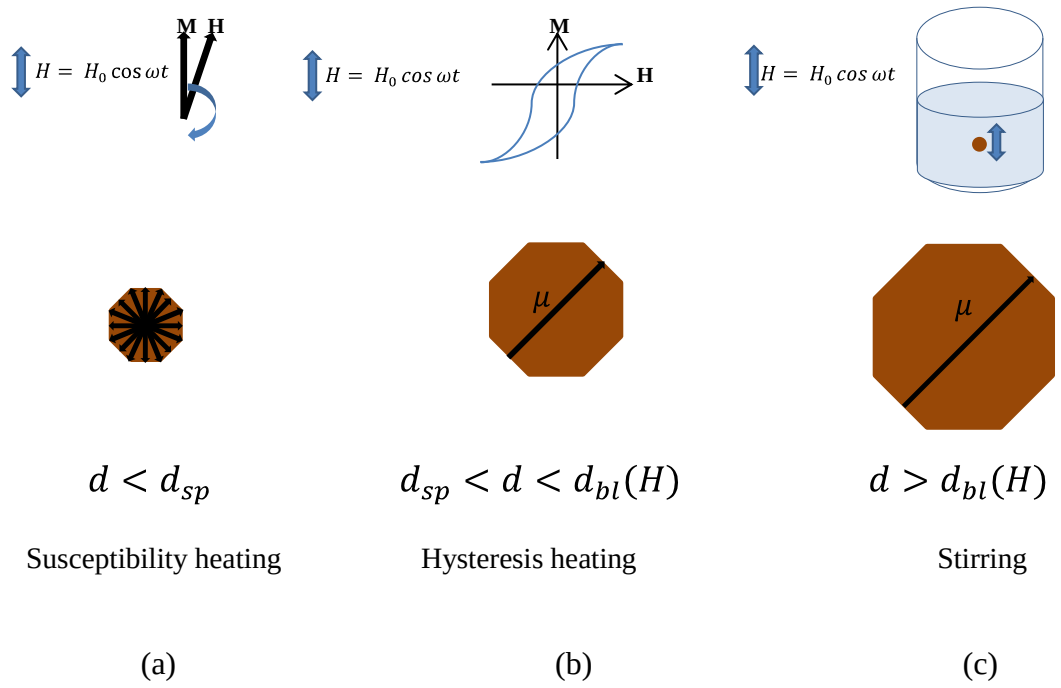

Figure 3.4: Heating mechanism of nanoparticles in response to an AMF (a) For $d < d_{sp}$ particles are superparamagnetic and there is a phase lag between the applied field and particle magnetisation. (b) Assembly of blocked particles ($d > d_{sp}$) in which the magnetisation follows a hysteresis loop. (c) Above a critical field-dependent size ($d_{bl}(H)$), the applied field is insufficient the switch to particle magnetic moment but heat is generated due to the field gradient by stirring [Vallejo-Fernandez 2013].

Above a critical diameter which is labelled d_{sp} in figure 3.4, the particles will be blocked and susceptibility heating will not happen. Each particle ($d > d_{sp}$) will switch its magnetisation in response to the AMF and heating due to the hysteresis loss will occur. The heating generated is proportional to the area enclosed by the loop. However, above a second critical diameter, labelled $d_{bl}(H)$, hysteresis heating is absent. The reason for this is that the magnitude (H_0) of the AMF will not be large enough to switch the particle magnetic moments due to the increasing coercivity of the nanoparticles with size. It is important to underline that $d_{bl}(H)$ depends on the amplitude of the applied

field. The nanoparticles ($d > d_{bl}(H)$) still produce heating by stirring in response to an AMF, however its calculation is extremely complex [Vallejo-Fernandez 2013].

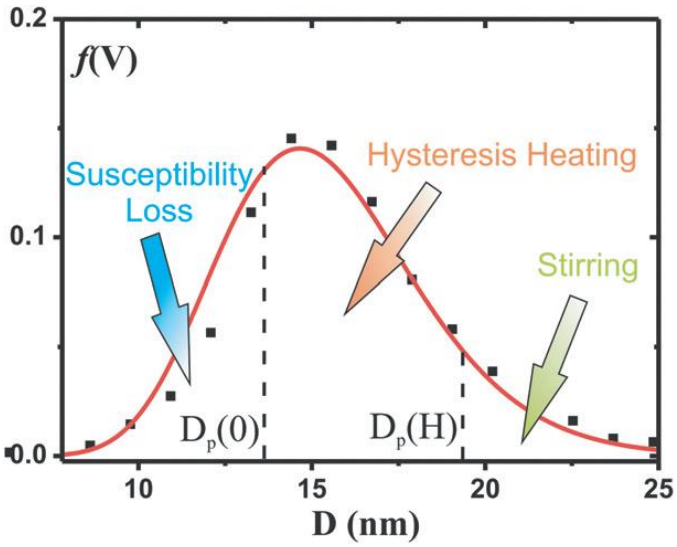

Figure 3.5: Range of sizes that generate heat by different mechanisms according to the size distribution of nanoparticles [Vallejo-Fernandez 2013].

Figure 3.5 illustrates that the heat generated by the log-normal size distribution of a typical nanoparticle sample used for hyperthermia is due to all three mechanisms, the detailed theory for which is presented below.

First of all, the susceptibility heating is produced by superparamagnetic nanoparticles with diameters up to the blocking size given by equation 3.4 but labelled here by d_{sp} as shown in equation 3.5.

$$d_{sp} = \left(\frac{6k_B T \ln(tf_0)}{\pi K}\right)^{\frac{1}{3}} \qquad 3.5$$

where t is the time of measurement (usually taken as the inverse of the AMF frequency) and f_0 is the magnetic moment fluctuation limit at high temperature ($f_0 \sim 10^9$ s^{-1}). The power produced per unit volume with susceptibility heating by an applied AMF of the form $H = H_0 \cos \omega t$ is given by [Rosensweig 2002]:

$$P_{sus} = f\mu_0\pi\chi^{"}{H_0}^2 \quad 3.6$$

where f is the frequency of the AMF (Hz) and H_0 is the amplitude of the AMF (Am^{-1}). It is clear that for susceptibility heating at a given field amplitude, the power is proportional to the imaginary part of susceptibility, χ" which is given by the following equation

$$\chi^{"} = \frac{\omega\tau}{1+(\omega\tau)^2}\chi_0 \quad 3.7$$

where τ is the lifetime of the particle magnetic moment, ω is the angular frequency and χ_0 is the equilibrium susceptibility of the assembly. The magnetisation of a sample containing nanoparticles is described by the Langevin function [Rosensweig 2002]:

$$L_{(\xi)} = M \; M_s = coth\,\xi - \frac{1}{\xi} \quad 3.8$$

where ξ is the factor $\mu_0 M_s HV \; kT$ with M_s being the saturation magnetisation of nanoparticles. Thus the magnetic field dependent equilibrium susceptibility can be written in terms of the initial susceptibility of the assembly, χ_i as:

$$\chi_0 = \frac{3\chi_i}{\xi} \; \coth\xi - \frac{1}{\xi} \quad 3.9$$

and finally χ_i can be written as:

$$\chi_i = \frac{\mu_0\phi{M_s}^2V}{3k_BT} \quad 3.10$$

where ϕ is the volume fraction of the nanoparticles and set to 1 to determine the heating performance of the material. Power generated by the assembly of nanoparticles is calculated per m^3 using equation 3.6. However, in order to calculate the power generated per kg or Specific Absorption Rate (SAR), the result of equation 3.6 is

divided by density of the material. SAR is the most useful value to understand the effectiveness of nanoparticles in hyperthermia treatment and is quoted in units W/g.

The only unknown factor in equation 3.7 to make an accurate determination of heating is the lifetime of the magnetic moment, τ which is due to superparamagnetic Neel and Brownian relaxation processes (see figure 3.6).

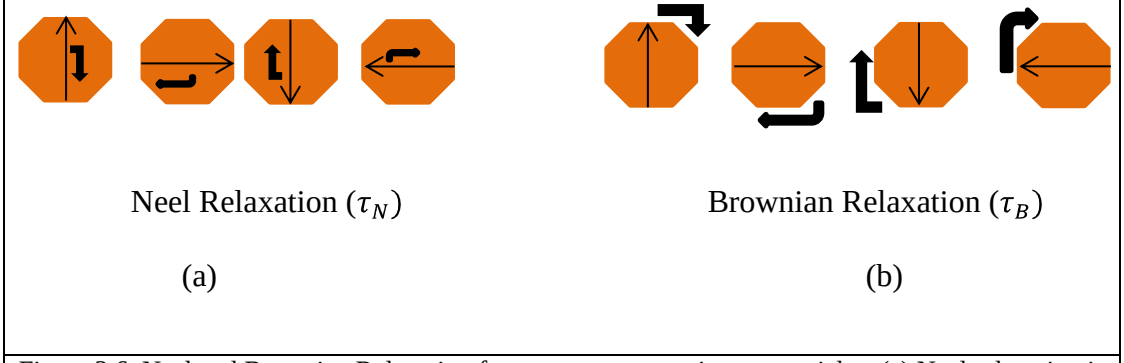

Figure 3.6: Neel and Brownian Relaxation for superparamagnetic nanoparticles. (a) Neel relaxation is the rotation of the magnetic moment within the particle. (b) Brownian relaxation is the rotation of the particles within the viscous fluid.

The nanoparticle magnetic moment time constant is a combination of Neel relaxation which is the rotation of the magnetic moment within the particles as shown in figure 3.6 (a) and Brownian relaxation which is the rotation of the particle in the viscous fluid, as illustrated in figure 3.6 (b). The time constant associated with the Neel relaxation is expressed by [Vallejo-Fernandez 2013]:

$$\tau_N = \frac{1}{f_0} exp \frac{KV(1-H_0\ H_K)^2}{k_B T} \qquad 3.11$$

where K is the anisotropy constant of the nanoparticles and H_K is the anisotropy field given by $H_K = 2K\ \mu_0 M_s$. The time constant associated with the Brownian relaxation is given by [Rosensweig 2002]:

$$\tau_B = \frac{3V_H\eta}{k_BT} \tag{3.12}$$

where V_H is the hydrodynamic volume of the nanoparticles, which includes the particle diameter plus the coating added to stabilise the suspension and any targeting [Binns 2014 b] and η is the viscosity of the carrier fluid. The time constant combined from both relaxations is given by the following expression:

$$\frac{1}{\tau} = \frac{1}{\tau_N} + \frac{1}{\tau_B} \tag{3.13}$$

Nanoparticle volume is a key factor to determine susceptibility heating since τ_N, τ_B, χ_0, χ_i (and probably K) all hinge on the diameter of the nanoparticles. Hence, for a size distribution, integration for diameters up to d_{sp} weighted by the probability of each size is essential. A log-normal size distribution is normally used to represent the size distribution of nanoparticles:

$$g\ d\ = \frac{1}{\overline{2\pi}\sigma d} exp\ \frac{-(\ln(d\ d_0))^2}{2\sigma^2} \tag{3.14}$$

where $ln(d_0)$ is the median and σ is the standard deviation. The normalised function $g(d)$ is given by:

$$\int_0^{\infty} g(d)\mathrm{d}\ d\ = 1 \tag{3.15}$$

Using equation 3.6 with the size distribution of the nanoparticles, the power generated per unit volume by susceptibility heating is given by:

$$P_{sus} = f\mu_0\pi {H_0}^2 \int_0^{d_{sp}} \chi^{"}\ d\ g(d)\mathrm{d}(d) \tag{3.16}$$

Susceptibility heating is valid for diameters below d_{sp} and from above this critical diameter to a second critical diameter $d_{bl}(H)$, the power will be generated by hysteresis

heating, which is proportional to the AMF frequency multiplied by the area of the hysteresis loop. The applied field magnitude is not strong enough to switch the particle magnetisation for diameters above $d_{bl}(H)$. The nanoparticle coercivity, H_c, depends on particle size according to the equation [Vallejo-Fernandez 2013]:

$$H_c = H_K \left[1 - \left(\frac{6k_B T \ln tf_0}{\pi K d^3}\right)^{1/2}\right] \quad \text{where} \quad H_K = 0.96\, K/M_s \tag{3.17}$$

The critical diameter above which the field amplitude is too weak to switch the particle magnetisation is given by:

$$d_{bl}(H) = \left[1 - \frac{\mu_0 H M_s}{0.96K}\right]^{-2/3} \times d_{sp} \tag{3.18}$$

The power generated by hysteresis heating between the size ranges of d_{sp} to d_{bl} is expressed by:

$$P_{hyst} = 2f\mu_0 M_s \int_{d_{sp}}^{d_{bl}(H)} H_c \, d \, g(d)\mathrm{d}(d) \tag{3.19}$$

Above the diameter, $d_{bl}(H)$, hysteresis heating vanishes but heat can still be produced by the frictional losses due to mechanical stirring. Even though writing an equation for stirring heating is impossible, Vallejo-Fernandez et al demonstrated the significant effect of stirring heating by comparing the SAR of similar nanoparticles dispersed in different viscosity fluids.

3.3 Limitations of the AMF

The SAR increases with the frequency and amplitude of the applied field but there is a biological limitation to the strength of the AMF that can be used as sufficiently high fields lead to eddy current heating and nerve stimulation in tissue. In the ideal approach of MNH, however, heat should only be generated by the AMF at the location where the

nanoparticles are. According to Faraday's law, any oscillating magnetic field will produce electric field gradients expressed by:

$$\nabla \times \boldsymbol{E} = -\frac{\partial \boldsymbol{B}}{\partial t} \qquad 3.20$$

These field gradients cause eddy current heating in tissue and stimulation of nerve and muscle [Binns 2014 b]. Thanks to the well-characterised physiological properties of tissue, determination of the safe limits of the AMF is possible. Therefore, the calculation of eddy currents will be a good starting point. Eddy currents produced by the field gradients in resistive tissue produce direct Joule heating. Generally, the calculation of eddy currents is complex but it is possible to derive an analytical expression, in the case of a uniform cylinder of tissue, for the power deposited per unit volume ($\mathrm{Wm^{-3}}$) by an AMF [Pankhurst 2009]:

$$P = \pi^2 \frac{\mu^2 {\mu_0}^2 \sigma}{2} f^2 r^2 {H_0}^2 \qquad 3.21$$

Here μ is the relative permeability of the tissue (≈ 1), σ is the conductivity ($\mathrm{Sm^{-1}}$) and r is the radius of the specimen (m). The upper safe dose limit for heating tissue is suggested to be about 0.025 $\mathrm{Wcm^{-3}}$ [Pankhurst 2009] and conductivity for fat and blood is measured to be 0.025 ($\mathrm{Sm^{-1}}$) and 0.64 ($\mathrm{Sm^{-1}}$), respectively [Jordan 1993]. The range of the AMF amplitude and frequency that produce heating of more than 0.025 $\mathrm{Wcm^{-3}}$ for these two types of tissue for a thin torso sized (≈ 15 cm) specimen is illustrated in figure 3.7 [Binns 2014 b]. With reference to equation 3.21, the product ($H_0 \times f$) is essential to determine the upper limits of field and frequency to avoid damage to the healthy tissue. It is generally accepted that the maximum safe dose for the product of $H_0 \times f$ is 4.85×10^8 $\mathrm{Am^{-1}s^{-1}}$ [Atkinson 1984]. This is known as the Atkinson-Brezovich limit.

Moreover, it is clear from figure 3.7 that with increasing frequency, threshold stimulation of peripheral nerves shows a decreasing trend. After a specific point, stimulation is not dependent on frequency. In general, the applied field frequency during MNH treatment is 100 kHz, therefore, within the safe zone for the AMF, peripheral nerve stimulation will not be a problem.

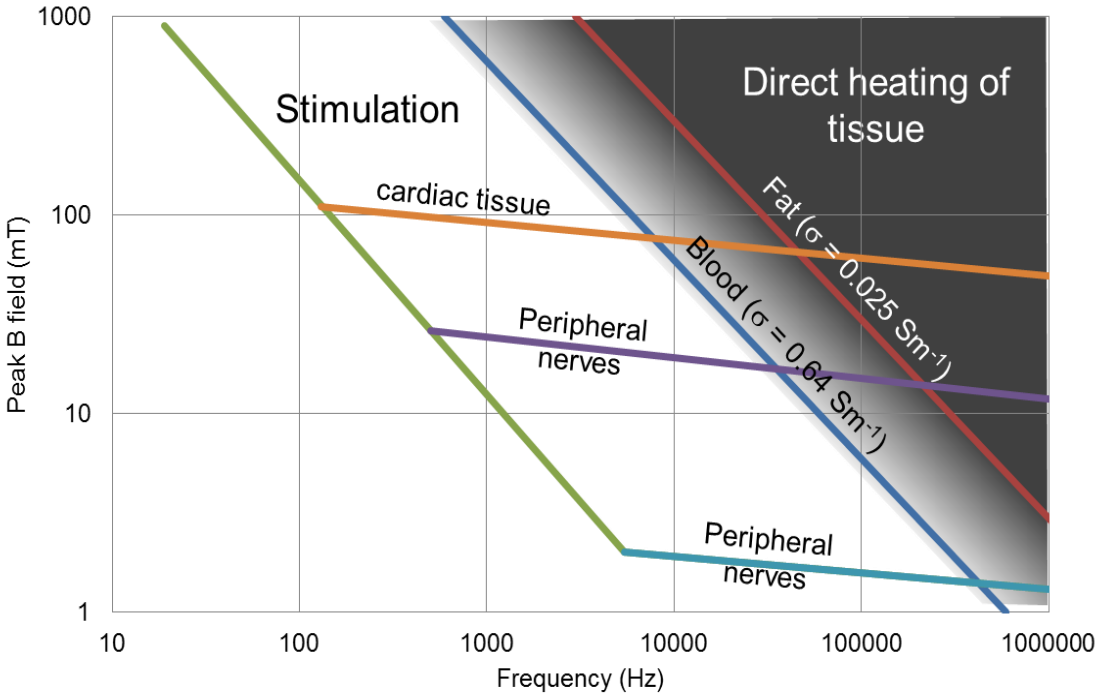

Figure 3.7: Areas of the magnitude and frequency of an AMF exposed to tissue that generate direct eddy current heating for fat and blood and also stimulate peripheral nerves and cardiac tissue [Binns 2014 b].

Also figure 3.7 shows that for sufficiently large strengths of the AMF, it is possible to have direct stimulation of muscles, which can result in extremely dangerous situations around the heart. Comparing this with the peripheral nerve stimulation, it is higher at all frequencies so the patients themselves can provide a warning prior to muscle stimulation. In general, at 100 kHz, the magnitude of the applied field should be lower than 20 mT (16 kAm^{-1}). Additionally, for smaller parts of the body or small animals, higher amplitudes of AMF can be applied without direct heating of tissue.

There is another important factor in addition to the specimen size and that is where the tissue is within the body. This has been demonstrated by clinical studies [Maier-Hauff 2007, Johannsen 2010] that show that much higher amplitudes could be used for homogenous brain tissue rather than the prostate region, which has a complex morphology of tissue and bone. From the above discussion, the maximum safe dose limit of the amplitude of the applied field at a given frequency is an essential point since the nanoparticles need to produce sufficient heat within these limits of the AMF.

3.4 Using the Magnetic Nanoparticles as MRI Contrast Agents

MRI is an important diagnostic tool in medical science owing to its high soft tissue contrast, good spatial resolution and penetration depth. Another important feature for MRI is its ability to obtain images safely. The biological tissue in the human body has a high concentration of hydrogen nuclei (protons) in the form of water and fat [Chaughule 2012]. Hence the working principle of MRI is based on detecting signals from relaxation of hydrogen nuclei from tissue and organs and converting these signals into an image. When an external strong magnetic field is applied to the human body, the free hydrogen nuclei align parallel and antiparallel (lower and higher energy state, respectively) to the magnetic field and oscillate at a specified frequency, known as Larmor frequency. When a radiofrequency (RF) pulse with a frequency equal to the Larmor frequency (perpendicular to the applied field) is applied to the nuclei, the protons absorb energy and have a net magnetisation which is perpendicular to the applied field. When the RF pulse is removed, the excited nuclei relax to initial state. There are two types of relaxation processes obtained in MRI that are highly sensitive to the chemical environment and type of tissue: longitudinal (spin-lattice) and transverse (spin-spin) relaxation processes. The time constants of these relaxation processes are

known as T_1 and T_2, respectively. In order to improve image quality and accentuate differences between normal and malignant tissue, contrast agents can be used [Lok 2001]. Contrast agents are classified as T_1 and T_2 contrast agents according to which relaxation process they modify. The currently available contrast agents used are Gd chelates and superparamagnetic Fe oxide nanoparticles.

The relaxivity is a key factor to determine the performance of a magnetic contrast agent. The relaxivity is described as the increase in the relaxation rate that occurs by adding 1mmol/l of the active ion and is given by;

$$R_{i(obs)} = \frac{1}{T_{i(obs)}} = \frac{1}{T_{i(diamag)}} + r_i C \qquad 3.22$$

where $i = 1$ or 2 (relaxation of longitudinal or transverse magnetisation respectively), $R_{i(obs)}$ is the observed relaxation rate of the system with the contrast agents added, $T_{i(diamag)}$ is the relaxation time of the system before adding the agent, r_i is the relaxivity of the agent with units of $\mathrm{s}^{-1}\mathrm{mmol}^{-1}\mathrm{l}$ and C is the concentration of its active ions in mmol/l.

The relaxations mechanisms are classified according to inner sphere and outer sphere effects. Magnetic nanoparticles have a large magnetic susceptibility so in the normal range of magnetic field strengths used in MRI they are saturated. Therefore, all spins of the nanoparticles are aligned with the fields and the movement of the water protons adjacent to particles leads to a dipolar interaction. This effect is called outer sphere relaxation [Rümenapp 2012]. The inner sphere relaxation is due to the exchange interaction between the protons and electrons is a minor contribution for superparamagnetic nanoparticles [Binns 2014 b].

R_1 and R_2 relaxation rates per nanoparticle can be calculated using the following equations

$$R_1 = \frac{1}{T_1} = \frac{6400\pi}{81} \left(\frac{\mu_0}{4\pi}\right)^2 {\gamma_1}^2 \mu^2 \frac{1}{rD} 9J_1(\omega_1, \tau, \tau_{S1} \dashrightarrow \infty) \quad 3.23$$

$$R_2 = \frac{1}{T_2} = \frac{6400\pi}{81} \left(\frac{\mu_0}{4\pi}\right)^2 {\gamma_1}^2 \mu^2 \frac{1}{rD} [4.5J_1(\omega_1, \tau, \tau_{S1} \dashrightarrow \infty) + 3J_1(0)] \quad 3.24$$

where γ_1 is the gyromagnetic ratio of the proton, D is the diffusion coefficient of the proton, r is the radius of the nanoparticles and τ_S is the lifetime of the magnetic moment of the nanoparticle within the applied field. The calculated relaxivities from equation 3.23 and 3.24 should be multiplied by $6 \times 10^{20}/N$ to get the quoted value per mmol/l with N the number of atoms in each nanoparticle [Binns 2014 b].

R_1 and R_2 are also proportional to the square of the saturation magnetisation [Binns 2014 b] so within the assumption of saturated nanoparticles, which have infinite relaxation times, the size/material dependence of the relaxivities is given by:

$$R_i \propto {M_s}^2 d^2 \quad 3.25$$

Thus the maximum relaxivity of the particles is obtained with a material with a high saturation magnetisation and the particles should be as large as possible within the single domain size range.

3.5 Stabilisation of Magnetic Nanoparticles in Liquid Suspension

The most important feature of the magnetic nanoparticles for clinical applications is that they are dispersed in a liquid suspension. Especially for hyperthermia and MRI, magnetic nanoparticles are required to be stable against particle agglomeration in the presence of various attractive and repulsive interactions. Due to quantum vacuum

fluctuations, the attractive Van der Waals force is present in the system. Additionally, if the magnetic nanoparticles in the suspension are magnetically blocked, the magnetic dipolar force will be present as an additional attractive interaction. Brownian motion will bring the nanoparticles sufficiently close for Van der Waals and magnetic (if present) attractions to cause agglomeration and an irreversible size increase. The presence of ions in the solution causes an electric double layer and also coating particles by polymers leads to steric repulsion. Both electric double layer and steric repulsion produce repulsive forces between the particles.

In the 1940s, Derjaguin, Verwey, Landua and Overbeek [Derjaguin 1941 and Verwey 1948] developed the formal theory which explains charged surfaces interacting through a liquid medium. This theory is known as the DVLO theory and it combines the effects of Van der Waals (VdW) attraction and electric double layer (EDL) repulsion. The attractive part for spherical particles is determined by adding the Van der Waals attraction between all the individual atoms in the form, $-C\ r^6$, where C is a constant dependent on the type of atom and is formulated as:

$$U_A\ D\ = -\frac{AR}{12D} \tag{3.26}$$

where $A = \pi^2 C\rho^2$ is the Hamaker constant with ρ the atomic density at the particle surface (atoms/unit area), R is the radius of the particles and D is the distance between particles' surfaces.

The repulsive force between two spherical particles can be written in terms of the zeta potential, ξ as [Eastman 2010]

$$U_R\ D\ = 2\pi\varepsilon\varepsilon_0 R\xi^2 e^{-KD} \tag{3.27}$$

in which

$$K = \sqrt{\frac{\rho e^2 z^2}{\varepsilon \varepsilon_0 k_B T}} \qquad 3.28$$

where K is the inverse of the Debye screening length and ε is the relative permittivity for a fluid containing ions with a valency, z, and a density ρ. Hence the total interaction potential between the particles can be calculated with the following equation:

$$U_A\ r\ = -\frac{AR}{12D} + 2\pi\varepsilon\varepsilon_0 R\xi^2 e^{-KD} \qquad 3.29$$

The interaction energy between two Fe oxide nanoparticles with a radius of 5 nm is demonstrated in figure 3.8. The Hamaker constant for Fe oxide nanoparticles (magnetite, maghemite and hematite) interacting through water has been calculated to be in the range $3.3 - 3.9 \times 10^{-21}$ J [Faure 2011]. Thereby the Van der Waals part can be calculated absolutely. For the repulsive part, the density of monovalent ions and the zeta potential were taken as 3×10^{22} m^{-3} and 8.8 mV, respectively [Binns 2014 b].

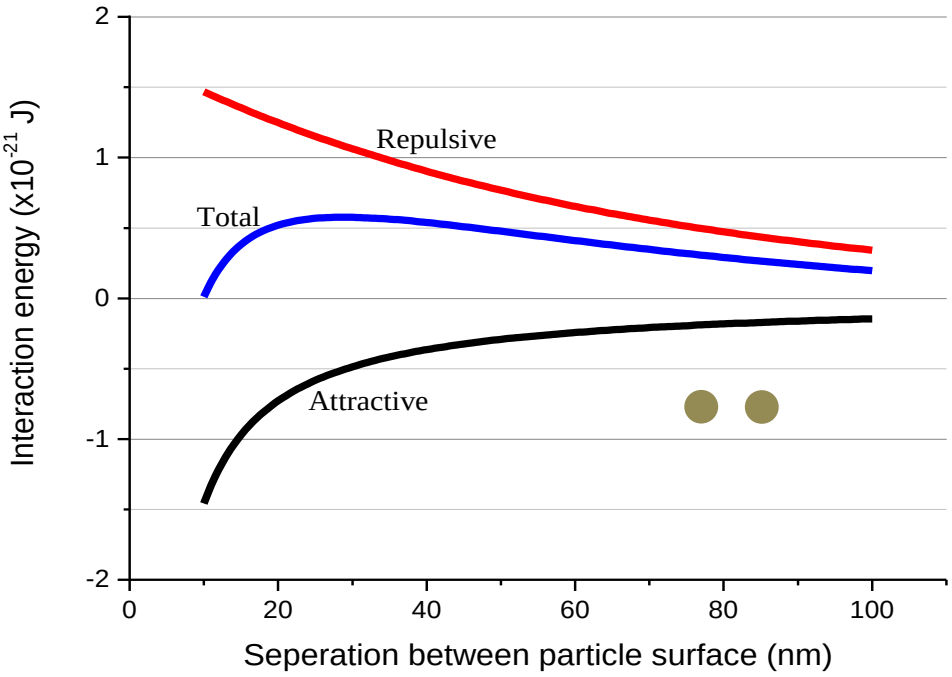

Figure 3.8: Attractive, repulsive and total interaction energies between two Fe oxide nanoparticles of radius 5 nm through water for a stable suspension at 300 K. The Hamaker constant, $A = 3.5 \times 10^{-20}$ J, the zeta potential = 8.8 mV, the monovalent ion concentration is 3×10^{22} m^{-3} and $\varepsilon = 80$.

It is demonstrated that the distance between two iron oxide nanoparticles should be at least 10 nm to stabilise the nanoparticles against agglomeration. Additionally, if the zeta potential decreases from 8.8 to 5 mV, the distance increases to 70 nm and under 5 mV the attractive force would be higher than the repulsive and particle agglomeration occurs.

Fe oxide nanoparticles with a radius of the 5 nm will be superparamagnetic. Therefore the magnetic dipolar interaction between them should be zero. The interaction energy between two superparamagnetic Fe nanoparticles will be similar to iron oxide nanoparticles due to the lack of a magnetic dipolar interaction.

At room temperature, blocked nanoparticles will exhibit a static magnetic moment which leads to an additional attractive interaction given by:

$$\frac{\mu_0 \mu^2}{4\pi r^3} \qquad 3.30$$

where μ is the magnetic moment of the nanoparticles and r is the distance between their centres. Comparison of the attractive, repulsive and total interaction energies for two 8 nm radius iron oxide nanoparticles with and without the magnetic dipolar force included is shown in figure 3.9. The effect of including the magnetic dipolar force is that the attractive force becomes dominant. Hence the distance between two iron oxide nanoparticles should be at least 50 nm in the presence of the magnetic dipolar force. Comparing the 50 to 10 nm, the influence of the magnetic force is very strong.

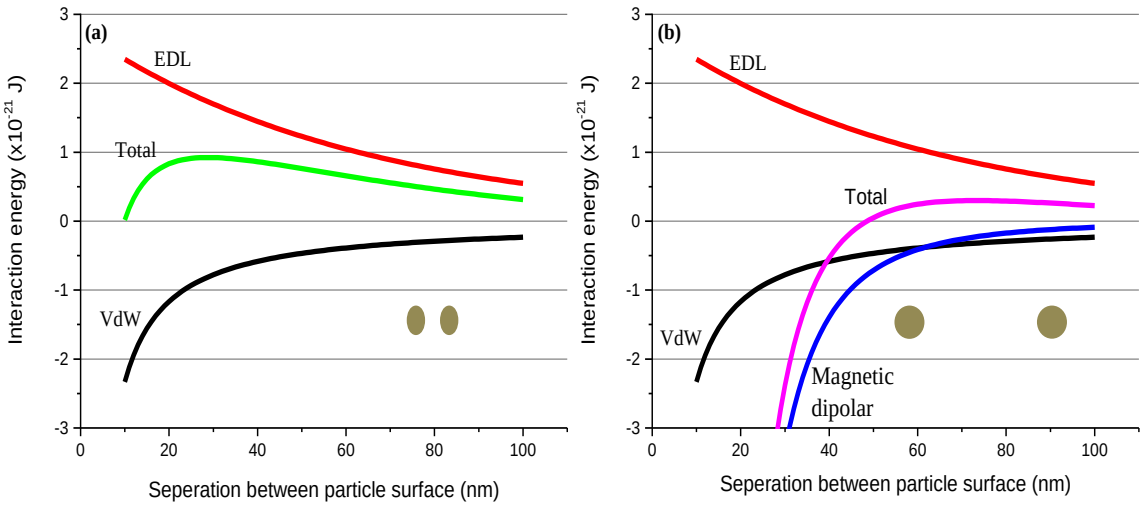

Figure 3.9: Attractive, repulsive and total interaction energies between two iron oxide nanoparticles of radius 8 nm through water at 300 K with all parameters as in figure 3.7. (a) Without the magnetic dipolar force included, the distance should be at least 10 nm. (b) With the magnetic dipolar force included, the distance should be at least 50 nm.

Figure 3.10 compares the attractive, repulsive and total interaction energies for two iron oxide and iron nanoparticles with a radius of 8 nm. As illustrated in figure 3.10, the distance between two iron nanoparticles should be at least 90 nm and compared with iron oxide it is nearly double. The reason for this is that the magnetic moment of pure iron nanoparticles is higher than that of iron oxide nanoparticles.

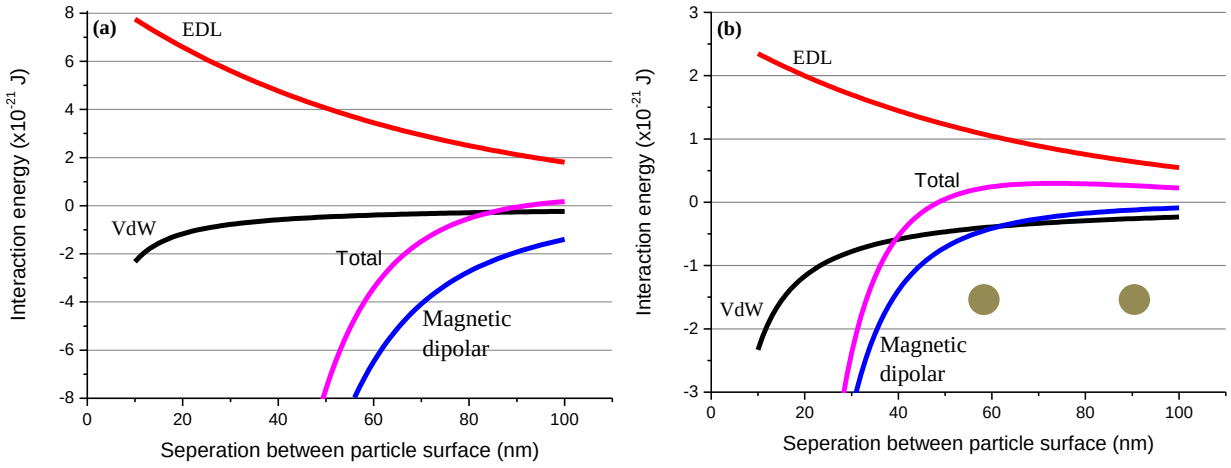

Figure 3.10: Comparing the attractive, repulsive and total interaction energies of 8 nm radius iron oxide and iron nanoparticles through water at 300 K with all the parameters as in the previous calculation except the zeta potential for iron nanoparticles which is 16 mV. (a) Total interaction becomes attractive at a separation of 90 nm for iron nanoparticles. (b) Total interaction becomes attractive at a separation of 50 nm for iron oxide nanoparticles.

The layout of EDL around the nanoparticles in suspension consists of stern layer (the charge bound strongly the surface), diffuse layer (counterion-rich region around the particle) which extends to slipping plane [Binns 2014 b]. The general consideration is that within slipping plane the ions in solution move with the particle, the ions beyond the slipping plane regarded as being within the bulk fluid. The zeta potential can be defined as the potential that exists at the slipping plane. The most important point when discussing the zeta potential is pH of the solution which can be varied to control the zeta potential. The influence of the zeta potential on the total interaction for iron nanoparticles with a diameter of 16 nm is shown in figure 3.11.

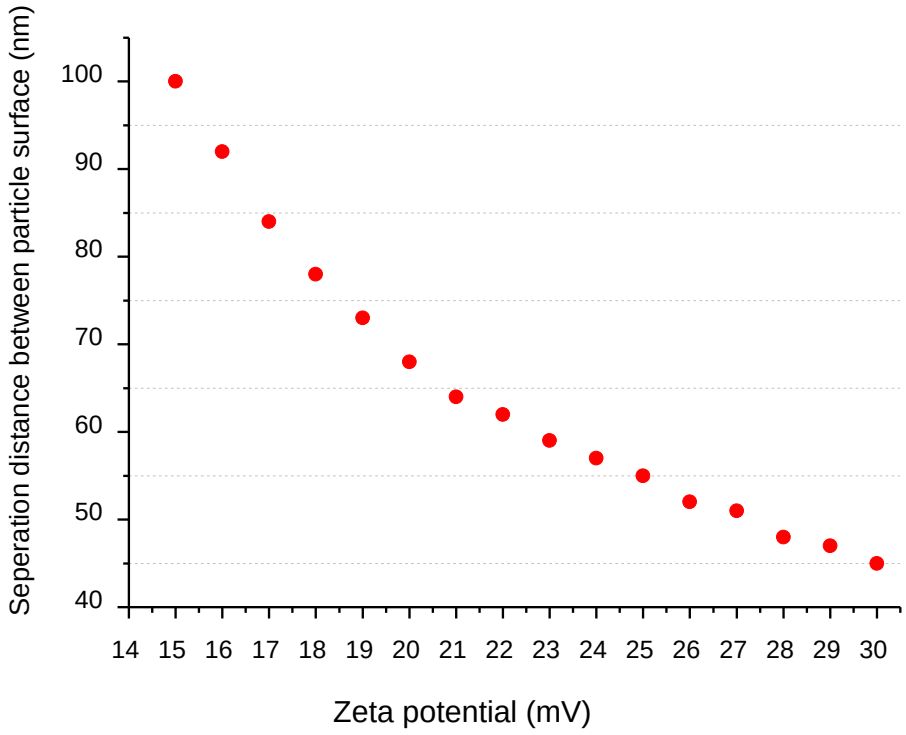

Figure 3.11: The influence of the zeta potential on the total interaction becoming attractive as a function of separation of two iron nanoparticles.

When the zeta potential increases, the separation distance between the nanoparticles to prevent particle agglomeration decreases. While the separation distance between two iron nanoparticles is 100 nm at a zeta potential of 15 mV, it reduces to 45 nm at a zeta potential of 30 mV. It is evident that the zeta potential has a significant effect on particle agglomeration.

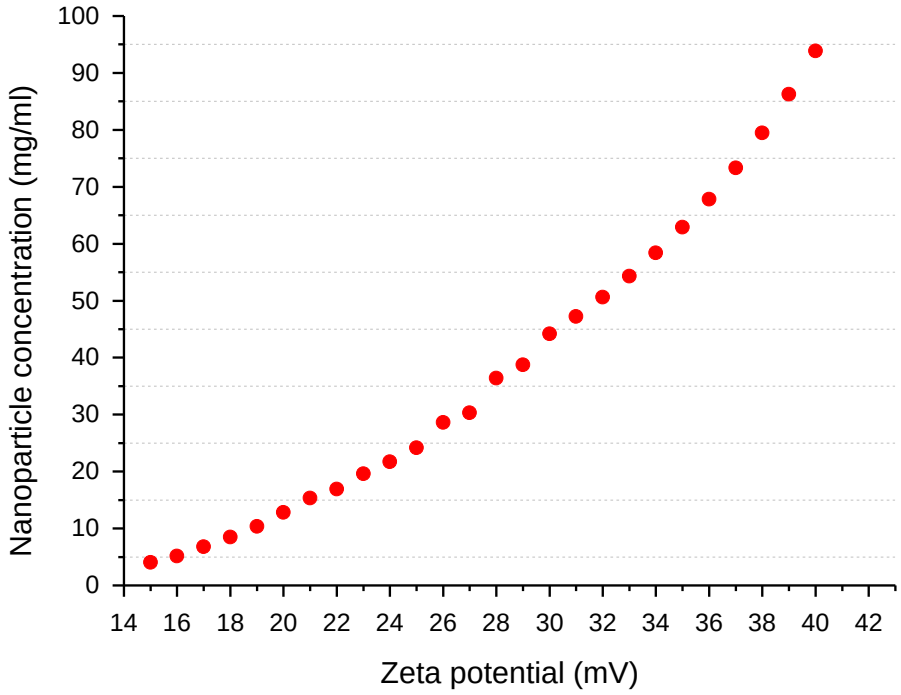

Figure 3.12: Fe nanoparticle concentration (mg/ml) versus zeta potential (mV)

Nanoparticle concentration is another vital aspect in particle stabilisation in suspension. Figure 3.12 demonstrates the required zeta potentials for various nanoparticle concentrations to stabilise Fe nanoparticles in suspension. For instance, while the required zeta potential is 16 mV for a 5 mg/ml nanoparticle concentration, it should be 40 mV for a 95 mg/ml nanoparticle concentration.

CHAPTER 4

Characterisation of Fe@FeO_x Nanoparticles

Magnetic nanoparticles have an increasing interest for many applications such as hyperthermia [Binns 2012, Binns 2010] and Magnetic Resonance Imaging (MRI) contrast agents [Tong 2010, Li 2013] in medicine due to their unique magnetic properties. For these applications, nanoparticles need to contain several layers. Ideally, a magnetic solid core a few nanometres across, which is coated with a layer to stabilise the nanoparticles in liquid suspensions.

Iron oxide (magnetite and maghemite) have been commonly produced nanoparticles for hyperthermia and MRI contrast agents by using various techniques [Hergt 2005, Mehdaoui 2010, Prushotham 2010, Bakoglidis 2012]. However, the downside of the iron oxide nanoparticles is their relatively low magnetisation under an Applied Magnetic Field (AMF). While the magnetic moment of pure iron per atom is 2.2 Bohr magneton (saturation magnetisation,M_S,~1.77×10^6 A/m) [Binns 2014 a], for Fe_2O_3, the magnetic moment is 0.6 Bohr magneton (saturation magnetisation,M_S,~4.5×10^5 A/m) [Fortin 2009]. So Fe@FeO_x nanoparticles are chosen for this project due to their pure iron core having a magnetisation that is four times higher than iron oxide. It is also worth mentioning that producing clean nanoparticles with a narrow size distribution in a liquid suspension is vital. Hence, all the nanoparticles analysed in this chapter were produced by an ultra-high vacuum (UHV) compatible gas aggregation source described in [Binns 2012] and summarised in chapter 2. This technique produces narrow size distribution of iron nanoparticles with a thin oxide shell.

This chapter describes the details of high-resolution Transmission Electron Microscopy (TEM) images of iron nanoparticles deposited directly onto the TEM grids and stabilisation of the nanoparticles within a liquid to prevent agglomeration by adding various surfactants. Also, UV-visible absorption spectra of some liquid suspensions will be presented.

4.1 TEM Analysis of Iron nanoparticles.

The iron core nanoparticles are formed in a sputter gas aggregation source in UHV conditions as explained in chapter 2. With this technique, it is possible to adjust the size distribution of the nanoparticles by varying the inert gas pressure and sputtering power. All the images presented here are from iron nanoparticles that were directly deposited on TEM grids in UHV conditions, followed by transfer through air into the microscope. The TEM study was carried out using the JEOL 2100 instrument in Leicester and also, for very high resolution work, the aberration-corrected JEOL 2200 FEG-TEM at the York-JEOL Nanocentre.

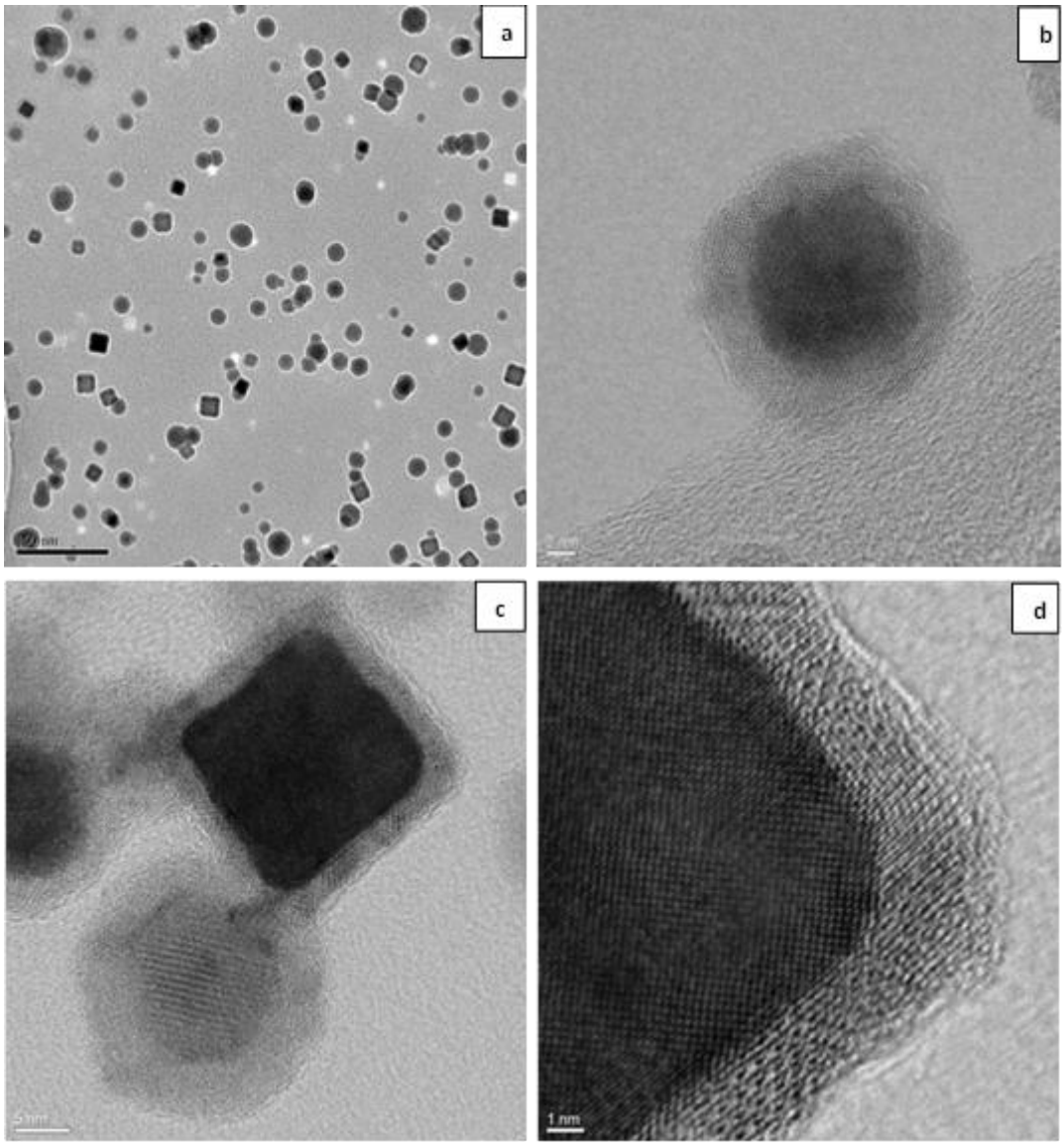

Figure 4.1: (a) TEM images of Fe@FeOx nanoparticles taken with the JEOL 2100 at Leicester. (b), (c) Aberration-corrected TEM images taken with the JEOL 2200 at York of a spherical and cubic nanoparticle respectively. (d) Details of the corner of a cubic nanoparticle showing a small corner facet. (Power = 20W, P_1 = 34 mbar, $P_3 = 2.0 \times 10^{-4}$ mbar, target position = 112 mm).

Figure 4.1 (a) is a TEM image taken with the JOEL 2100 at the University of Leicester of a sample that contains cubic and spherical shapes of nanoparticles. Figure 4.1 (b) and figure 4.1(c) are high-resolution images of spherical and cubic nanoparticles obtained using the aberration-corrected JEOL 2200 instrument at York, respectively. Figure 4.1 (d) demonstrates details of the cube corner. The oxide shell around the iron core might form naturally when the samples were transferred in air from the nanoparticle source to

the microscopes or another possibility is that oxidation might start in the chamber though UHV conditions (~10^{-9} mbar) due to high reactivity of pure iron nanoparticles. The details of the oxidation process with time have been reported in [Pratt 2014]. The general result of the TEM images is that the particles consist of a pure Fe metallic core and a thin (~2 nm) oxide shell.

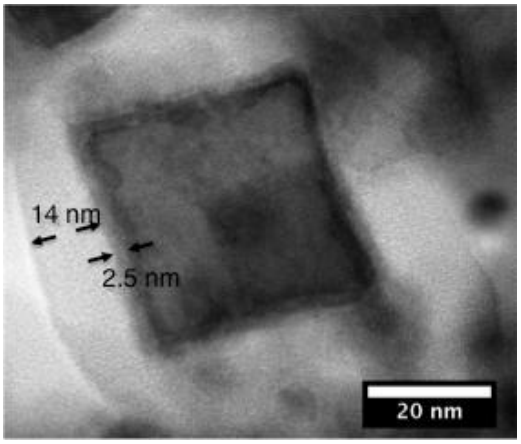

Figure 4.2: BF-STEM image of Fe nanoparticles extracted from water with DMSA and dried on a TEM grid showing a pure iron core, a thin oxide shell and a thicker surfactant shell [Binns 2012].

Figure 4.2 shows an aberration-corrected bright field STEM (BF-STEM) image of an Fe nanoparticle deposited into water with DMSA under UHV and dried on a TEM grid. The same structure of a pure iron core and an iron oxide shell is observed with a ~2.5 nm thick oxide shell and a 14 nm thick surfactant shell. It shows that the nanoparticle oxidation is similar for samples deposited in UHV and transferred through air and nanoparticles deposited into water and then dried. It is difficult to clarify when the nanoparticle oxidation starts (in the chamber or while microscope transfer), however, nanoparticles has a thin oxide shell around the pure iron core.

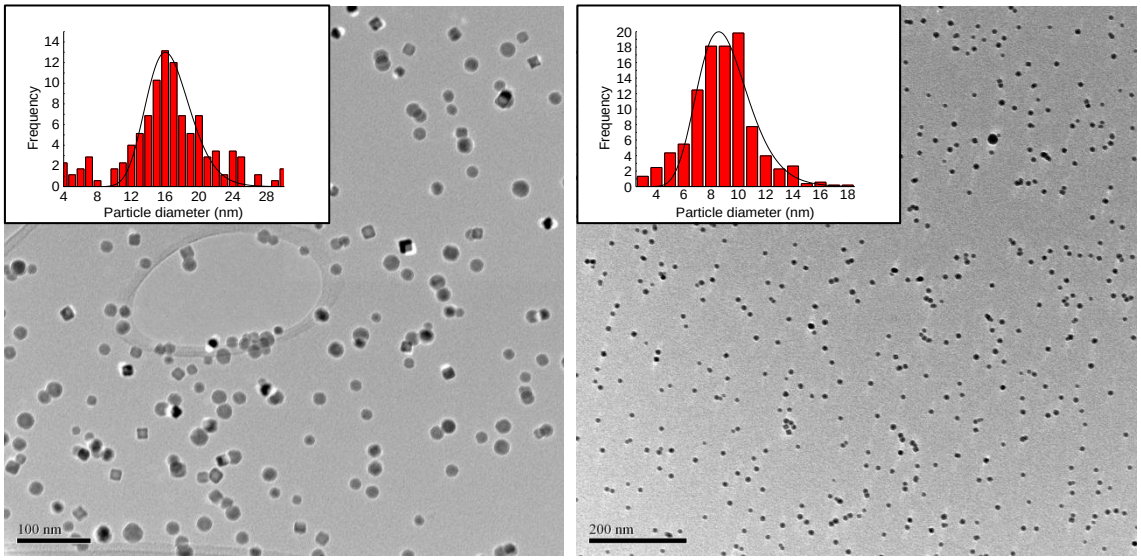

(a) (b)

Figure 4.3 (a) and (b) are TEM images taken with the JEOL 2100 at Leicester for samples deposited directly onto the TEM grid with water cooling to the sputter head on and off, respectively. The insets show the size distributions of nanoparticles.

Figure 4.3 (a) and (b) show that TEM images of iron nanoparticles deposited in vacuum directly onto a TEM grid with the water cooling to the sputter head on and off respectively with all other deposition conditions (pressure and power) kept the same. Leaving the water cooling off increases the temperature of the aggregation region though the value was not measured. TEM images were analysed using imageJ software and the log-normal size distribution was determined by using equation 4.1 (see below). While the water cooling is on, the most probable particle size is ~ 16 nm (181699 atoms), on the other hand it is about 8.55 nm (22712 atoms) when the water cooling is off.

Adjusting the size distribution of the nanoparticles in the gas-phase enables the production of superparamagnetic and ferromaganetic nanoparticles. According to equation 3.5, the small-size nanoparticles show superparamagnetic behaviour and should be easy to protect from agglomeration due to the lack of magnetic interactions

(see figure 3.9). However, the larger blocked particles are expected to have higher performance for hyperthermia treatment (see chapter 5).

4.2 Stabilisation and Size Distribution of Iron Nanoparticles in Liquid Suspension

For clinical applications, the nanoparticles must be dispersed in a liquid suspension. The method used to synthesise liquid suspensions of nanoparticles by co-deposition with water vapour from the gas phase in UHV conditions is detailed in [Binns 2012] and in chapter 2 but it is worth briefly explaining the production of liquid suspensions here. Before starting the particle deposition, water vapour was injected as a molecular beam into the vacuum chamber onto a substrate that was cooled with LN_2 to 77 K, and formed an ice layer. Then the Fe cores were formed in a sputtering gas aggregation source and were deposited within the ice matrix. The particle deposition rate was measured every 10 minutes and the suspension concentration was calculated as described in chapter 2 section 1.4.1. The water and nanoparticles depositions were continued until the required amount of sample was deposited and then the system was vented with clean nitrogen either while the ice was left in the chamber or knocked into another solution to melt outside the chamber.

A suspension should be stable against particle agglomeration in the presence of various attractive and repulsive interactions, which has already been explained in chapter 3 section 5. Untreated Fe particles in pure water quickly agglomerated hence different surfactants were added into the injected water in an attempt to passivate the nanoparticles and form stable suspensions. The substances tested included meso-2,3-Dimercaptosuccinic acid (DMSA), Ethylenediaminetetraacetic acid (EDTA), Polyethylene glycol (PEG), Polyvinylpyrrolidone (PVP), Poly(ethylene glycol) 2-

mercaptoethyl ether acetic acid (Thiol-PEG-carboxylate), dextran, detergents and sorbitol. Sorbitol and PVP were purchased from Fisher Scientific and eBay, respectively, and rest of the chemicals were purchased from Sigma Aldrich.

The size distribution of Fe@FeO_x hydrosols were measured by a Nanosight LM10 instrument which is described in chapter 2, section 3.1. In general, the size distribution of the nanoparticles has an asymmetric shape and has been fitted to a log-normal distribution of particle diameter, d:

$$f\ d\ \propto\ -\frac{(\ ln\ d\ -\mu)^2}{2\sigma^2} \qquad 4.1$$

where μ and σ are the mean and standard deviation of $ln\ d$,respectively, and are treated as fitting variables [Binns 2005]. The most probable diameter is calculated from $\exp(\mu)$ [O'Grady 1983]. Thereby, the log-normal distribution is applied to all Nanosight data and the most probable diameter is determined. The most probable diameter of the nanoparticles refers to the hydrodynamic diameter which includes the nanoparticle core and the surfactant shell.

4.2.1 Pure Water

Iron nanoparticles were deposited in pure water without any surfactants added by the already explained technique at a concentration of 1.0 mg mL^{-1}. As described before in the experimental chapter, to increase the particle concentration, the LN_2 tank was placed after the second aperture which produces an order of magnitude increase in the iron deposition rate (see figure 2.10). When the required amount of sample was deposited, the LN_2 was blown out from the trap and the ice on the substrate was knocked off into a petri dish containing some warm water after which the ice and pure water mixture was left to melt.

It was observed that the particles quickly agglomerated in pure water. The agglomeration process starts as soon as the ice melted. What's more, it was possible to see agglomerates by eye as tiny black specks. Consequently, the Nanosight LM10 measurements showed a heavily agglomerated sample from which it was impossible to measure a size distribution.

Another important feature that was observed is that the iron nanoparticles are hydrophobic. That means that agglomerated iron nanoparticles stayed on the surface of the water and never penetrated into the water

4.2.2 Detergent Coated Iron Nanoparticles

When the nanoparticles were deposited in pure water, it was proven that non-surfactant coated iron nanoparticles are hydrophobic. Therefore detergent (Teepol multipurpose) was added to the pure water and introduced into the chamber. Detergents are characterised as containing a hydrophilic head region and a hydrophobic tail region [Caligur 2008]. While the hydrophilic region of each molecule is oriented towards the water, the hydrophobic region is bounded to the hydrophobic iron cores.

The injected fluid was prepared by adding 0.22 g of detergent to 25 g of pure water. This solution was introduced into the system for approximately 1 hour before the start of particle deposition. Similarly to the pure water solution, the LN2 tank was placed after the second aperture. However, the ice was allowed to melt in a clean nitrogen atmosphere in the deposition chamber and the suspension was collected in a pre-placed petri dish with a detergent concentration of $1.0\ \mathrm{mg\ mL^{-1}}$.

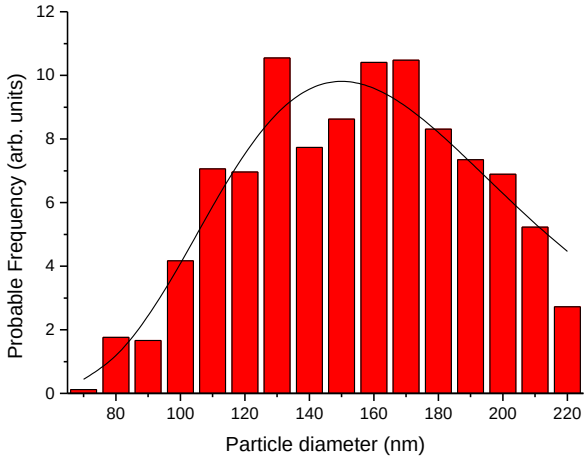

Figure 4.4: Iron nanoparticle size distribution in water which added detergent measured by the Nanosight LM10.

The size distribution of iron nanoparticles in suspension is illustrated in Figure 4.4. The most probable diameter is determined as 150 nm with a standard deviation of 0.94. The hydrodynamic diameter of the nanoparticles is larger than the particles in gas phase and shows that the particles are agglomerated. Even though detergent does not prevent agglomeration, it reduces it to a level so that the size distribution can be measured. Tiny small specks were still visible in solution but mostly the particles showed hydrophilic properties.

4.2.3 *meso*-2,3-Dimercaptosuccinic Acid (DMSA), Poly(vinyl pyrrolidone) (PVP), Ethylenediaminetetraacetic Acid (EDTA) Polyethylene glycol (PEG) and Dextran Coated Iron Nanoparticles

Dimercapto-succinic acid: $C_4H_6O_4S_2, M_w$ 182.22 (DMSA) has been employed to stabilise nanoparticles in liquid suspensions and increase the solubility in water [Fauconier 1997, Wilhelm 2003, Billotely 2003, Jun 2005 and Zhang 2009]. Thanks to the carboxylic chelate bonding DMSA forms a stable coating and also the SH group remains free, which allows bonding to targeting molecules [Fauconier 1997, Billotely

2003]. In the literature, nanoparticles are often coated with a layer of hydrophilic and biocompatible polymers such as, poly(vinyl pyrrolidone) (PVP) [Liu 2007, Lu 2008, Leng 2009 and Arsalani 2010], ethylenediaminetetraacetic acid (EDTA) [Warner 2010, Yi 2014], poly(ethylene glycol) (PEG) [Zhang 2002, Kohler 2004 and Shultz 2007] and dextran [Berry 2003, Laurent 2004, Gamarra 2005, Hong 2008, Yu 2012 and Easo 2013]. PVP is water soluble, non-toxic and adsorbs onto metals such as gold, silver and iron to increase the stability of the colloidal suspension [Graf 2003]. EDTA is water-soluble and a well-known chelator of toxic metals [Warner 2010]. PEG is hydrophilic, biocompatible and also increases the nanoparticles circulation time in tissue [Yu 2012]. Dextran is the first generation group of polymers and the most commonly used surfactant to stabilise particles against agglomeration.

By varying the ligands type, six samples were prepared as illustrated in table 4.1. Before being introduced into the UHV chamber, N_2 was bubbled through the DMSA solutions to deoxygenate them. The deoxygenated solutions were introduced to the substrate at 77 K, which was placed after the second aperture. An ice layer was deposited for approximately 1 hour before particle deposition.

The PVP coated iron nanoparticles were deposited as described on chapter 2 section 1.4 (see figure 2.8). The other surfactant-coated iron nanoparticles were deposited onto the LN_2 tank which was placed after second aperture to produce dense sample (see figure 2.10). When we had deposited the required amount of sample, the LN_2 tank was taken out of the chamber and we knocked off the ice/cluster area into the warm petri dish fluid which was placed in the fisher heater at 100 ℃.

Sample	Coating ligand	Ligands amount added to pure water (g)		Peak size (nm)	Concentration (mg/ml)	Collection method
		injection fluid (25 g)	Petri dish fluid (5 g)			
Fe@FeO_x	DMSA	0.05	0,05	30	1.4	Outside the chamber.
Fe@FeO_x	EDTA	0.4	0.4	23	2.0	Outside the chamber.
Fe@FeO_x	PEG	2.5	5	70	1.5	Outside the chamber.
Fe@FeO_x	DEXTRAN	0.05	0.07		1.5	Outside the chamber.
Fe@FeO_x	PVP	0.015		40	0.1	Inside the chamber.

Table 4.1:Fe@FeO_x nanoparticles deposited in liquid suspension by various ligand type and concentration technique.

Even though, newly-produced EDTA coated nanoparticles have the smallest peak size, the next day measurement showed that particles agglomerated and peak size increased to 140 nm. PVP and PEG coated nanoparticles agglomerated quickly same as the EDTA one. Also, dextran coated nanoparticles were completely agglomerated like the pure water sample. This made the size test impossible using the LM10 instrument.

The hydrodynamic diameter of DMSA coated nanoparticles is about 30 nm with a standard deviation of 0.33. Also, repeated size test shows that nanoparticles did not agglomerated over 10 days. DMSA-coated nanoparticles' behaviour in a cell culture was tested at the University of Liverpool by Dr. Lara Bogart. The results show that the particles did not aggregate when added to the culture medium. The mesenchymal stem cells with particles were incubated for 24 h. It was observed that during this time that

the particles did not aggregate or stick to the dish and most importantly the cells did not die. Also their further test to image the cells using magnetophoresis (cells are placed in a large magnetic field gradient (300 T/m) showed that the nanoparticles were completely oxidised and converted into a non-magnetic oxide.

These results prove that surfactants commonly used to coat iron oxide nanoparticles do not give a promising stabilisation with our technique. The reason could be that iron nanoparticles have a stronger magnetic attractive interaction than iron oxide. While to stabilise the iron oxide nanoparticles the distance between two nanoparticles should be approximately 40 nm [Binns 2014 b], for iron nanoparticles that have an iron core and iron oxide shell it is about 90 nm as shown in figure 3.9.

4.2.4 Poly(ethylene glycol) 2-mercaptoethyl Ether Acetic Acid (Thiol-PEG-carboxylate) Coated Iron Nanoparticles.

To keep the distance between two iron nanoparticles greater than 90 nm, thiol-PEG-carboxylate (M_n 3.500), which has a long PEG spacer providing steric stabilisation, was used. Also the presence of the carboxyl group should result in a negative surface charge.

The injection solution was prepared by adding 0.07 g of thiol-PEG-carboxylate to 20 g of deoxygenated pure water. The ice/cluster area was knocked off into a petri dish, which included 5 g of injection fluid at room temperature.

It was observed that the thiol-PEG-carboxylate did not work since most of the particles agglomerated. The difference from the other surfactants might be due to the large size of the thiol-PEG-carboxylate molecule. When the ice/cluster mixture starts melting, nanoparticles attract each other. The diffusion speed of the long chain molecules in

ice/water mixture could be smaller than the nanoparticles thus the coating process starts after agglomeration has already begun.

4.2.5 Sorbitol-Coated Iron Nanoparticles

After an ineffective attempt to coat nanoparticles with a long chain polymer, sorbitol, (M_w 182.18) which is a short chain polymer, was employed to coat nanoparticles due to its likely higher diffusion speed. Due to its higher solubility, 2.5 g of sorbitol was added to 25 g of deoxygenated water for injection water and 5 g of sorbitol added to 5 g of water for the petri dish fluid. The petri dish fluid was heated to approximately 60 ℃ before the ice/cluster area was added. It was observed that the temperature of the petri dish solution is critical since overheated sorbitol solution could be degraded. In addition, it was evident that using only sorbitol as a surfactant does not give a promising result to stop agglomeration. Hence after the ice melted, the solution was collected in a bottle and we added (1.2 mg 3M NaOH) to the solution. As shown in figure 4.5 the sorbitol-coated iron nanoparticles have a good size distribution with a 39 nm hydrodynamic diameter.

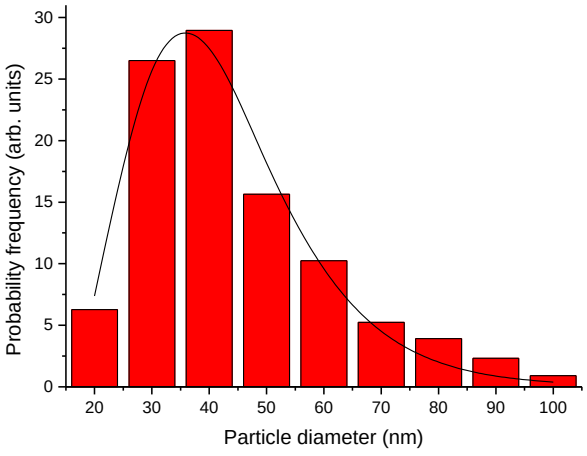

Figure 4.5: Size distribution of the sorbitol-coated iron nanoparticles.

It is probable that the short chain sorbitol molecules quickly attach to the nanoparticles and produce a shell around the particles. This shell brings the nanoparticle close enough to attract each other and the first impression is that it is not enough to prevent the agglomeration. On the other hand, adding the NaOH to the solution leads to an increase in the zeta potential which gives a higher repulsive force by charging the nanoparticles' surfaces. After that it was observed that the nanoparticles nicely dispersed in the solution.

4.3 UV-visible Measurement

UV-visible spectra were recorded on a Thermo Scientific Evolution 220 UV-visible Spectrophotometer. The absorption spectra of DMSA coated iron nanoparticles were obtained from a hydrosol which was produced same way explained in section 2.3.

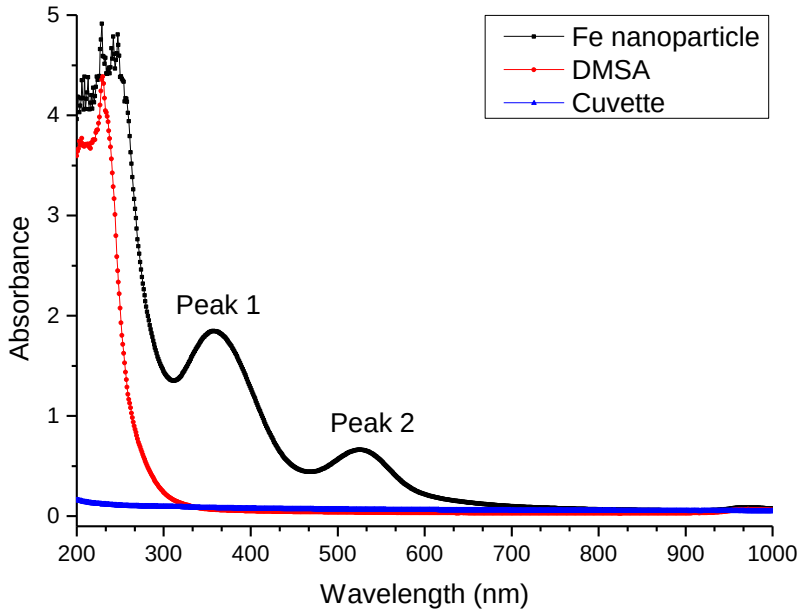

Figure 4.6: UV-visible spectra of Fe nanoparticles, DMSA and empty cuvette.

Figure 4.6 displays the UV-visible spectrum of iron nanoparticles (black line), DMSA solution (red line) and the empty cuvette (blue line). The iron nanoparticles in water

with added DMSA showed two absorption peaks at wavelengths of 356 and 525 nm. Similar UV-visible spectra have been observed in iron nanoparticles at 360 nm [Binns 2012] and at 327 and 357 nm [Guo 2001].

Iron nanoparticles dispersed in water with added DMSA solution were divided into three bottles to understand the effect of day-light and temperature on oxidation. One of these was stored in a fridge, the second one at room temperature and the final one was exposed daylight. UV-visible tests were repeated five, seven and fourteen days after production. The three batches of sample showed two peaks at the same wavelength as the original sample.

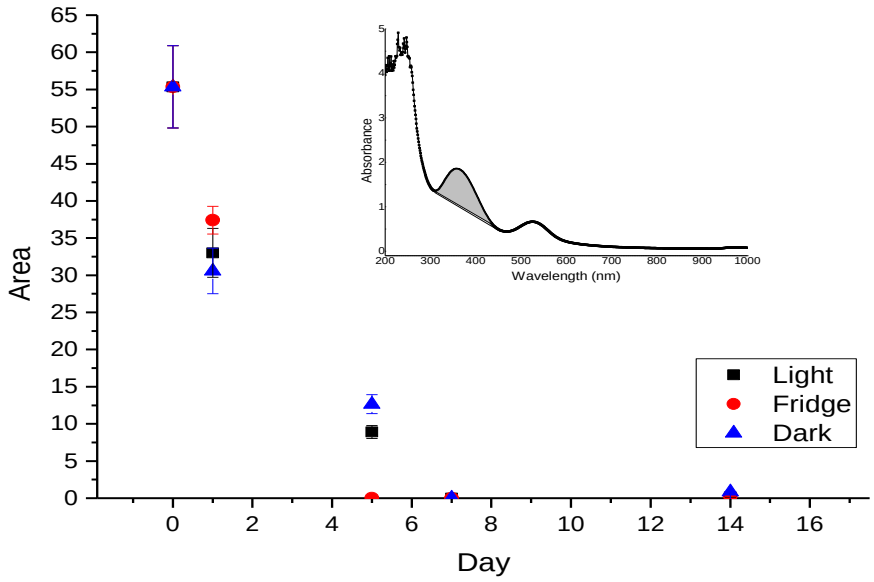

Figure 4.7: Area of the first absorption peak of iron nanoparticles that were stored in daylight, in the fridge and in the dark versus time.

Figure 4.7 illustrates the area of the first absorption peak of the three batches of sample that were kept in the dark, in daylight and in the fridge vs. time. The area of each peak was calculated as illustrated in the inset figure. The intensity of the first peak decreased with time and after seven days reached to zero. According to Guo 2001, the intensity of the absorption peak decreases with the oxidation of Fe nanoparticles. This result shows

that Fe nanoparticles oxidise with time and as described before display non-magnetic properties with the DMSA coating. Also it is worth mentioning that, here, daylight or temperature do not affect the oxidation of the nanoparticles.

In the meantime, the second peak areas were also calculated as shown in the inset in figure 4.8. The second absorption peak intensity behaves the same as the first one and reaches zero seven days later (see figure 4.8). The reason that two absorption peaks are observed could be due to nanoparticle shape since with our synthesis technique, it is possible to produce spherical and cubic nanoparticles in the normal deposition condition (see figure 4.1 (c)) . A shape dependence of the absorption spectra has been studied for silver and gold nanoparticles [Orendorff 2006, El-Brolossy 2008 and Amendola 2010] and it was proved that absorption spectra shift with shape changes.

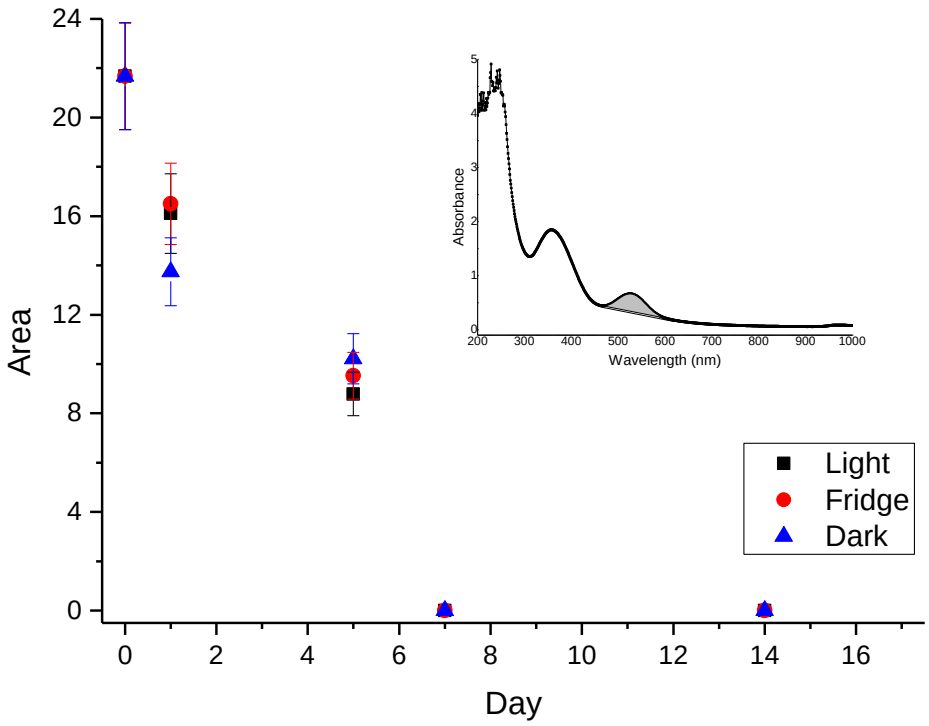

Figure 4.8: Area of the second absorption peak of iron nanoparticles that were kept in daylight, in the fridge and in the dark versus time.

To understand the oxidation dependence of the intensity of the absorption peaks, oxygen was introduced into (red spheres) and onto (black squares) the sample for one minute. This plots the area of the first peak as a function of the number of injections of pure oxygen each lasting 30 seconds for oxygen blown over the top of the sample and injected into the volume. After each oxygen injection, UV-visible spectra were measured. When the oxygen was injected onto the surface of the sample, the area of the absorption peak has a nearly stable trend. On the other hand, when exposed into the sample, it goes to zero as shown in figure 4.9.

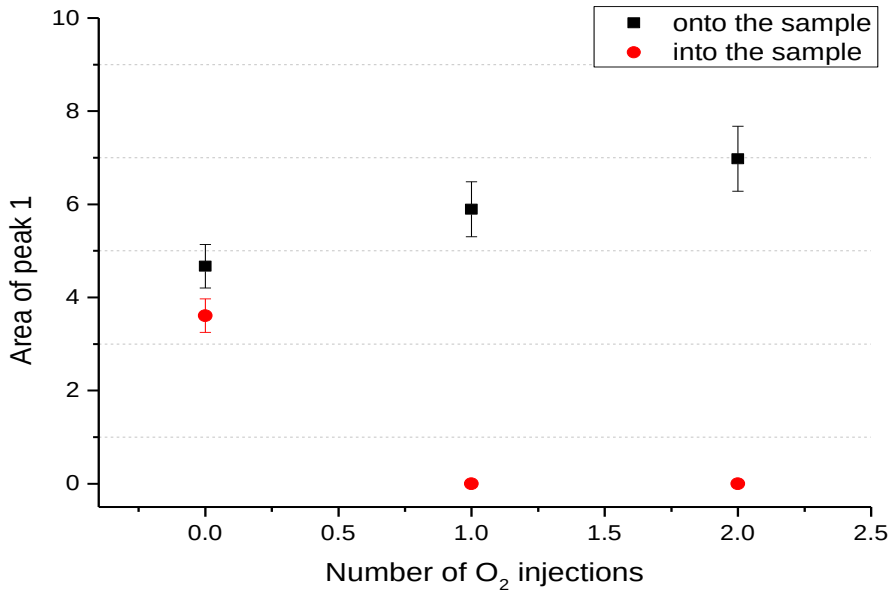

Figure 4.9: 0.05 mbar oxgyen was injected into the solution with hyperdemic syringe and bubled through the suspension. Also the oxgyn was injected surface of the suspension without any contact (onto the sample).

Even though the DMSA-coated iron nanoparticles appear not to agglomerate, they can oxidise easily and, according to the cell culture tests at Liverpool, transform to a non-magnetic iron oxide. The effect of the oxidation can be observed in figures 4.7, 4.8 and 4.9. The oxidation process is faster when the particles are directly exposed to oxygen as

shown in figure 4.9. It is clear that oxygen injected into the sample produces a rapid oxidation.

4.4 Conclusion

High-quality TEM images have demonstrated the production of clean iron nanoparticles using a UHV-compatible gas aggregation source. A thin oxide shell around the nanoparticles starts either while transferring the samples through the air or into the chamber under UHV conditions. Additionally, the source enables the synthesis of either superparamagnetic or ferromagnetic cubic and spherical shaped iron core/iron oxide shell nanoparticles. Although ferromagnetic nanoparticles have a higher heating ability for hyperthermia treatment, superparamagnetic nanoparticles could be easier to stabilise in suspension than ferromagnetic nanoparticles due to the lack of a magnetic interaction.

The results of the stabilisation of the nanoparticles in liquid suspension by adding different surfactants demonstrate that DMSA- and sorbitol-coated iron nanoparticles have small sizes and stabilise in water for a long time. On the other hand, even though DMSA-coated iron nanoparticles have a distinct UV-visible spectra in the first few days, due to rapid oxidation, they transform into a non-magnetic iron oxide. Hence they are not a good candidate for hyperthermia treatment or MRI contrast agents. It is believed that sorbitol with some NaOH is the most promising surfactant to coat the gas-phase produced nanoparticles and keep their magnetic properties over time. Additionally, commonly used surfactants for iron oxide nanoparticles do not stop agglomeration. This is because, as described in figure 3.10, the separation distance between two iron nanoparticles should be about four times larger than the iron oxide

nanoparticle diameter. Also, in the case of long chain molecules, before the surfactants attach to the nanoparticle surfaces, the particles could already be agglomerated.

In light of the above, to produce gas-phase synthesised iron nanoparticles for medical applications, it is essential to use a surfactant with a higher diffusion coefficient and, additionally, which should increase the zeta potential by varying the pH of the solution.

CHAPTER 5

Magnetic Properties and Heating Efficiency of Gas Phase Produced Fe@FeO_x Nanoparticles

Magnetic nanoparticles in liquid suspensions have attracted considerable attention in the treatment of tumours by heating. In hyperthermia treatment, magnetic nanoparticles are placed in an alternating magnetic field to heat the malignant tissue. The heating mechanisms of the nanoparticles have already been discussed in chapter 3 where it was shown that their heating efficiency depends on the size distribution, the saturation magnetisation, frequency and magnitude of the applied field and the anisotropy constant of the nanoparticles. However, the heating efficiency cannot be increased by increasing the frequency and amplitude of the magnetic field since this would cause an unwanted heating of healthy tissue (see chapter 3, section 3). So in order to obtain higher heating performance, the nanoparticles should have a high saturation magnetisation and a narrow size distribution.

In the last few years, there have been a number of attempts to produce magnetic nanoparticles in liquid suspensions which have a higher heating efficiency. Gas phase produced Fe@FeO_x nanoparticles are a promising candidate for hyperthermia treatment and Magnetic Resonance Imaging (MRI) contrast agents due to their high saturation magnetisation. The gas phase size distribution and stabilisation of the nanoparticles has already discussed in previous chapters. The most probable sizes of the particles in gas phase have been obtained from TEM images as 16 nm with the standard deviation of 0.2 and 8.55 nm with the standard deviation of 0.99 with water cooling to the sputter

head on and off, respectively. What is more, sorbitol-coated iron nanoparticles show a narrow size distribution and are readily dispersed in liquid.

Determining the Specific Absorption Rate (SAR) is the most useful way to understand the effectiveness of the nanoparticles in producing heat. It describes the ratio of the energy converted into heat per unit time and mass (W/g). Hence the heating efficiency of the nanoparticles will be presented as their SAR values at different conditions.

In this chapter, magnetometer measurements at 5 and 100 K of the sorbitol-coated Fe@FeO_x nanoparticles which were produced with the water cooling to the sputter head off under ultra-high vacuum (UHV) conditions will be discussed. Transverse MRI relaxivity of the sorbitol-coated Fe@FeO_x nanoparticles will be presented. Also SAR values will be determined and some comparison between the two different size distributions (16 and 8.55 nm) will be calculated by using the model described in chapter 3.

5.1 Magnetic Measurements of Sorbitol Coated Fe@FeO_x Nanoparticle

The magnetic properties of the nanoparticles are an important factor for hyperthermia. The most probable diameter of the nanoparticles in the gas-phase and after coating with sorbitol in a liquid suspension along with the concentration of the solution were described in chapter 4. Also, as already demonstrated by the commercial ferrofluid heating test to calibrate the RF heater in the experimental chapter (see section 2.2.3), the lower limit of the concentration required to measure a sensible SAR value should be at least 0.06 mg/ml for the sample if its SAR is about 100 W/g. Hence in order to determine the magnetic properties of the nanoparticles and also size and concentration of the solution, magnetic measurements of the Fe@FeO_x nanoparticles stabilised with

sorbitol coating were performed by using the SQUID at the Demokritos institute in Greece.

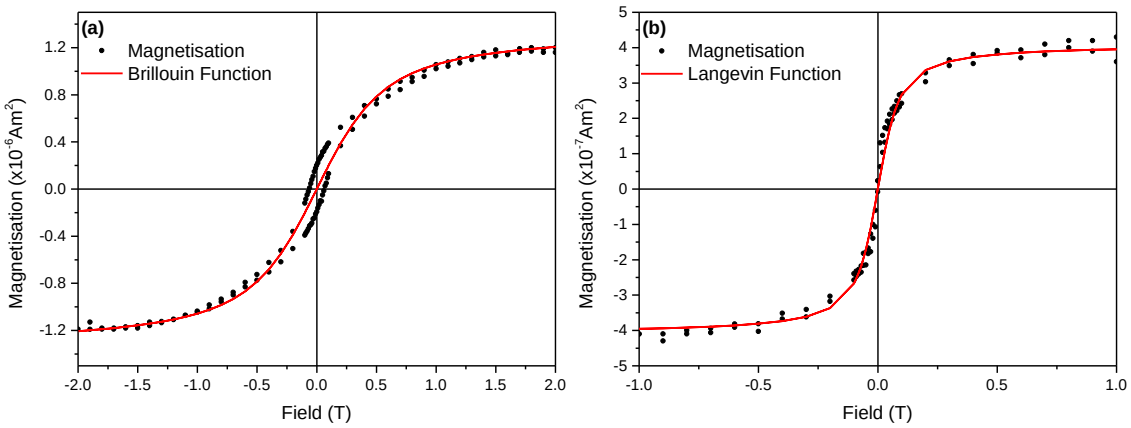

Figure 5.1: Magnetisation of the sorbitol-coated Fe@FeO$_x$ nanoparticles in water at (a) 5 K and (b) 100 K.

Figures 5.1 (a) and (b) show the magnetisation of the sorbitol-coated Fe@FeO$_x$ nanoparticles in liquid suspension at a temperature of 5 and 100 K, respectively. At 100 K, the sample saturates at a field amplitude of 1 T but at 5 K full saturation is not achieved at 2 T. In general, nanoparticles are much easier to saturate since they have larger moments as compared to atoms. Also, at 100 K nanoparticles show superparamagnetic behaviour (no remanent magnetisation and no coercive field) with a fitted Langevin function as shown in figure 5.1 (b) (red line) using equation 3.8 with the diameter of the nanoparticles and the saturation magnetisation treated as fitting parameters. The diameter of the single nanoparticles is determined to be approximately 3.5 nm (from TEM analysis, it is 8.55 nm) by fitting the Langevin function with the saturation magnetisation of 4.1×10^{-7} Am^2. Determining the saturation magnetisation enables us to calculate the concentration of the sample by using the measured sample volume which is 60×10^{-9} m^3 yielding approximately 0.03 mg/ml.

The calculated diameter of the nanoparticles from the magnetisation measurements refers to the size of the Fe core. According to the TEM analysis, the most probable diameter of the nanoparticles has been determined to be 8.55 nm with a pure iron core and a thin oxide shell. However, it is probable that even though coating the nanoparticles with sorbitol prevents the particle agglomeration, it probably does not uniformly coat the particles surface to stop oxidation. Thereby oxidation increases with time and leads to a thicker oxide layer which has a weak magnetisation or is magnetically dead. Before discussing the effect of having a small pure iron core on heating efficiency, it is worth mentioning the concentration of the solution since it has a vital importance in determining the SAR and MRI response of the nanoparticles. As already described in the experimental chapter, the sample concentration was calculated by measuring the flux every 10 min with the XTM and recording the amount of the injected water into the deposition chamber. Despite the fact that the calculated size concentration is 1.5 mg/ml, from magnetic measurements it is determined to be 0.03 mg/ml. Thus, there is a significant difference between the measured and calculated concentration. Beside this, as shown in figure 5.1 (a), at 5 K the sample does not saturate even though it reaches a magnetisation that is three times higher than that measured at 100 K. A Brillouin function was fitted to the magnetisation curve as shown in figure 5.1 (a) with the magnetic moment and saturation magnetisation used as fitting parameters. The saturation magnetisation was found to be $\sim 1.32 \times 10^{-6}$ Am^2 and the magnetic moment was found to correspond to very small Fe clusters (between 4-8 atoms) which is possible because there are certain configurations of very small clusters that are particularly stable [Datta 2011]. Moreover, what is more likely is that the small moment comes from larger particles (8.55 nm) of a non-magnetic oxide that get a very small moment (equivalent of a few Fe atoms) from uncompensated spins at the surface.

Hence, although the reason why there are very small clusters in solution is not clear, it could explain the difference between the measured and calculated concentration. Besides this while collecting the nanoparticles from the petri dish or tank some of them might be lost. However, the measured concentration is about 98% less than the calculated concentration; in general it is expected to be majority of the calculated concentration since ice/cluster area knocked into the petri dish.

Also the larger (3.5 nm) nanoparticles present ferromagnetic properties in the hysteresis loop at 5 K as shown in figure 5.1 (a). The natural coercive field (H_K) of the particles was measured to be 60 mT ($\sim 4.77 \times 10^4$ A/m). The anisotropy constant *(K)* of the nanoparticles was calculated using equation 3.17 and found to be 5.31×10^4 J/m^3 which is close to the anisotropy value of bulk iron (5.00×10^4 J/m^3).

The sorbitol coated Fe@FeO_x nanoparticle sample was analysed by Dr. Mark Horsfield of the MRI unit at the University of Leicester Royal Infirmary to determine its performance as a contrast agent in MRI diagnosis. Relaxation rates were measured as a function of the concentration of the sample. It has already been determined from magnetic data that our sample includes 3.5 nm nanoparticles with a concentration of 0.03 mg/ml and some small iron Fe@FeO_x clusters, which will not contribute to the relaxivity. Thus the concentration of the solution was assumed to be 0.03 mg/ml in our calculations.

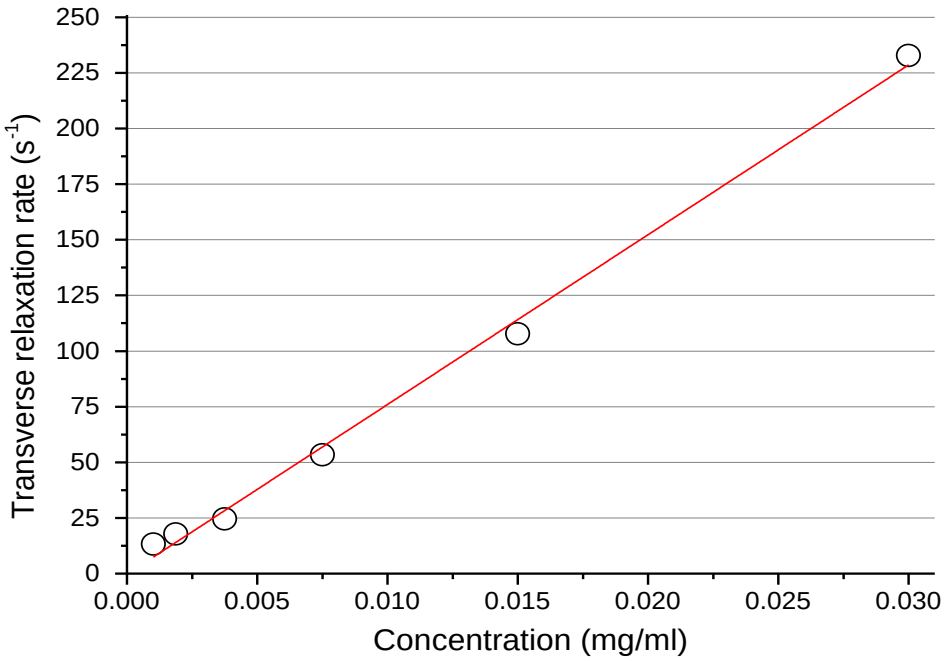

Figure 5.2: Transverse relaxation rate versus concentration of sorbitol-coated Fe@FeO$_x$ nanoparticles.

Figure 5.2 shows the transverse relaxation rate of the sorbitol-coated Fe@FeO$_x$ nanoparticles as a function of concentration. The transverse relaxation value of the nanoparticles was calculated to be approximately $425\ \mathrm{mM^{-1}s^{-1}}$ from the slope of the relaxivity increase with concentration by doing the necessary conversions from mg/ml to mM. The relaxivity of nanoparticles depends on the size and saturation magnetisation of the nanoparticles as expressed in equation 3.25. The relaxivity of the clinically available Fe nanoparticle (Resovist®) is $82\ \mathrm{mM^{-1}s^{-1}}$ [Reimer 2003] which is five times less than sorbitol coated Fe@FeO$_x$ nanoparticle.

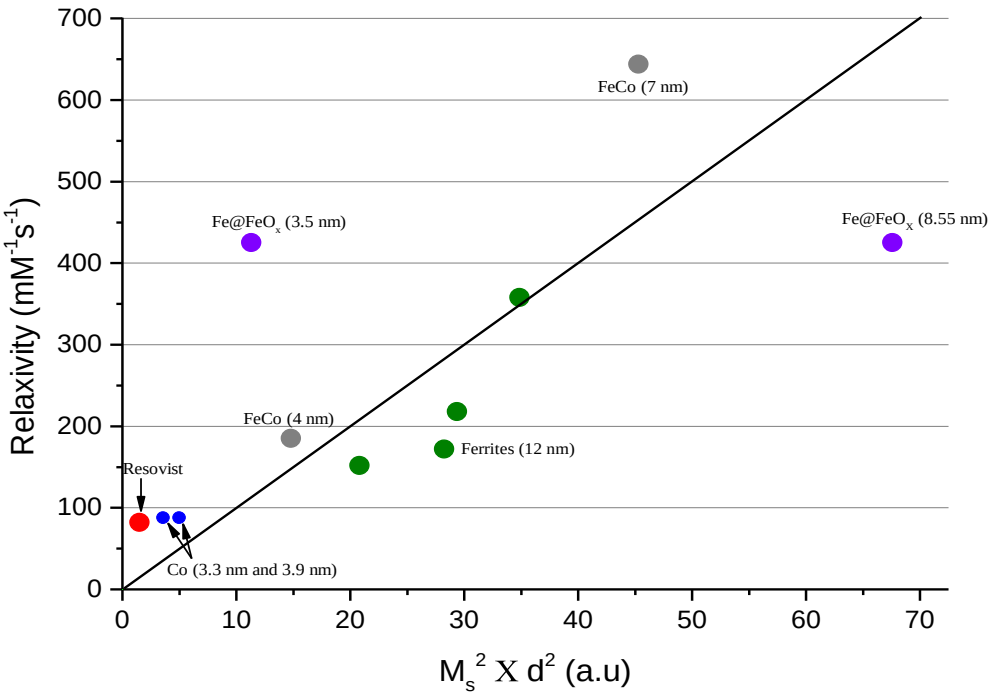

Figure 5.3: Relaxivity of different magnetic nanoparticles versus $M_S^2 \times d^2$ [Binns 2014 b]. Red circles: 5-25 nm core diameter Resovist® nanoparticles (M_s = 55 emu/g) [Reimer 2003]; Grey circles: 4 and 7 nm core diameter FeCo nanoparticles (M_s = 215 emu/g) [Seo 2006]; Blue circles 3.3 and 3.9 nm diameter Co nanoparticles (M_s = 88 emu/g) [Parkes 2008]; Green circles: 12 nm diameter nanoparticles of spinel ferrites of different composition and saturation magnetisation [Lee 2007]; Purple circles: 3.5 and 8.55 nm core diameter of sorbitol coated Fe@FeO$_x$ nanoparticles (M_s = 215 emu/g) produced at Leicester.

Figure 5.3 shows the relaxivity of various nanoparticles with different sizes and saturation magnetisations reported in the literature and as shown previously [Binns 2014 b] the relaxivity is approximately proportional to $M_S^2 \times d^2$. Also shown are the 3.5 and 8.55 nm core diameter sorbitol-coated Fe@FeO$_x$ nanoparticles (M_s = 215 emu/g). All the nanoparticles presented in Figure 5.3 have a higher saturation magnetisation than Resovist® so show higher relaxivity. What's more, the sorbitol-coated Fe@FeO$_x$ nanoparticles show the highest relaxivity after 7 nm FeCo nanoparticle.

The reason that two different core sizes (3.5 and 8.55 nm) of Fe@FeO_x nanoparticles are presented is due to the time gap between the MRI and magnetic measurements of the sample. The size distribution of the nanoparticles determined from TEM images is 8.55 nm. The magnetic measurements of the nanoparticles were done one month after the MRI test, which in turn was performed one month later after the production of the nanoparticles. During this period, according to the magnetisation data, the core size shrinks due to oxidation so the size lies somewhere between 3.5 nm and 8.55 nm and is thus close to the expected value represented by the linear fit. In summary, the Fe@FeO_x nanoparticles show a high MRI relaxivity and protecting them from oxidation (from example by coating the core with another metal-see chapter 6) will increase their performance further.

5.1.1 SAR Measurements of the Sorbitol Coated Fe@FeO_x Nanoparticles

The heating measurements of the nanoparticles were taken using the RF heaters which have already been described in the experimental chapter. However, the SAR value was not accurately measurable due to the size and concentration of the nanoparticles. According to the heating mechanisms of the nanoparticles (see chapter 3, section 2), the SAR value of the 3.5 nm iron nanoparticles (that is, the value after a period of oxidation) was calculated to be 3 W/g. This assumed the measured K value of 5.31×10^4 J/m^3 and H_K value of 4.77×10^4 A/m with the saturation magnetisation of bulk iron ($M_S = 1.77 \times 10^6$A/m), the fluid viscosity of water (~8.89×10^{-4} Pa.s at 25 ℃), the amplitude of the magnetic field (10 kA/m) and a frequency of 100 kHz. In order to measure heating from a sample with an SAR of 3 W/g, the lowest limit of the concentration should be 2 mg/ml. Repeating the calculation for particles with a

diameter of 8.55 nm (i.e. the size in the gas-phase) gives an SAR of 6 W/g, which to be measurable requires a concentration of at least 1 mg/ml.

The size and concentration of the sample make the heating efficiency measurement of the nanoparticles impossible by using our RF heaters. In general, it could be possible to get a high SAR from 8.55 nm diameter nanoparticles by applying a higher field and frequency (discussed in next section). The main reason for producing the nanoparticles with a smaller size is to keep the nanoparticles in suspension by reducing the magnetic dipolar interaction since producing iron nanoparticles in a liquid suspension without agglomeration is vital.

5.2 Modelling the SAR of the Gas-Phase-Produced Fe@FeO_x Nanoparticles.

Due to the difficulty of measuring the SAR at the concentrations in our samples, the heating efficiency will be discussed with reference to the model described in chapter 3. In all SAR calculations, a value of 3×10^{-3} Pa.s and 310 K were used for the fluid viscosity [Binns 2012] (approximately the value for blood) and human body temperature, respectively. Also, the measured natural coercive field (H_K) of 4.77×10^4 A/m, anisotropy constant of 5.31×10^4 J/m^{3}and saturation magnetisation of bulk iron ($M_s = 1.77 \times 10^6$ A/m) were used.

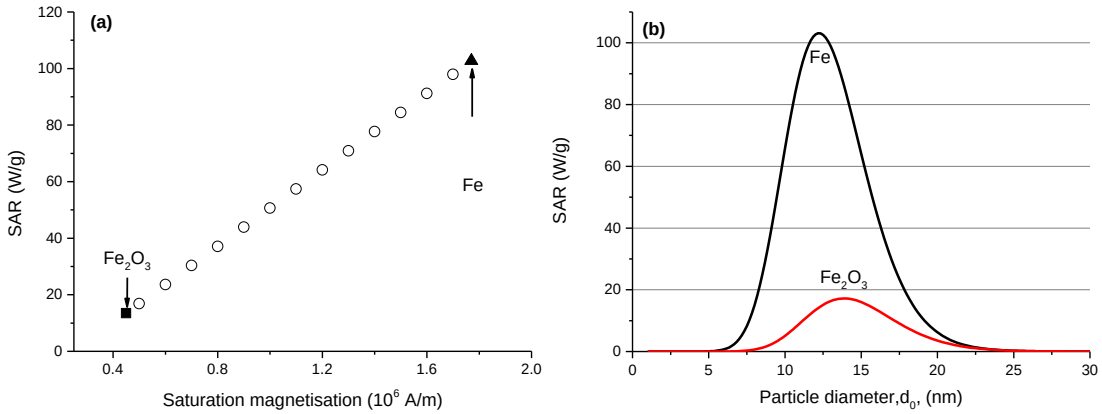

Figure 5.4: Calculation of the SAR of the Fe and Fe_2O_3 nanoparticles (a) Dependence of SAR on the saturation magnetisation, M_S, of the material in the nanoparticles. To calculate the SAR of the iron oxide nanoparticles, an anisotropy constant of $3 \times 10^4\ \mathrm{J/m^3}$ and a saturation magnetisation of $4.5 \times 10^5\ \mathrm{A/m}$ was used while for iron nanoparticles, the values were $5.31 \times 10^4\ \mathrm{J/m^3}$ and $M_s = 1.77 \times 10^6\ \mathrm{A/m}$ (bulk Fe). The excitation field was 100 kHz at 4850 A/m. For the M_S values between Fe_2O_3 and pure Fe, the K value and material density were interpolated between the end points (b) SAR of the Fe nanoparticles (black line) and Fe_2O_3 nanoparticles (red line) as a function of particle diameter, d_0.

The saturation magnetisation of the nanoparticles is the best starting point to explain the dependence of SAR on the particle parameters. It also clarifies the reason for the choice of iron nanoparticles in hyperthermia application rather than the iron oxide nanoparticles. Figure 5.4 (a) shows the dependence of the SAR of Fe and Fe_2O_3 nanoparticles of the same size (d_0~maximum at a specific particle size) with the same standard deviation (0.2) on the saturation magnetisation. To calculate the SAR of the iron oxide nanoparticles, the anisotropy constant of $3 \times 10^4\ \mathrm{J/m^3}$ and saturation magnetisation of $4.5 \times 10^5\ \mathrm{A/m}$ were used. The frequency and the amplitude of the magnetic field are 100 kHz and 4850 A/m, respectively. It is clearly observed that a high saturation magnetisation is a key requirement to obtain high SAR.

Additionally figure 5.4 (b) shows the SAR which was calculated with the same parameters already given above, of the Fe and Fe_2O_3 nanoparticles as a function of particle diameter d_0. The SAR of both Fe and Fe_2O_3 nanoparticles reaches its maximum and starts decreasing again at a frequency of 100 kHz and magnetic field of 4850 A/m. The calculation clearly demonstrates the importance of having a narrow size distribution to obtain a high SAR. It is evident that the heating efficiency of the Fe nanoparticle is much higher than Fe_2O_3 nanoparticle at all particle diameters. This demonstrates the importance of our method which enables the production of nanoparticles with a pure iron core and a thin oxide shell.

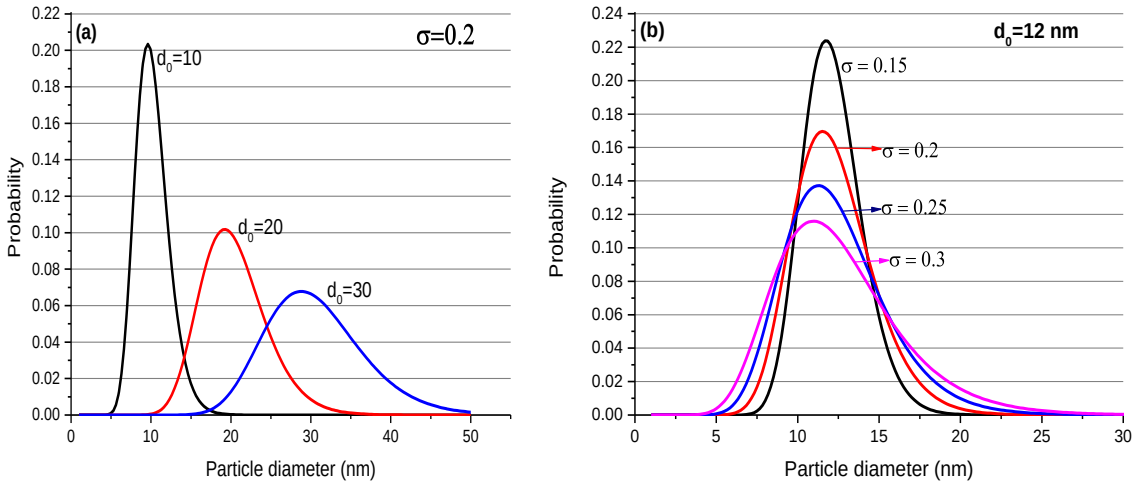

Figure 5.5: Log- normal size distributions plotted for (a) d_0 = 10, 20 and 30 nm with $\sigma = 0.2$ (b) σ =0.15, 0.2, 0.25 and 0.30 for $d_0 = 12$ nm.

The particle diameter in the figures represents the peak of a log-normal distribution rather than a single particle size. The size distribution of the gas-phase produced nanoparticles is determined by fitting the log-normal distribution, so, as illustrated in figure 5.5 (a), d_0 represents the maximum size of the distribution. The standard deviation is another important parameter to characterise the size distribution and its

affect on the log-normal size distribution is illustrated in figure 5.5 (b) for nanoparticle assemblies with d_0= 12 nm and various σ values.

As already explained in the theoretical chapter, it is possible to calculate the SAR of the nanoparticles from the superparamagnetic to the blocked state. Three heating mechanisms generate heat according to the size of the nanoparticles. These are susceptibility heating (P_{sus}) for superparamagnetic nanoparticles, hysteresis heating (P_{hyst}) for blocked nanoparticles and a stirring heating after the absence of the hysteresis heating for bigger nanoparticles. There is not any equation to calculate the stirring heating but it is worth comparing the percentage of P_{sus} and P_{hyst} in the total heating to underline the effect of the size distribution of the nanoparticles on SAR.

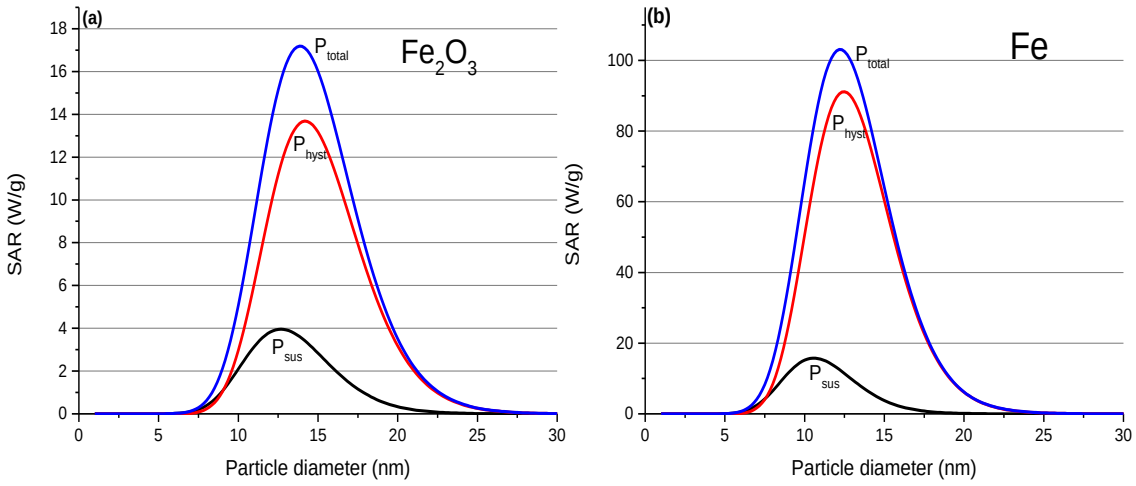

Figure 5.6: The contribution of the susceptibility and hysteresis heating on the total SAR. Calculation of SAR by using the same parameters as above for (a) Fe_2O_3 nanoparticle. (b) Fe nanoparticle.

Figure 5.6 (a) and (b) show P_{sus} , P_{hyst} and total heating power in W/g for Fe_2O_3 and Fe nanoparticles as a function of the most probable diameter, d_0,of the particles, respectively. The SAR of Fe and Fe_2O_3 were calculated by using the same parameters given above. It is evident that the majority of the heating is generated by P_{hyst} for both

Fe and Fe_2O_3 nanoparticles and the contribution to the SAR from susceptibility heating is very small. Hence the heating efficiency of the superparamagnetic nanoparticles is much less than that of blocked nanoparticles.

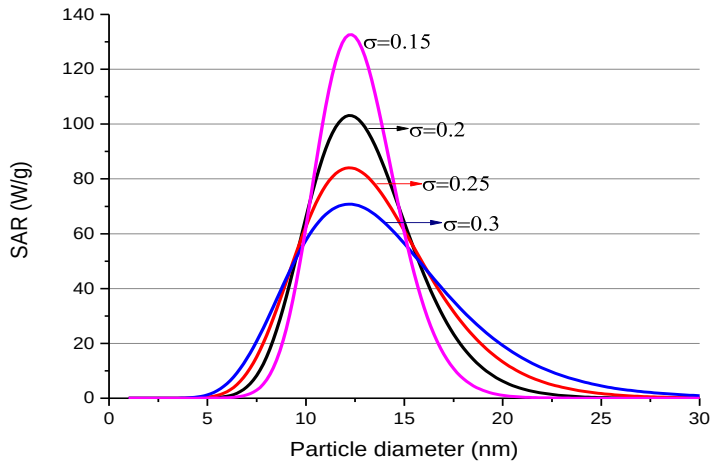

Figure 5.7: Calculation of SAR of the nanoparticles as a function of the size parameter, d_0 for different values of the standard deviation, σ.

The width of the size distribution has a significant effect on the SAR of the nanoparticles. Figure 5.7 shows the SAR of the Fe nanoparticles calculated using the same parameters as above as a function of the most probable size, d_0, for the standard deviation, σ varying from 0.15 to 0.3. It is evident that increasing σ decreases the SAR. So to optimise heat generated for hyperthermia treatment, producing nanoparticle suspensions with a narrow size distribution is necessary.

The anisotropy constant of the Fe@FeO_x nanoparticles has been calculated to be approximately 5.31×10^4 J/m^3 (close to the bulk value 5.0×10^4 J/m^3) from the magnetic measurements. Also a higher anisotropy constant ($= 2 \times 10^5$ J/m^3) was measured before for 2 nm Fe nanoparticles [Binns 2002 b]. Thereby it is worth determining the effect of the anisotropy constant of the particles on their SAR.

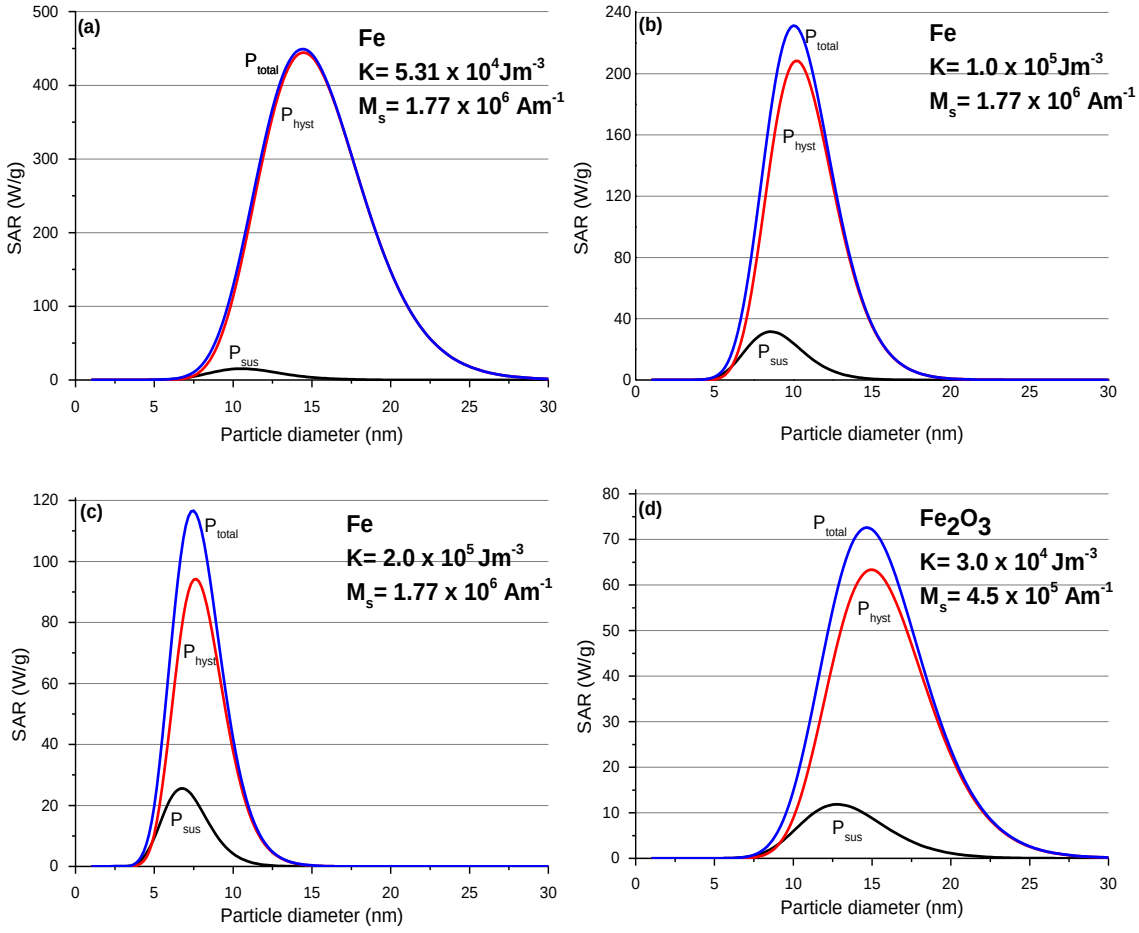

Figure 5.8: Calculation of the SAR as a function of particle diameter for Fe_2O_3 and Fe for different values of the anisotropy constant, *K* in an applied field $H_0 = 100$ kA/m and f = 100 kHz. A value of 1.77×10^6 A/m and 4.5×10^5 A/m were used for the saturation magnetisation of Fe and Fe_2O_3, respectively and a value of 0.2 was used for the standard deviation of the size distribution for both. (a) $K = 5.31 \times 10^4$ Jm^3, (b) $K = 1.0 \times 10^5$ Jm^3, (c) $K = 2.0 \times 10^5$ Jm^3(d) $K = 3.0 \times 10^4$ Jm^3 for Fe_2O_3.

Figure 5.8 shows the calculation of the SAR as a function of particle diameter for Fe_2O_3 with $K = 3.0 \times 10^4\ Jm^{-3}$, and Fe with $K = 5.31 \times 10^4\ Jm^{-3}$, $K = 1.0 \times 10^5\ Jm^{-3}$ and $K = 2.0 \times 10^5\ Jm^{-3}$. The frequency and the magnitude of the Applied Magnetic Field (AMF) were 100 kHz and 10000 A/m, respectively. Even though, the field and frequency product is higher than the Atkinson-Brezovich limit and on the edge of the safe region (see figure 3.7), it would be suitable for brain tumours. The other parameters for Fe and Fe_2O_3 nanoparticles were the same as used above. It is clear that the SAR value for Fe reduces significantly with increasing anisotropy constant. It also changes the diameter at which peak power occurs. It means that when the anisotropy constant increases, the smaller size produces a higher peak. In general, although the heating power of the nanoparticles drops with increasing anisotropy constant, it is still much higher than Fe_2O_3 nanoparticles at the highest anisotropy constant. Moreover, the SAR of the sorbitol-coated Fe@FeO_x nanoparticles with the anisotropy constant of $K = 5.31 \times 10^4\ Jm^{-3}$ is about 445 W/g which is seven times higher than the SAR of the Fe_2O_3 (~ 72 W/g). It is obvious that Fe nanoparticles with the lower anisotropy constant lead to significant improvements in the effectiveness of hyperthermia.

The heating efficiency of the nanoparticles depends either on the particle parameters (size distribution, anisotropy constant and saturation magnetisation) or the amplitude of the applied field for hyperthermia treatment. For Fe and Fe_2O_3 nanoparticles, the dependence of particle parameters has already been discussed. So it is worth discussing the field and frequency dependence for 8.55 and 16 nm size Fe nanoparticles which were produced by the gas aggregation source and also their effectiveness for hyperthermia treatment.

The SAR of the Fe@FeO$_x$ nanoparticles with the size distribution of 8.55 (standard deviation, $\sigma = 0.99$) and 16 nm (standard deviation, $\sigma = 0.2$) determined from TEM images (see chapter 4 section 2) were calculated by varying the field and frequency of the AMF while keeping constant the product of the field and frequency at the values $H_0 \times f = 4.85 \times 10^8\ \mathrm{Am^{-1}s^{-1}}$ (Atkinson-Brezovich limit) and $H_0 \times f = 1.0 \times 10^9\ \mathrm{Am^{-1}s^{-1}}$ (suitable for brain tumours). For example at 100 kHz the field amplitude is 4850 A/m for $H_0 \times f = 4.85 \times 10^8\ \mathrm{Am^{-1}s^{-1}}$ and 10000 A/m for $H_0 \times f = 1.0 \times 10^9\ \mathrm{Am^{-1}s^{-1}}$.

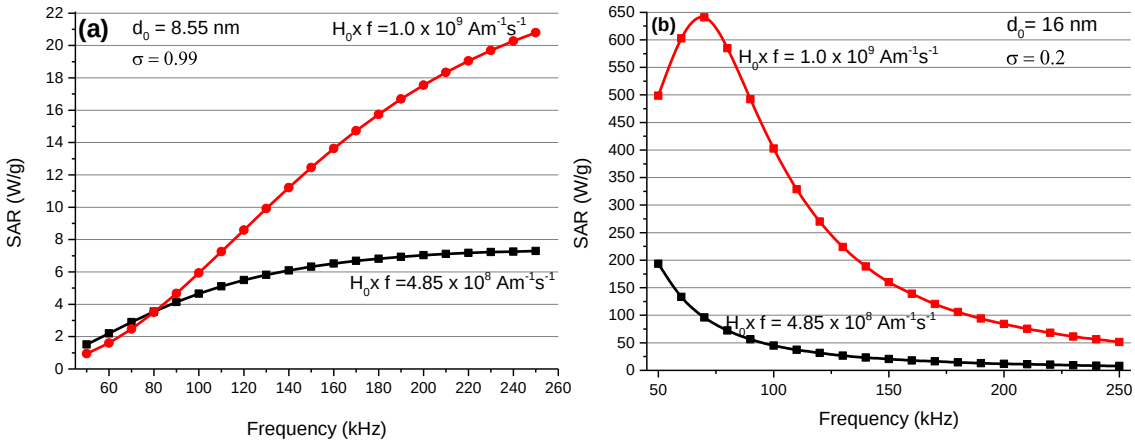

Figure 5.9: Calculation of the SAR of Fe@FeO$_x$ nanoparticles versus frequency of the AMF while keeping constant the product of the frequency and field amplitude ($H_0 \times f$) at $4.85 \times 10^8\ \mathrm{Am^{-1}s^{-1}}$ (black line) and $1.0 \times 10^9\ \mathrm{Am^{-1}s^{-1}}$ (red line). (a) Nanoparticles have a log-normal size distribution with d_0 = 8.55 nm and $\sigma = 0.99$ (b) Nanoparticles have a log-normal size distribution with d_0 = 16 nm and $\sigma = 0.2$.

Figure 5.9 shows the frequency and field dependence of the 8.55 nm and 16 nm diameter, d_0, Fe@FeO$_x$ nanoparticles produced by the gas aggregation technique. The heating performance of the nanoparticles, at the smaller size distribution is not promising for hyperthermia treatment even at the higher product of the frequency and field as illustrated in figure 5.9 (a). The main reason for the small SAR of the 8.55 nm

nanoparticles is that the majority of the nanoparticles are superparamagnetic. In general the generated heat by superparamagnetic nanoparticles is much less than the blocked particles as shown in figure 5.8. It is also clear that susceptibility heating is proportional to the frequency of the applied field so it shows an increasing trend as the frequency increases. However, the main reason for the production of the smaller nanoparticles is that stabilisation of the superparamagnetic nanoparticles in liquid suspension is much easier than for blocked nanoparticles.

On the other hand, doubling the most probable size in the distribution of the nanoparticles from 8.55 nm to 16 nm leads to a significant increase in the heating performance of the nanoparticles as shown in figure 5.9 (b). When the product of the frequency and field is at the Atkinson-Brezovich limit (black line), the maximum SAR (~194 W/g) is observed at the lowest frequency. At the higher safe limit ($H_0 \times f = 1.0 \times 10^9$ $\mathrm{Am^{-1}s^{-1}}$), the effect of the frequency and field on the heating performance of the nanoparticles is obvious since the SAR of the nanoparticles increases to 640 W/g at $f = 70$ kHz and $H_0 = 14.3$ $\mathrm{kAm^{-1}}$. It is observed that SAR reaches a peak value at 70 kHz and starts decreasing again. The reason for this behaviour is that for frequencies between 50 and 70 kHz, the field amplitude is high enough to flip all the spins in the size distribution and so the heating power increases with frequency. Above 70 kHz, the amplitude is not sufficiently high to flip all the particles and the proportion of particles able to respond to the applied field decreases with frequency hence the reduction in SAR. For the lower field frequency product, the field amplitude even at 50 kHz is not high enough to flip all the spins so only a decrease is observed with increasing frequency.

To compare the performance of our materials with other reported material for hyperthermia treatment is a problem due to the different fields and frequencies used. Determining the Intrinsic Loss Parameter (ILP) which is independent of the AMF parameters could be a way but it is only appropriate for the susceptibility heating mechanism which has a minor contribution to the total heat generated. A new way has been suggested to compare the performance of the materials by scaling to $H_0 \times f = 4.85 \times 10^8$ Am^{-1}s^{-1} for all samples [Binns 2014 b].

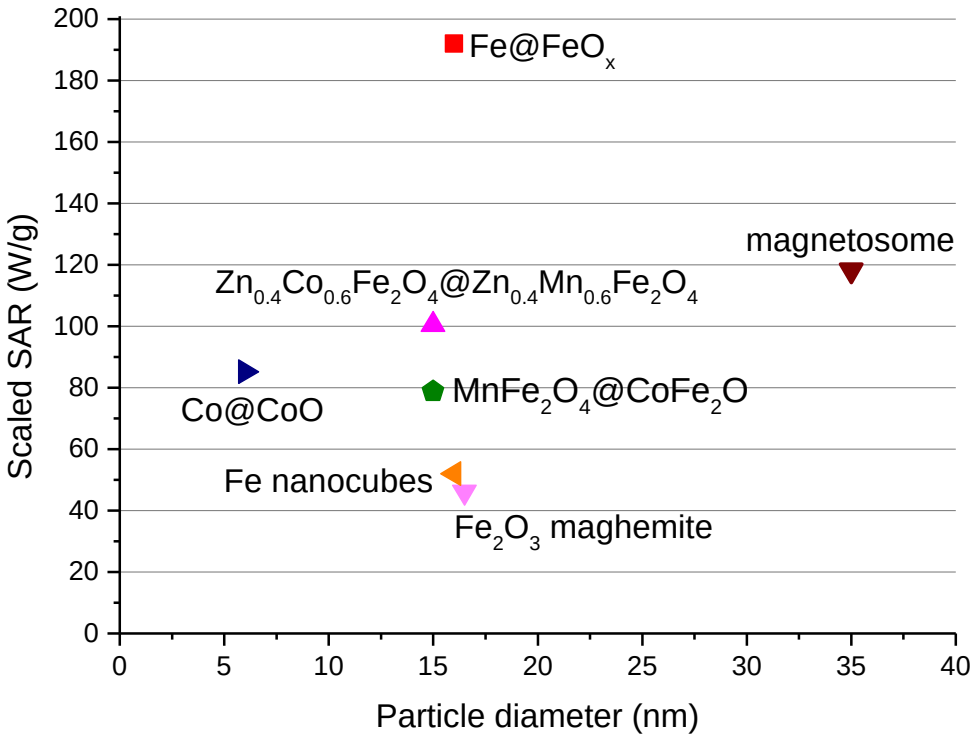

Figure 5.10: Scaled SAR value of selected high-performance nanoparticles as a function of particle diameters to compare with Fe@FeO$_x$ nanoparticles.

Figure 5.10 shows the scaled SAR values of selected high-performance nanoparticles as a function of particle diameter to compare their performance with Fe@FeO$_x$ produced by the gas aggregation technique with a diameter of 16 nm. Size, reported SAR values, frequency and magnitude of the AMF for the selected nanoparticles are listed in table

5.1. While the reported SAR values of the nanoparticles are much higher than the Fe@FeO_x nanoparticles, their scaled SAR values are smaller when scaling the amplitude of the AMF. As illustrated in figure 5.10, all the materials have higher SAR values than maghemite. What's more, while the highest SAR of the selected nanoparticles is 118 W/g for magnetosomes, the SAR of the Fe@FeO_x nanoparticles is 192 W/g. It is clear that gas phase produced Fe@FeO_x nanoparticles may produce enough heat for an effective hyperthermia treatment. It also reduces the required amount of nanoparticles to be injected into human body.

Nanoparticles	Size (nm)	H_0 (kA/m)	f (kHz)	Reported SAR (W/g)	Scaled SAR (W/g)	Reference
Fe@FeO_x	16	9.7	50	192	192	Our sample
Fe nanocube	16	52.5	300	1690	52	[Mehdaoui 2010]
Fe_2O_3 maghemite	16.5	24.8	700	1650	48	[Fortin 2007]
Fe magnetosome	35	10	410	1000	118	[Hergtz 2006]
$CoFe_2O_4@MnFe_2O_4$	15	37.3	500	2280	59	[Lee 2011]
$MnFe_2O_4@CoFe_2O_4$	15	37.3	500	3034	78	[Lee 2011]
Co@Co oxide	6	10	410	720	85	[Bönnemann 2013]
$Zn_{0.4}Co_{0.6}Fe_2O_4@$ $Zn_{0.4}Mn_{0.6}Fe_2O_4$	15	37.3	500	3866	100	[Lee 2011]

Table 5.1: Reported and scaled SAR values of high-performance nanoparticles with the AMF parameters

5.3 Conclusion

According to the magnetic measurements of sorbitol-coated Fe@FeO_x nanoparticles, it is clear that sorbitol did not uniformly coat the highly reactive iron surface so the nanoparticles oxidised, which eroded the pure iron core from 8.55 nm to 3.5 nm within two months. However, one month after particle production, the transverse relaxivity of nanoparticles was measured to be $425\ \mathrm{mM^{-1}s^{-1}}$ which is five times higher than clinically available Fe-oxide nanoparticles (Resovist ®). According to the linear relationship between the relaxivity and $M_S{}^2 \times d^2$, the diameter of the nanoparticle should be 6-7 nm. It is evident that the oxide shell around the Fe core was about 2 nm one month after production and increased to 4.5 nm after a further two months.

Also, it is observed that the concentration of the solution is much less than the calculated concentration and contains some small (4-8 atoms) nanoparticles or fully oxidise nanoparticles with the diameter of 8.55 nm. The anisotropy constant of the nanoparticles was determined to be $5.31 \times 10^4\ \mathrm{J/m^3}$ which is close to the anisotropy value of bulk iron ($5.00\times 10^4\ \mathrm{J/m^3}$).

Modelling the SAR of the Fe@FeO_x nanoparticles shows that the contribution of hysteresis heating to the total power is much higher than susceptibility heating. Hence, nanoparticles should have a narrow size distribution with the most probable diameter of 12-16 nm range to obtain a higher performance for effective treatment. Also comparing the gas-phase produced Fe@FeO_x nanoparticles with reported nanoparticles which have a high SAR value illustrates that Fe@FeO_x nanoparticles have the highest scaled SAR value and will produce the highest heating for treatment.

Accurate measurement of the heating efficiency of the sorbitol-coated Fe@FeO_x nanoparticles with the diameter of 8.55 nm by the RF heater was not possible due to the low SAR value and the low concentration. However, the modelled SAR of the Fe@FeO_x nanoparticles with a diameter of 16 nm at the Atkinson-Brezovich limit shows that the SAR of the Fe@FeO_x nanoparticles is five times higher than Fe oxide nanoparticles. Moreover, at the higher field and frequency product ($H_0 \times f = 1.0 \times 10^9\ \mathrm{Am^{-1}s^{-1}}$ that is assumed to be safe for brain tumours), it is possible to increase SAR of the nanoparticle to 600 W/g. The higher heating efficiency means a lower particle concentration can be injected into tumour tissue.

In summary, if problems (biocompatibility stability of suspension and enough particles collected in solution) can be solved, gas phase produced nanoparticles with a narrow size distribution may enable hyperthermia treatment as an effective cancer treatment technique without any negative side effects. What's more, the transverse relaxivity of the Fe@FeO_x nanoparticles could be increased by preserving the pure iron core against oxidation.

Chapter 6

Core-Shell Structure and Shape of the Nanoparticles

Core-shell nanoparticles are gradually attracting more attention due to their modified properties. Core-shell magnetic nanoparticles consist of a magnetic core encapsulated in a protective shell. The shell material could be magnetic with a different hardness such as Fe@FeO_x, which has already been demonstrated in chapter 4 (with the oxidation process naturally occurring) or non-magnetic such as Au [Sun 2006, Chung 2014] and Ag [Lu 2010]. Producing pure iron nanoparticles in ultra-high vacuum (UHV) conditions using the gas phase synthesis technique provides an important advantage in hyperthermia treatment due to the higher magnetic moment. Unfortunately, pure iron nanoparticles without a coating cannot be used for biomedical applications for the following reasons: Fe nanoparticles are highly toxic, can easily agglomerate and rapidly oxidize. Furthermore, the oxidation process will weaken their magnetic moment. Hence, it is clear that Fe nanoparticles need to be coated in situ so that they retain their magnetic moment, remain nontoxic, biocompatible and chemically stable. Also, for the biomedical applications the coating facilitates surface functionalization by attaching biological molecules to transfer the particles into the human body and increase their lifetime in circulation.

In general, coating of the core material improves the surface modification, functionality and stability of nanoparticles. The properties could be modified by changing the constituting material or core-to-shell ratio [Chaudhuri 2012]. Ag has been one of the popular coating materials due to its biocompatibility and non-toxicity. Also, Ag-coated iron nanoparticles are more resistant to oxidation compared to the uncoated particles. In general core-shell nanoparticles with a pure iron core and a uniform silver shell

combine a high magnetic moment with the strong surface plasmon resonance of Ag. These multifunctional properties of nanoparticles enable them to be employed for diagnostic imaging and treatment of cancer at the same time. For instance, the multifunctional Fe@Ag nanoparticles, modified with surface functionalization could be used firstly to attach to the cancer tissue and then to image by utilising the surface plasmon resonance of Ag and then kill the tumour by magnetic hyperthermia.

The optical, magnetic and electrical properties of the nanoparticles show differences relative to the bulk properties. These unique properties depend on not only size but also the shape of the materials. Furthermore, the influence of the magnetic nanoparticles can be increased by controlling their shape, similar to the size control, for hyperthermia treatment or other medical applications. The size of the nanoparticles produced by the gas aggregation technique can be varied by adjusting the sputter power, gas pressure and position of the sputter head. With this technique, it is also possible to produce different shapes of the nanoparticles by annealing them under UHV conditions.

In this chapter, core-shell nanoparticles having a Cu and an Fe core coated with a Ag shell, and also effect of the annealing the Fe@FeO_x particles in UHV, will be presented. Ag has been chosen as the shell material since previous work [Binns 2012] shows that Ag nanoparticles can be stabilised in solution with DMEDA. Also it is biocompatible and enables the attachment of targeting molecules on the surface of the nanoparticles.

6.1 Cu@Ag Core-Shell Nanoparticles

As described in chapter 2, after the cores are formed in the sputtering gas aggregation source, nanoparticles pass through a heated crucible containing the shell material. The

mass increase of the particles due to the coating has been observed by using the quadrupole mass filter.

Producing Cu nanoparticles with a high flux is much easier than the Fe nanoparticles so this was done initially to test the system, before producing the Fe@Ag nanoparticles. A Cu target was placed in the sputter head and the Cu nanoparticles passed through the hot crucible, which contained Ag.

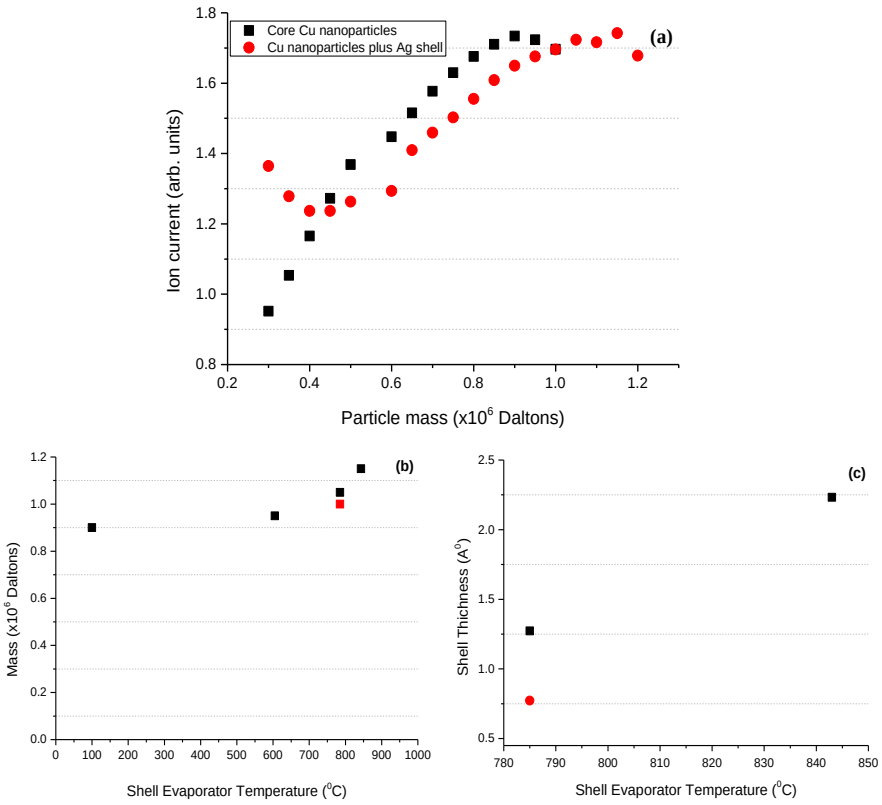

Figure 6.1: (a) Mass spectra for core Cu nanoparticles and after coating with a Ag shell. (b) Peak of the mass spectrum of the Cu nanoparticle passed through the hot crucible at different temperatures. The black squares show data obtained on the upward temperature sweep and the red square shows the peak value after cooling again to a given temperature. (c) Shell thickness of the Ag-coated Cu nanoparticles versus shell evaporator temperature. Red and black squares as for (b).

Figure 6.1 (a) and (b) illustrate the shift in the mass of the nanoparticles after coating with Ag and the mass increase of the nanoparticles as a function of the shell evaporator

temperature, respectively. The black squares in Figure 6.1 (a) represent the mass spectrum for the core Cu particles recorded with the shell evaporator off and red spheres represent the change in the mass spectrum with the Ag shell evaporator heated to 843 ℃. The uncoated core nanoparticles have a most probable mass of 925,000 Daltons, which corresponds to about 14,600 atoms with a diameter of 6.9 nm (assuming the bulk density). After passing through the hot crucible, the core material was coated with the Ag and the mass increased to 1,150,000 Daltons, which corresponds to about 2000 Ag atoms. As shown in figure 6.1 (b), the shift in the mass spectrum depends on the shell evaporator temperature. At higher temperatures, the amount of evaporated shell material is more, so the number of shell atoms increases. Additionally when the hot crucible is cooled down to 785 ℃, the peak mass in the spectrum, which is represented by the red square in figure 6.1 (b), has a good agreement with the value obtained at the same temperature during the upward temperature sweep.

Figure 6.1 (c) displays the shell thickness of the Ag-coated Cu nanoparticles with a diameter of 6.9 nm. It is observed that at 785 ℃ evaporator temperature, a 1.2 Å Ag shell (~ 1160 Ag atoms) is deposited around the particles and when the temperature is increased to 843 ℃ , the shell thickness reaches 2.2 Å (~2000 Ag atoms). When the shell evaporator temperature goes back to 785 ℃ again, the shell thickness drops to 0.07 Å. The reason for having two different shell thicknesses at the same temperature is that the amount of the shell material in the hot crucible might decrease with time.

6.2 Fe@Ag Core-Shell Nanaoparticles

After the encouraging results from the Cu@Ag core-shell nanoparticles, Fe@Ag core-shell particles were produced with the same technique. However, due to a technical

problem with the thermocouple connected to the crucible, instead of the shell evaporator temperature, the power supply current has been used in the plots.

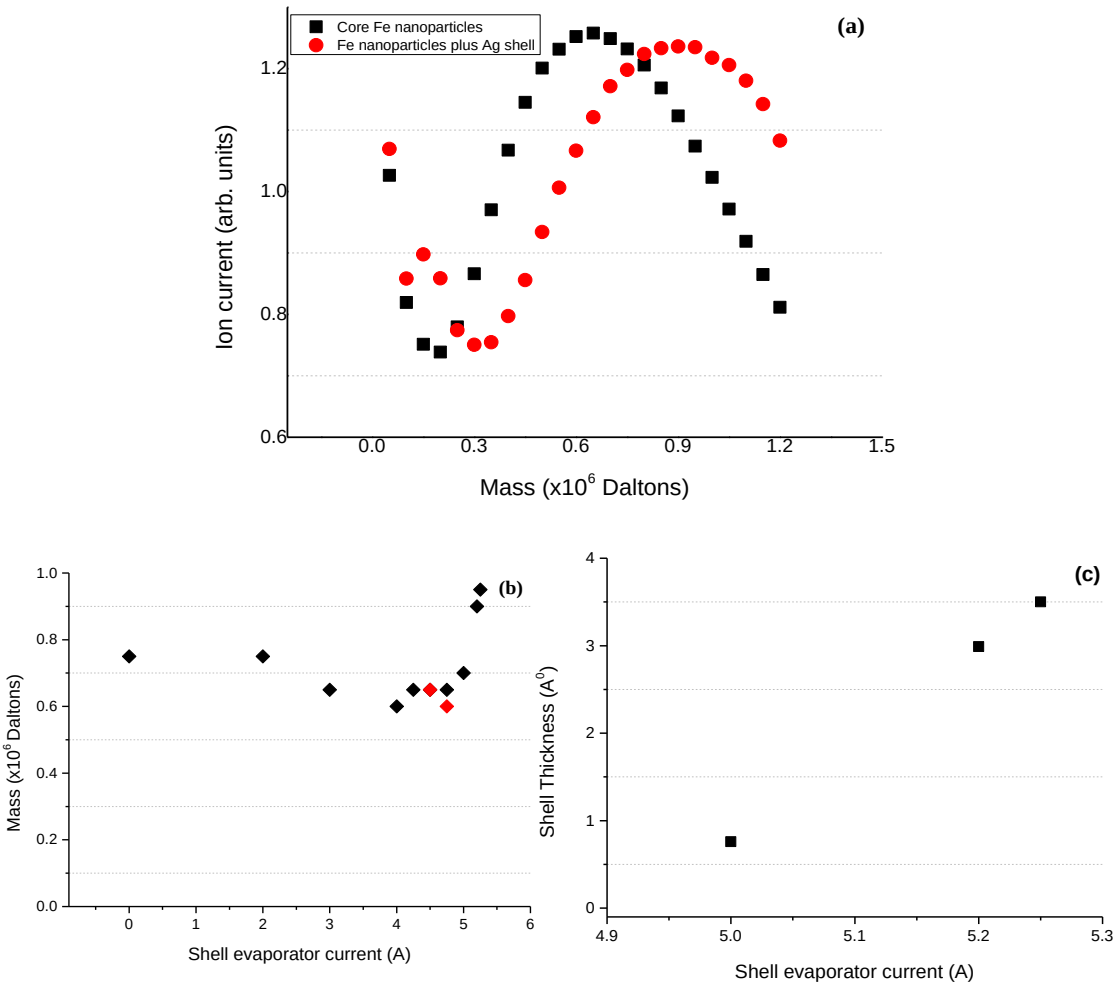

Figure 6.2: (a) Mass spectra of the core Fe and after coating with a Ag shell. (b) Mass of particles at different shell evaporator currents. (c) Shell thickness of Ag-coated Fe nanoparticles as a function of the shell evaporator current.

In figure 6.2 (a), the black squares display the mass spectrum of the core Fe particles when the shell evaporator is at 3.0 A, and the red circles represent the mass spectrum with the Ag shell evaporator current at 5.25 A. The uncoated Fe core nanoparticles have a most probable mass of 650,000 Daltons, which contains about 13,500 atoms with a diameter of 6.4 nm. When the particles pass through the hot evaporator, the mass has increased to 950,000 Daltons, that is, contain 4605 Ag atoms. Figure 6.2 (b) illustrates

the most probable mass of the particles as a function of the shell evaporator current. Up to 5.0 A, The most probable mass fluctuates so the uncoated material mass has been taken as the average of this fluctuation to calculate the shell thickness of the material. It is clear that the mass of the particles rapidly increases for shell evaporator currents above 5 A and reaches 950,000 Daltons. It returns to the same value when the current is reduced to 4.5 A.

The shell thickness of the material can be controlled by changing the temperature of the shell evaporator as shown in figure 6.2 (c). It is observed that while the shell thickness is 0.76 Å at 5.0 A, it has increased to 2.99 Å and 3.5 Å at 5.20 and 5.25 A, respectively.

In general it is clear that there is a significant shift in the mass of both Cu and Fe nanoparticles after passing through the hot Ag evaporator and the mass spectra demonstrate convincingly the pick-up of the shell material. However, the data does not prove that the shell is a uniform coating or whether it alloys with the core.

6.3 TEM Analyses of the Fe@Ag Core-Shell Nanoparticles

After observing the shell material by analysing the shift in the mass of nanoparticles in situ, it is worth determining how the core and shell material interact with each other. So TEM grids were placed in the deposition chamber, which is after the quadrupole mass filter. All the images presented here are from Fe nanoparticles that were deposited directly onto TEM grids, after passing through the shell evaporator at various currents in UHV conditions and transferred through air into the microscope. The high-resolution TEM images were obtained using the aberration-corrected JEOL 2200 FEG-TEM at the York-JEOL Nanocentre by Dr. Leonardo Lari in York.

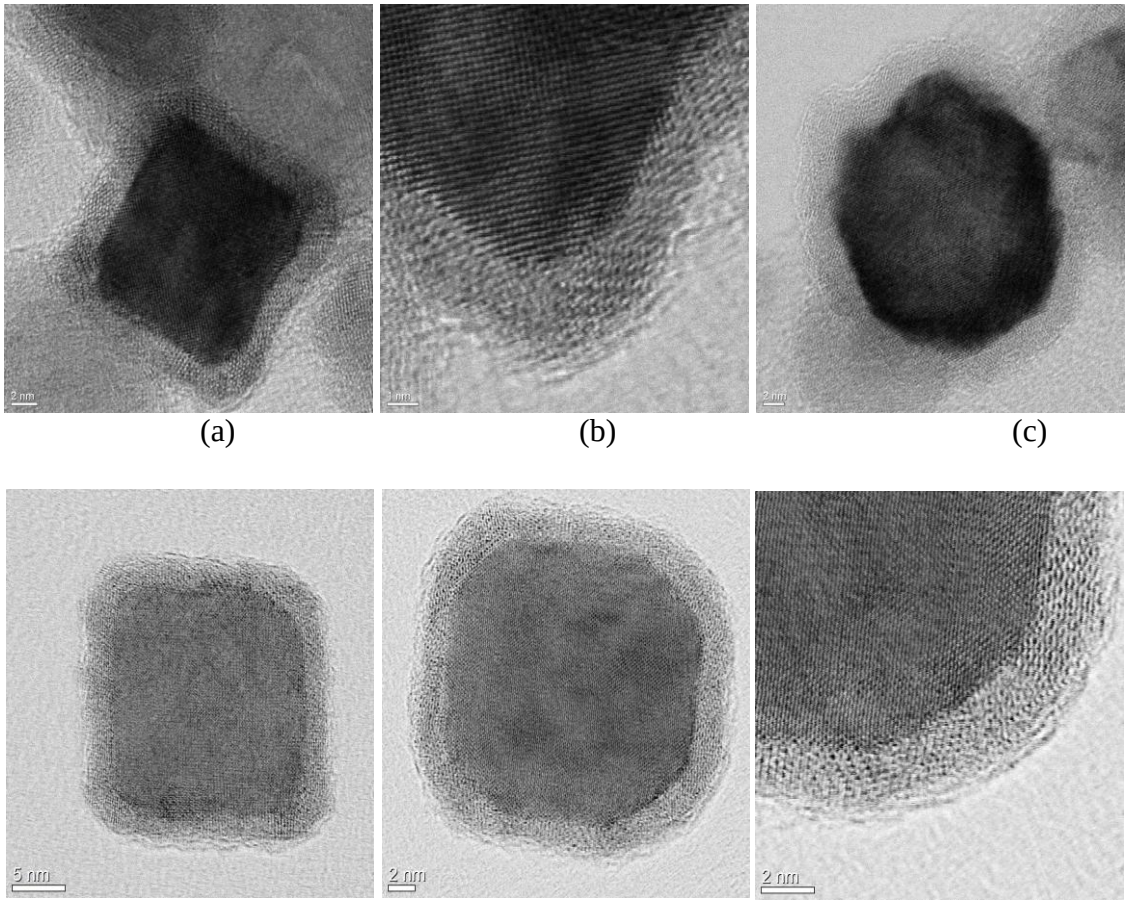

Figure 6.3: TEM images of the Fe nanoparticles directly deposited onto TEM grids after passing through the shell evaporator at different currents; (a), (b) and (c) at 2.0 A and (d), (e) and (f) at 2.5 A.

Figure 6.3 illustrates the TEM images of Fe@FeO nanoparticles passed through the shell evaporator, which was loaded with silver and deposited on TEM grids. The nanoparticles in figure 6.3 (a), (b) and (c) were produced while the shell evaporator current was 2.0 A, and in figure 6.3 (d), (e) and (f) was produced while the current was 2.5 A. At these low shell evaporator currents, which are much lower than the evaporation temperature of the shell material, no Ag is observed as expected. However, even at these low currents the particles are annealed (see below) so these are taken to be the starting state of the uncoated particles. The basic structure is a pure Fe core with a

thin oxide shell, which is similar to that observed with the shell evaporator off (see figure 4.1).

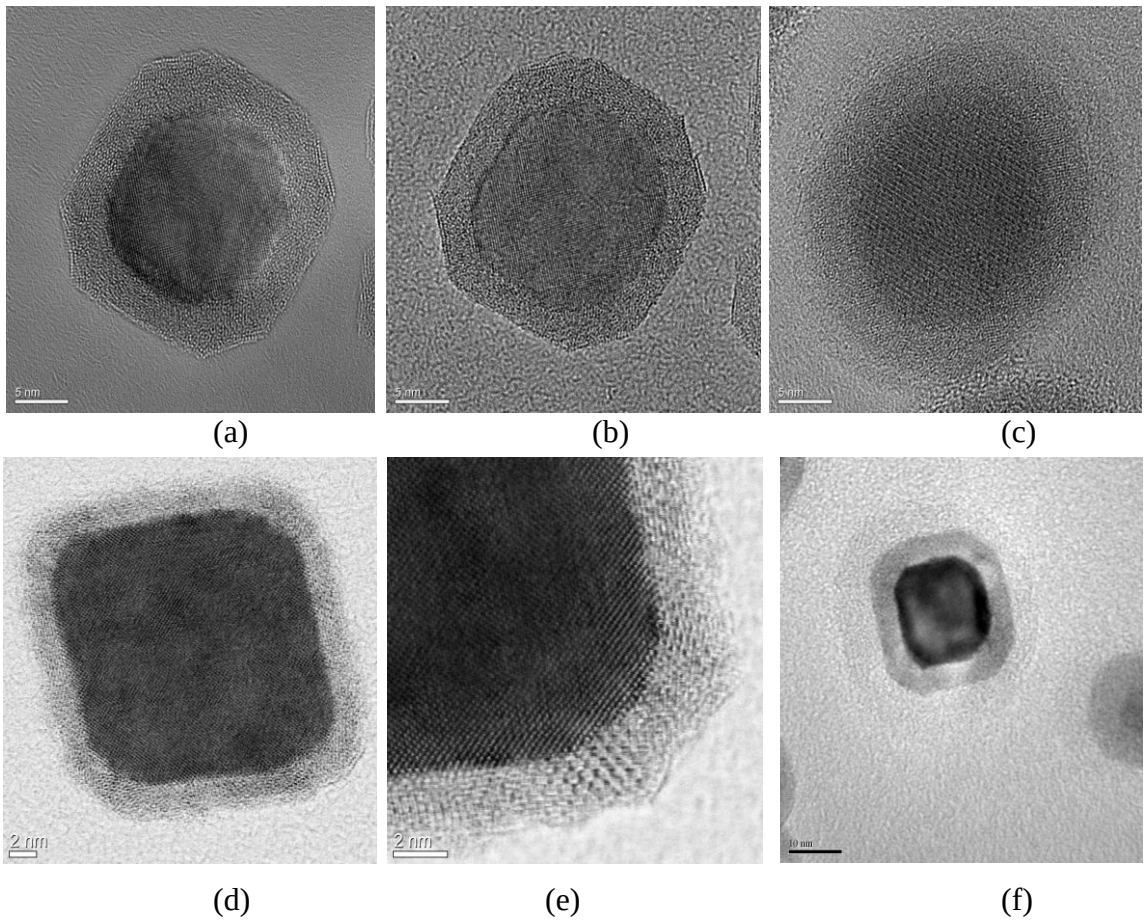

Figure 6.4: TEM images of the nanoparticles after passing through the heated crucible and directly deposited on to TEM grids. (a) and (b) deposited at 3.75 A, (c) deposited at 4.25 A, (d) and (e) deposited at 4.50 A, and (f) deposited on 5.0 A.

Figure 6.4 shows TEM images of the deposited nanoparticles after the shell evaporator current was increased from 3.75 to 5.0 A. Only Figure 6.4 (f) was taken using the JEOL 2100 TEM at the University of Leicester. None of the TEM images reveals a Ag shell around the nanoparticles. Even though a thin silver coating was observed at 5.0 A by the mass spectrum measurement in situ, TEM images taken up to 5.0 A do not show any silver shell. All the nanoparticles have a pure iron core and thin iron oxide shell and the only difference they have at different shell evaporator currents is their shapes, which

will be discussed in the next section. The next TEM samples were prepared with shell evaporator currents of 5.75 and 5.84 A.

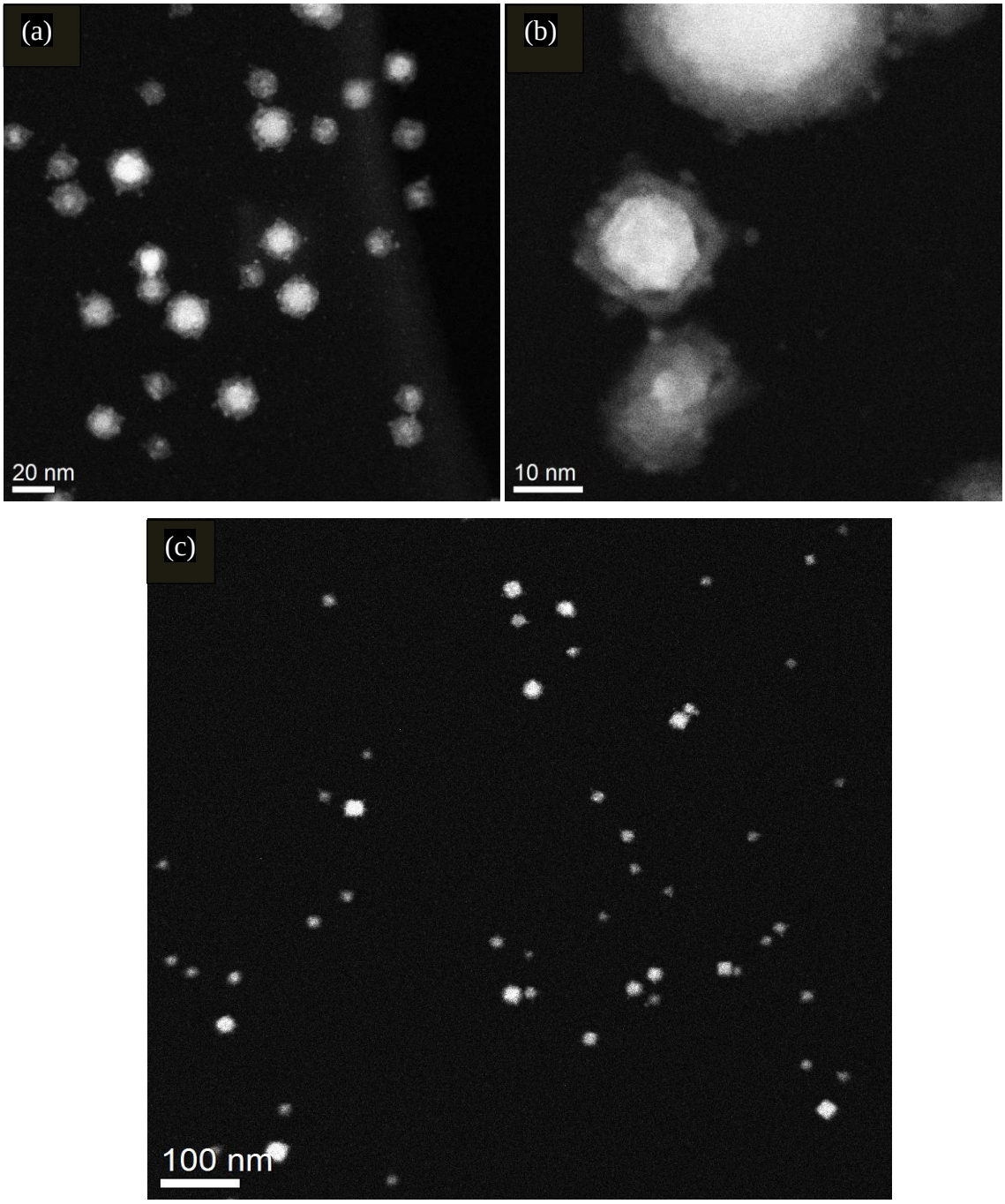

Figure 6.5: STEM images of the nanoparticles deposited in vacuum directly on TEM grids. (a) With a shell evaporator current of 5.75 A. (b) High magnification image at 5.75 A and (c) 5.84 A.

Figure 6.5 shows dark-field STEM images of the nanoparticles deposited in vacuum at 5.75 A, and 5.84 A shell evaporator current. It is clearly observed in figure 6.5 (a) and (b) that the nanoparticles have some small islands attached to their surface. Similarly, as for the other presented images, the nanoparticles have a pure iron core and an iron oxide shell as well.

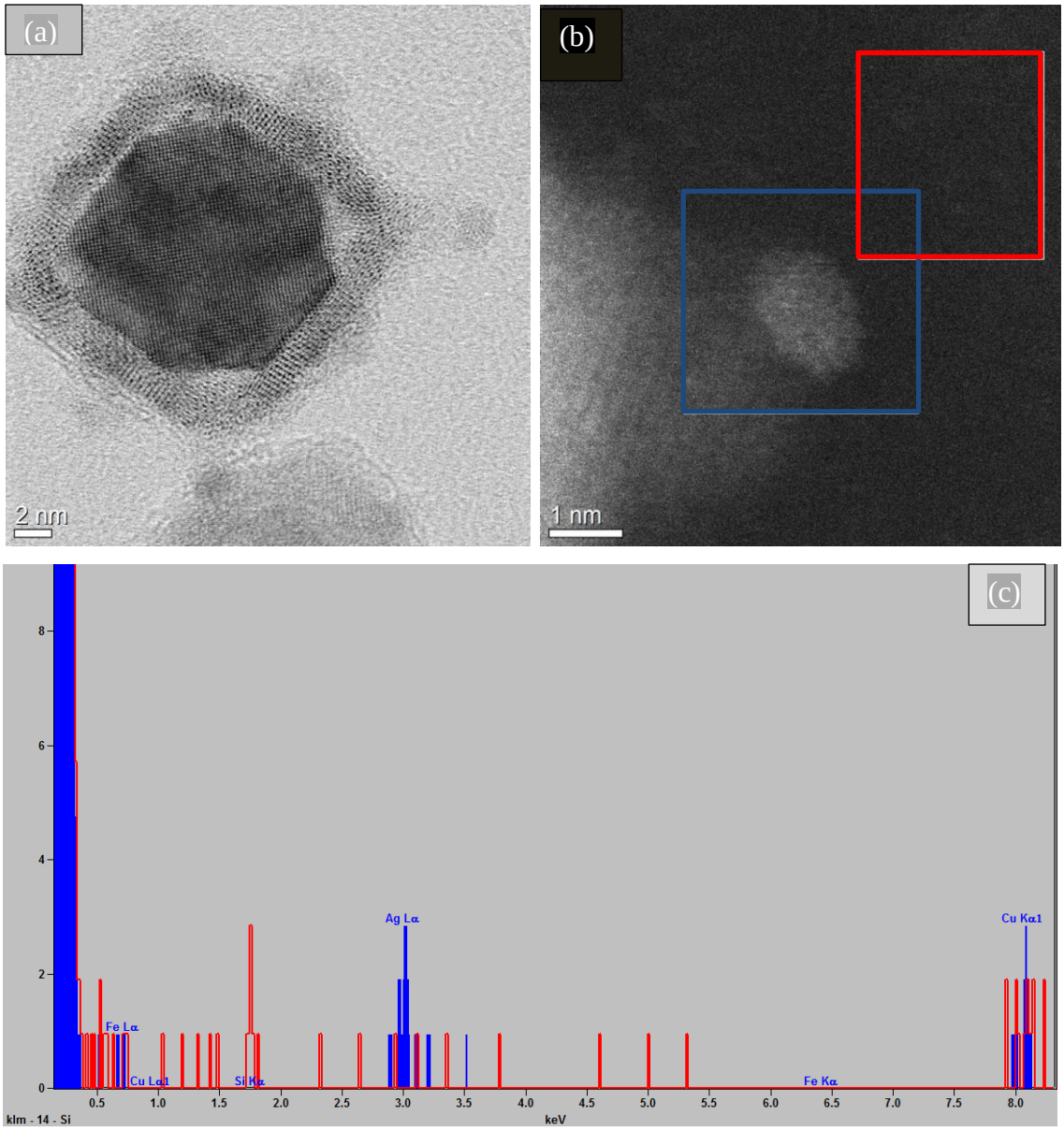

Figure 6.6: (a) Single nanoparticles produced while a 5.84 A shell evaporator current. (b) High magnification STEM images focused on a small island which attached to the surface of a nanoparticle. (c) EDX measurement of the areas shown by red and black squares in figure 6.6 (b).

As shown in figure 6.6 (c), energy-dispersive X-ray spectroscopy (EDX) measurements demonstrate that the small islands attached to the surface of the nanoparticles are Ag. Figure 6.6 (a) shows that the Ag has not uniformly coated the pure iron core and is attached to the nanoparticles' surface as small Ag islands. Hence nanoparticles form with a pure iron core uniformly coated with an iron oxide shell with some silver particles on their surface. This type of structure is called composite particles, which describes two different functional nanoparticles in intimate contact [Wang 2009].

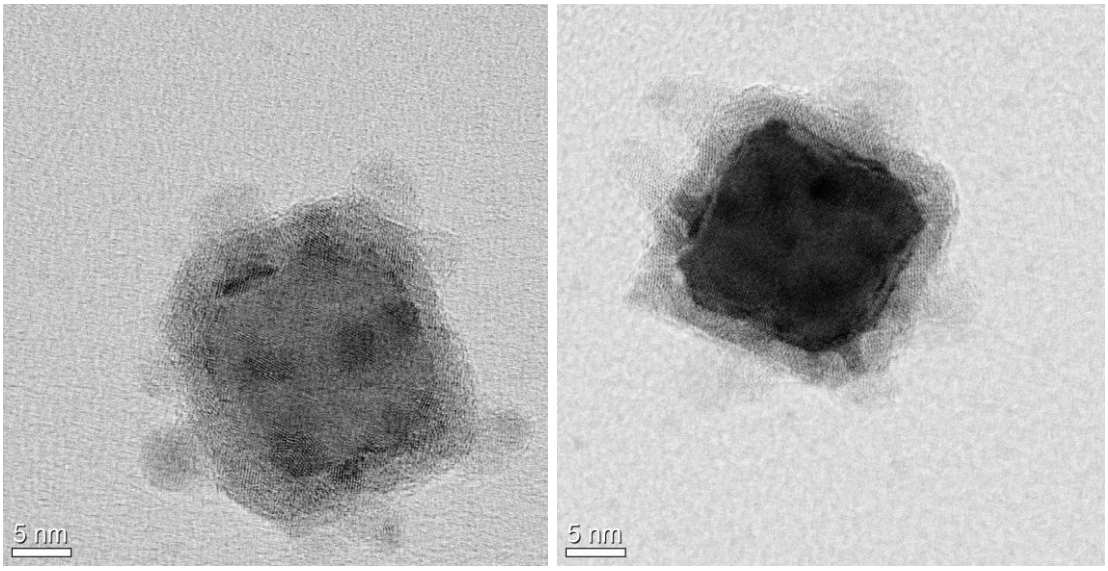

Figure 6.7: Examples of the composite Fe@FeO-Ag nanoparticles passed through the crucible at 5.75 A shell evaporator current.

Figure 6.7 shows two examples of composite Fe@FeO-Ag nanoparticles passed through the silver evaporator at 5.75 A. The same structure has been observed with 5.84 A. It is well known that Fe and Ag are immiscible in the solid state. Furthermore, due to the high surface energies of Fe and Ag nanoparticles [Xu 2008], Ag does not uniformly coat the iron surface and tends to form small particles on the surface.

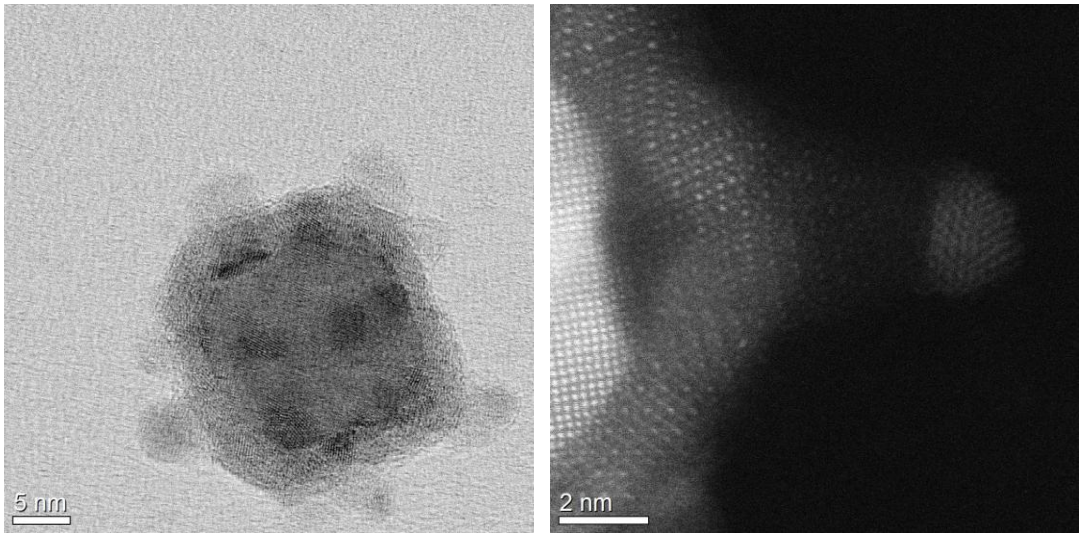

(a) (b)

Figure 6.8: (a) Fe@FeO-Ag composite nanoparticle (b) Details of the corner of a composite nanoparticle (presented in figure 6.6(a)), which shows the details of the contact surface between the Fe and Ag nanoparticles.

It has already been proven that in UHV conditions the nanoparticles have only a pure iron core. The oxide shell occurs as soon as the particles are in contact with air. As shown in figure 6.8 (a), small silver islands are attached to the surface of the nanoparticles. Due to not uniformly coating the highly active Fe nanoparticle surface, the particles oxidise when they are exposed to air. As a result of the further oxidation process, a thin oxide shell uniformly coats the iron surface and lifts the silver nanoparticle away from the iron surface to the iron oxide surface as illustrated in figure 6.8 (b). Hence the final structure of nanoparticles determined from TEM images is composite with small Ag nanoparticles attached to a thin oxide shell around the Fe core.

Overall, the synthesis of Fe nanoparticles with a Ag shell has not worked as expected. However, Fe@FeO-Ag composite nanoparticles have been produced and these are promising for biomedical application as multifunctional probes for target-specific imaging and delivery application with binding at specific receptors [Wang 2009].

6.4 Control of the Shape of the Nanoparticles

The magnetic properties of nanoparticles are highly dependent on their size and shape. Gas phase synthesis of iron nanoparticles in UHV conditions lead to a narrow size distribution and either superparamagnetic or ferromagnetic nanoparticles can be produced as shown in chapter 4, section 4. Furthermore, it is observed that mostly cubic and spherical nanoparticles are present under normal deposition conditions.

During the attempt to produce core shell nanoparticles by passing them through the hot crucible, it was observed that different shape nanoparticles can be produced. Hence to clarify the shape changes as a function of temperature and understanding its effect on magnetic properties, three sets of TEM and liquid samples were produced.

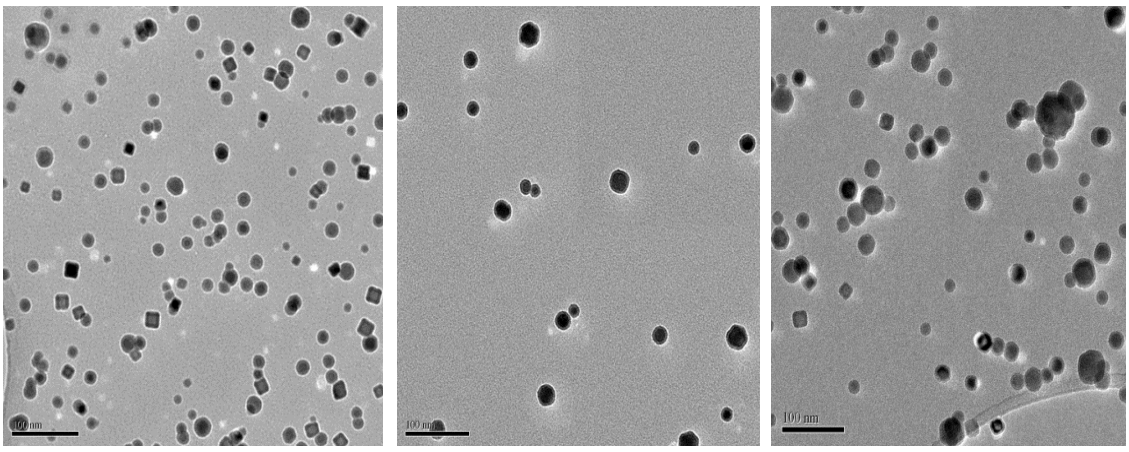

(a) (b) (c)

Figure 6.9: TEM images taken with the JEOL 2100 TEM at the University of Leicester for samples produced with the shell evaporator current (a) off, (b) 5.0 A and (c) 5.25 A.

TEM grids were placed in the deposition chamber and nanoparticles passed through the crucible, containing no shell material while the shell evaporator current was 0, 5.0 and 5.25 A to prepare three sets of samples as shown in figure 6.9 (a), (b) and (c), respectively. All TEM samples were synthesised with the same vacuum conditions and sputtering power. As usual, the natural oxidation process leads to a thin oxide shell

when transferring in air from the nanoparticle source to the microscope. The shape analyses of the unheated and heated nanoparticles have been carried out on the TEM images using Adobe Photoshop CS6 software.

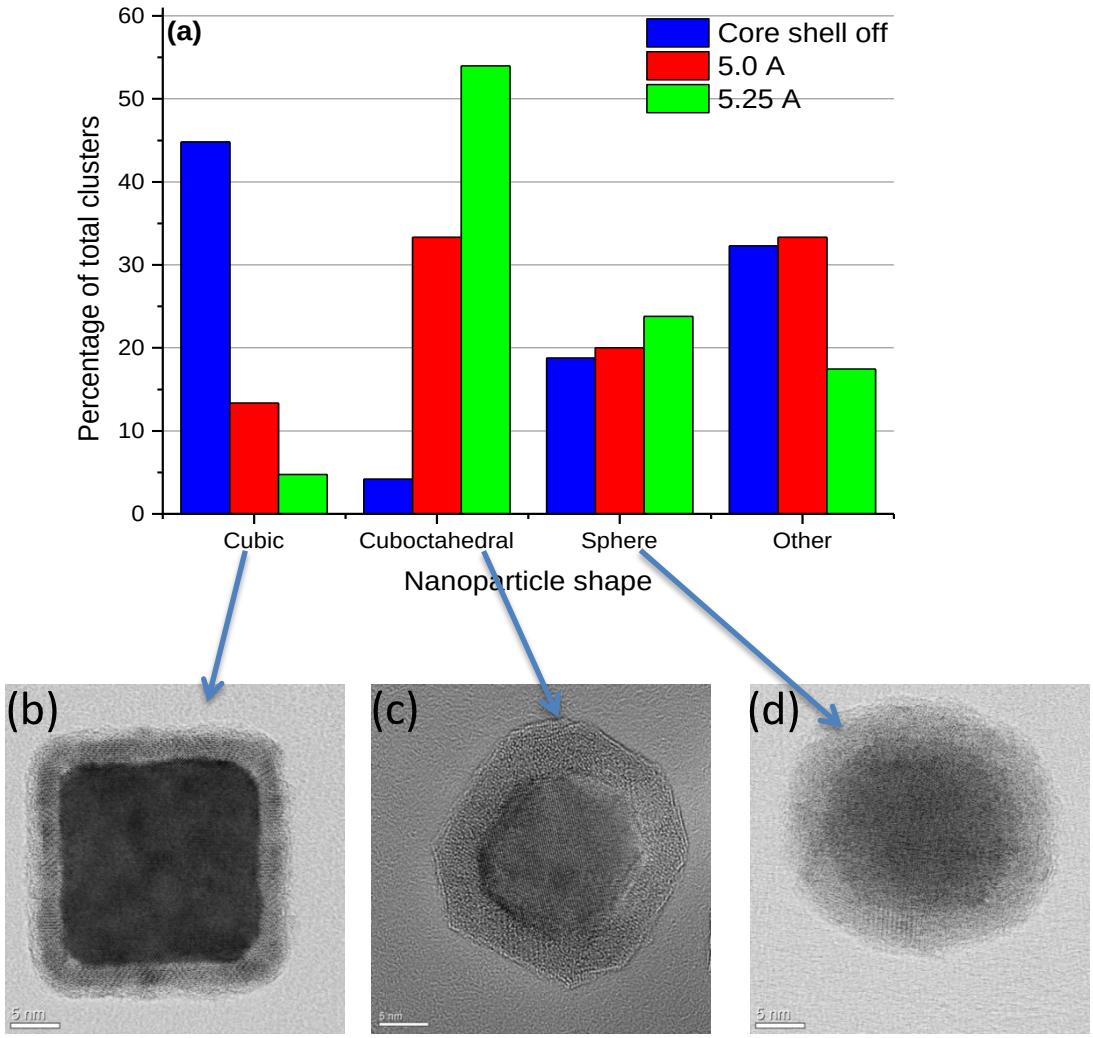

Figure 6.10: (a) Nanoparticle shapes as a function of the shell evaporator current which has been used to anneal the free nanoparticles. (b), (c) and (d) Cubic, cuboctahedral and spherical shapes observed by TEM after depositing the nanoparticles in vacuum.

A detailed shape analysis of the nanoparticles produced in vacuum at different annealing temperatures is illustrated in figure 6.10 (a). As already mentioned in the previous section, due to the technical problem of measuring the shell evaporator

temperature, shape changes have been illustrated as a function of the shell evaporator current instead of temperature. Both the unheated and heated nanoparticle beam consists of a mixture of shapes which has been determined by observing nanoparticle TEM images taken by the aberration corrected JEOL 2200 FEG-TEM, including cubes (figure 6.10 (b)), cuboctahedra (figure 6.10 (c)), spheres (figure 6.10 (d)) and more complex shapes. The cuboctahedral-shaped nanoparticles show either hexagonal or octagonal shapes in the two-dimensional TEM images depending on which facet is in contact with the surface.

The number of cubic nanoparticles is dominant in unheated nanoparticles and it decreases with the annealing temperature. It is clearly demonstrated in figure 6.10 (a) that the annealing of the nanoparticles converts a large proportion of the cubes to cuboctahedra. Furthermore, at the highest temperature, the proportion of the other shapes drops to its lowest value. However, the proportion of the spherical particles does not change significantly.

To determine the influence of the shape changes (mostly from cubic to cuboctahedral) on the magnetic properties of the nanoparticles, three liquid samples were produced at three different shell evaporator currents under UHV conditions with the sputter gas aggregation source (see chapter 2, section 1.4 – figure 2.8).

To determine how the annealed and un-annealed nanoparticle suspensions would perform as contrast agents in MRI diagnosis, samples have been analysed by the MRI unit at the Leicester Royal Infirmary. Their longitudinal ($R_1 = 1\ T_1$) and transverse ($R_2 = 1\ T_2$) relaxation rates have been measured as a function of concentration for three Fe@FeO samples. One of them was not annealed and two were annealed at 5.0 and 5.25 A shell evaporator currents.

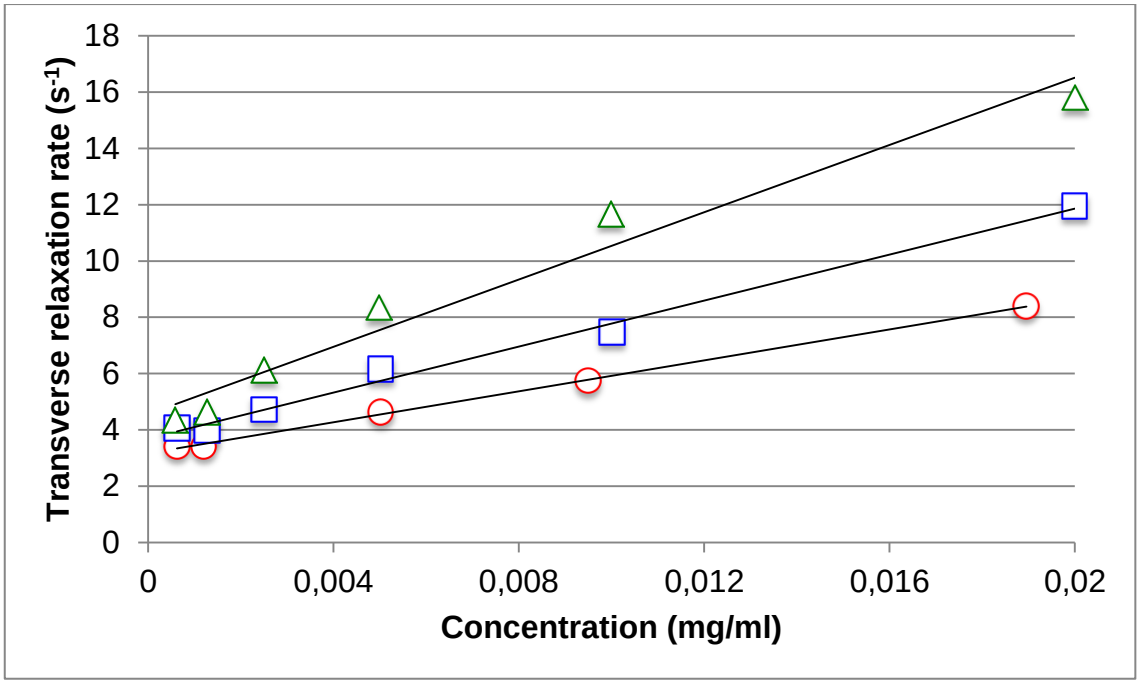

Figure 6.11: Transverse relaxation rate versus concentration for Fe@FeO nanoparticles synthesised with the shell evaporator off (triangles), at 5.0 A (squares) and at 5.25 A (circles).

The concentration dependence of the longitudinal relaxation was negligible, which is typical for dispersed nanoparticles, but the effect of the concentration on transverse relaxation rate was clear as shown in figure 6.11. It is evident that the response of the nanoparticles significantly decreases with annealing. The un-annealed sample, in which cubes are much more common (see figure 6.10 (a)) shows the highest response. Furthermore, with annealing nanoparticles at 5.0 and 5.25 A, converting the cubes to cuboctahedral, the traverse relaxations display a significantly lower response than the un-annealed sample. This proves that the shape of the nanoparticles has a significant influence on the magnetic properties of the material. Also, the general finding revealed in figure 6.10 (a) and 6.11 is that cubic nanoparticles have a higher magnetic moment than the cuboctahedral nanoparticles.

According to the Kolhatkar (2013), the saturation magnetisation of cubic nanoparticles is higher than that of spherical nanoparticles of the same volume [Zhen 2011], and to

explain this Noh (2012) simulated the orientation of the magnetic spin structures in both a cube and a sphere of the same volume and found that the ratio of disordered spins in cubic nanoparticles (4%) is smaller than that in spherical (8%) nanoparticles. The drop observed in the R_2 relaxivity is higher than this which could be due to a disproportional influence of surface spins on MRI response.

The calculated transverse relaxivity value of the unheated Fe@FeO nanoparticles from the slope of the curve in figure 6.11 after doing the necessary conversions from mg/ml to mM is approximately 35 $\mathrm{mM^{-1}s^{-1}}$. This value is about half that of commercially used iron oxide nanoparticles value (~ 78 $\mathrm{mM^{-1}s^{-1}}$). However, the relaxation value of the nanoparticles highly depends on the concentration of suspension. The total amount of magnetic material deposited in the ice layer has been calculated (see chapter 2 section 1.4.1) as 0.1 mg/ml but this is not necessarily the same as the final concentration in the collected liquid. To get a rough estimate of the concentration, the liquid was removed from the 5 ml sample by collecting all the nanoparticles to one side with a magnet. The final part was left to evaporate and dry with the magnet in place leaving finally a small quantity of dry powder. The attempt to weigh the powder was not successful even with the most sensitive scale which has a sensitivity of 0.1 mg. The total amount of powder from the calculation should have been 0.5 mg and easily measurable. Thus, the final limit of concentration has been estimated to have an upper limit of 0.02 mg/ml and the MRI relaxivity has been calculated using this concentration. So the MRI performance of the nanoparticles refers to the lower limits and is probably much higher than the calculated value.

6.5 Conclusion

In UHV conditions, with the gas aggregation source it is possible to produce core-shell multifunctional nanoparticles by passing them through a loaded shell evaporator. In situ mass spectrum analyses have demonstrated that at the vapour pressure of the shell material in the tubular crucible, it is possible to pick up shell material. TEM images of the nanoparticles deposited in UHV conditions at the different shell evaporator currents up to 5.0 A illustrate that there is not any silver coating and nanoparticles form the same as before with an iron core and a thin oxide shell. Furthermore, at the highest shell evaporator currents, TEM images of the nanoparticles show that silver forms as small particles on the iron surface and after oxidation, are lifted onto the oxide surface. The final form of the nanoparticles is composite Fe@FeO-Ag which will have multifunctional properties for diagnosis and treatment in medical applications. In general, the results show that this technique works best when the vapour pressure of the core material is significantly lower than the vapour pressure of the shell material at the temperature of the shell evaporator.

Also the deposition of various shapes of the nanoparticles following annealing under UHV condition, which enables some control over the magnetic properties of the particles, has been demonstrated. The MRI response of the different shapes of the nanoparticles shows that cubic nanoparticles are the best candidate for hyperthermia treatment and MRI diagnosis due to their higher magnetisation. Also at the lower limit, the transverse relaxivity value has been estimated to be 35 $\mathrm{mM^{-1}s^{-1}}$ but is likely to be significantly higher.

Chapter 7

Conclusion and Future Work

7.1 Conclusion

The size distribution and shape of the gas phase produced Fe nanoparticles deposited directly onto Transmission Electron Microscopy (TEM) grids and into liquid were analysed by TEM. The size distribution of nanoparticles deposited into water was determined using a Brownian motion analyser (Nanosight LM10). The nanoparticles deposited directly onto TEM grids have a thin oxide shell around the pure iron core due to sample transfer through air. Also, oxidation of the nanoparticles in liquid suspensions shows similarities with the directly-deposited nanoparticles onto TEM grids. Additionally, the size distribution of the nanoparticles can be controlled by changing the temperature of the gas by turning the water cooling to the sputter head on and off. That means that while the water cooling is on, the most probable particle size is ~ 16 nm (mostly blocked), on the other hand it is about 8.55 nm (superparamagnetic) when the water cooling is off. Changing the position of the LN_2 tank enables the deposition of denser samples.

The best results for stabilisation of the nanoparticles in suspension by adding various surfactants were obtained using DMSA and sorbitol. The nanoparticles without any chemical coating are hydrophobic and so DMSA or sorbitol-coated iron nanoparticles have a small size and stabilise in water for a long time. However, DMSA-coated nanoparticles transform into a non-magnetic oxide although they have distinct UV-visible spectra in the first few days. According to the magnetic measurements of sorbitol-coated nanoparticles, due to an incomplete coating of the highly-reactive iron

surface, oxidation erodes the pure iron core to about 5 nm in two months. On the other hand, MRI measurements of the sorbitol-coated iron nanoparticles, which were done one month after synthesis, show promising result for use as MRI contrast agents.

Hence commonly used surfactants for iron oxide do not prevent the agglomeration between iron nanoparticles since the separation distance between two iron nanoparticles should be four times bigger than two iron oxide nanoparticles. Also, long-chain molecules did not work since nanoparticles agglomerate faster than the coating molecules can cover the surface. Sorbitol, which is a short chain molecule, prevents the particles agglomeration but does not stop the oxidation due to not uniformly coating the surface.

According to the magnetic measurements, the anisotropy constant of the sorbitol-coated iron nanoparticles is close to the anisotropy constant of bulk iron so they can produce more heat for hyperthermia treatment. However, the concentration of the solution was found to be much less than the calculated one. Hence, SAR measurement of the nanoparticles produced by the gas aggregation source is impossible with the heating coils used in the project according to a calibration using a commercial ferrofluid.

Modelled SAR values of iron nanoparticles show that the nanoparticles should have a narrow size distribution with the most probable diameter in the 12-16 nm range to generate a higher heating for effective hyperthermia. Additionally, the contribution of the hysteresis heating on total power is much higher than susceptibility heating. Thus for an effective nanoparticle hyperthermia, the magnetic nanoparticles should be blocked with a low anisotropy constant and a high saturation magnetisation. Also, the calculated SAR of the sorbitol-coated Fe@FeO nanoparticles with a diameter of 16 nm

at the Atkinson-Brezovich limit is five times higher than Fe oxide nanoparticles and also with a safe alternating magnetic field for brain tumours it is possible to obtain SAR values up to 600 W/g. This leads to lower particle concentrations required to be injected into tumour tissue.

Gas-phase produced biocompatible pure iron core nanoparticles effectively dispersed in a liquid suspension with a narrow size distribution may introduce hyperthermia treatment as an effective cancer treatment technique without any negative side effects. Also they show promising results as a contrast agent for MRI.

The attempt to produce Fe@Ag core shell nanoparticles showed that there is not any silver shell around the pure iron at shell evaporator currents up to 5.0 A. What's more, at the highest shell evaporator temperature, silver forms as small particles on the iron surface rather than a uniformly coated shell. This type of structure is called a composite particle and presents both Fe@FeO and Ag at the surface which can be used as multifunctional medical nanoparticles.

It is demonstrated that shape control of the nanoparticles is possible by passing the nanoparticles through a heated tubular crucible. The majority of the cubic nanoparticles form cuboctohedra at higher crucible temperatures and these show a reduced MRI relaxivity. According to the MRI response of the different shape of the nanoparticles, cubic nanoparticles are the best candidate for hyperthermia treatment and MRI diagnosis due to their highest magnetisation.

7.2 Future Work

The MRI response and calculated SAR values of the sorbitol-coated pure iron core nanoparticles with an iron oxide shell produced by the gas aggregation technique under

UHV conditions show promising results for future medical application. In the future, attempts should focus on the production of core-shell nanoparticles to overcome the oxidation of the pure iron core by coating with a uniform metal shell such as Al or Mg under UHV conditions. Also further research should be carried out for the stabilisation of the nanoparticles in liquid suspension by attaching the ligands to the nanoparticles before they agglomerate. Mainly short chain molecules, which have higher diffusion coefficient should be employed to prevent the agglomeration and additionally, by varying the pH of the solution, the zeta potential can be increased to prevent agglomeration.

Additionally, magnetic nanoparticles could be coated by surfactants before they land in the ice matrix. Since for many surfactants the magnetic nanoparticles diffuse faster than the ligands, they tend to agglomerate before the coating is complete. To do this, suitable ligands could be placed into a shell evaporator to generate a high vapour pressure of the coating material in the path of the free beam of nanoparticles.

An alternative to depositing the nanoparticles into water is to deposit them in UHV conditions into a solid insulating matrix and record temperature changes in response to an alternating magnetic field with a thermal camera. This would enable the nanoparticle properties to be optimised prior to solving the problem of obtaining stable hydrosols.

Furthermore, composite Fe@FeO-Ag nanoparticles should be investigated further for multifunctional biomedical applications, for example particles that can be heated both magnetically and optically via the surface plasmon resonance of Ag. Hence, the next step would be production of these nanoparticles in a liquid suspension.

List of Publications

"Preparation of Hydrosol Suspensions of Elemental and Core-Shell Nanoparticles by Co-Deposition with Water Vapour from the Gas-Phase in Ultra-High Vacuum Conditions"

C. Binns, P. Prieto, S. Baker, P. Howes, R. Dondi, G. Burley, L. Lari, R. Kröger, A. Pratt, S. Aktas and J. K. Mellon, J. Nanoparticle Res. **14** (2012) 1136.

"Controlling the Shape of Gas Phase Nanoparticles and Shape Effect on MRI"

S Aktas, S C Thornton, C Binns, A Pratt, R Kröger, L Lari and M Horsfield (Submitted to Nanoscale).

"Gas-Phase Synthesis of Core-Shell Magnetic Nanoparticles into fluids"

S C Thornton, S Aktas and C Binns (Preparation for J. Phys. D: Appl. Phys.).

References

Amendola V, Bakr O M, Stellacci F (2010) Plasmonic **5**:85-97

Arsalani N, Fattahi H, Nazarpoor M (2010) eXPRESS Polymer Letters **4**:329–338

Atkinson W J, Brezovich I A, Chakraborty D P (1984) IEEE (T) Biomedical Engineering **BME-31**:70-75

Baker SH, Thornton SC, Edmonds KW, Maher MJ, Norris C, Binns C (2000) Rev. Sci. Instr. **71**:3178

Bakoglidis K D, Simeonidis K, Sakellari D, Stefanou G, Angelakeris M (2012) IEEE Transactions on Magnetics **48**:1320-1323

Banerjee A N, Krishna R, Das B (2008) Appl. Phys. A **90**:299–303

Berry C C, Wells S, Charles S, Curtis A S G (2003) Biomaterials **24**:4551–4557

Billotey C, Wilhelm C, Devaud M, Bacri J C, Bittoun J, Gazeau F (2003) Magnetic Resonance in Medicine **49**:646–654

Binns C, Maher M J (2002 a) New Journal of Physics **4**:85.1-85.15

Binns C, Maher M J, Pankhurst Q A, Kechrakos D, Trohidou K N (2002 b) Phys. Rev. B **66**:184413

Binns C, Trohidou K N, Bansmann J, Baker S H, Blackman J A, Bucher J-P, Kechrakos D, Kleibert A, Louch S, Meiwes –Broer K-H, Pastor G M, Perez A, Xie Y (2005) J. Phys. D:Appl. Phys. **38**:R357-R379

Binns C (2010) Magic Beacons and Magic Bullets: The Medical Applications of Functional Nanoparticles. Chapter 6 in *Introduction to Nanoscience and Nanotechnology* Wiley

Binns C, Prieto P, Baker S, Howes P, Dondi R, Burley G, Lari L, Kröger R, Pratt A, Aktas S, Mellon J K (2012) J. Nanopart. Res. **14**:1136

Binns C (2014 a) Tutorial Section on Nanomagnetism. Chapter 1 in *Nanomagnetism: Fundamentals and Applications* Elsevier

Binns C (2014 b) Medical Applications of Magnetic Nanoparticles. Chapter 6 in *Nanomagnetism: Fundamentals and Applications* Elsevier

Bönnemann H, Brijoux W, Brinkmann R, Matoussevitch N, Waldöfner N, Palina N, Modrow H (2003) Inorg. Chim. Acta. **350**:617 – 624

Caligur V (2008) Detergent Properties and Applications. BioFiles **3.3**-14

Chaudhuri R G, Paria S (2012) Chem. Rev. **112**:2373–2433

Chaughule R S, Purushotham S, Ramanujan R V (2012) Proc. Natl. Acad. Sci., India, Sect. A Phys. Sci. **82**:257–268

Chung R-J, Shih H-T (2014) Materials **7**:653-661

Datta S, Kabir M, Saha-Dasgupta T (2011) Physical Review B **84**: 075429

Davies P (2013) Physics World **26**:37 – 40

DeNardo G L, DeNardo S J (2008) Cancer Biother. Radiopharm. **23**:671-679

Derjaguin B, Landau L (1941) Acta Physico Chemica URSS **14**:633-662

Dobson J (2006) Drug Dev. Res. **67**:55-60

Easo S L, Mohanan P V (2013) Carbohydrate Polymers **92**:726– 732

Eastman J (2010) Stability of charge-stabilised colloids. Chapter 3 in *Colloid Science: Principles, Methods and Applications* Wiley

El-Brolossy T A, Abdallah T, Mohamed M B,Abdallah S, Easawi K, Negm S, Talaat H (2008) Eur. Phys. J. Special Topics **153**:361–364

Fauconnier N, Pons J N, Roger J, Bee A (1997) Journal of Colloidal and Interface Science **194**:427–433

Faure B, Salazar-Alvarez G, Bergström L (2011) Langmuir **27**:8659-8664

Fortin J -P, Wilhelm C, Servais J, Ménager C, Bacri J-C, Gazeau F (2007) J. Am. Chem. Soc. **129**:2628–2635

Gamarra L F, Brito G E S, Pontuschka W M, Amaro E, Parma A H C, Goya G F (2005) J. Magn. Magn. Mater. **289**:439–441

Gilchrist R K, Medal R, Shorey W D, Hanselman R C, Parrott J C, Taylor C B (1957) Ann. Surgery **146**:596-606

Graf C, Vossen D L J, Imhof A, Blaaderen A van (2003) Langmuir **19**:6693-6700

Guo L, Huang Q, Li X-Y, Yang S (2001) Phys. Chem. Chem. Phys. **3**:1661-1665

Haberland H, Karrais M, Mall M, Thurner Y (1992) J. Vac. Sci. Technol. A **10**:3266-3271

Haeften K. von, Binns C, Brewer A, Crisan O, Howes P B, Lowe M P, Sibbley-Allen

C, Thornton S C (2009) Eur. Phys. J. D **52**:11-14

Hergt R, Hiergeist R, Zeisberger M, Schüler D, Heyen U, Hilger I, Kaiser W A (2005) J. Magn. Magn. Mater. **293**:80-86

Hergt R, Dutz S, Müller R and Zeisberger M (2006) J. Phys.: Condens. Matter **18**:S2919–S2934

Hergt R, Dutz S, Röder M (2008) J. Phys.: Condens. Matter **20**:385214

Hergt R, Dutz S, Zeisberger M (2010) Nanotechnology **21**:015706

Hong R Y, Feng B, Chen L L, Liu G H, Li H Z, Zheng Y, Wei D G (2008) Biochemical Engineering Journal **42**:290–300

Jackson T J, Binns C, Forgan E M, Morenzoni E, Niedermayer C, Glückler H, Hofer A, Luetkens H, Prokscha T, Riseman T M, Schatz A, Birke M, Litterst J, Schatz G, Weber H P (2000) J. Phys.: Condens. Matter **12**:1399–1411

Johannsen M, Thiesen B, Wust P, Jordan A (2010) Int. J. Hyperthermia **26**:790-795

Jordan A, Wust P, Fählin H, John W, Hinz A and Felix R (1993) Int. J. Hyperthermia **9**:51-68

Jun Y-W, Huh Y-M, Choi J-S, Lee J-H, Song H-T, Kim S, Yoon S, Kim K-S, Shin J-S, Suh J-S, Cheon J (2005) J. Am. Chem. Soc. **127**:5732-5733

Kallumadil M, Tada M, Nakagawa T, Abe M, Southern P, Pankhurst Q A (2009) J. Magn. Magn. Mater. **321**:1509–1513

Kita E, Oda T, Kayano T, Sato S, Minagawa M, Yanagihara H, Kishimoto M, Mitsumata C, Hashimoto S, Yamada K, Ohkohchi N (2010) J. Phys. D: Appl. Phys. **43**:474011

Kohler N, Fryxell G E, Zhang M (2004) J. Am. Chem. Soc. **126**:7206-7211

Kolhatkar A G, Jamison A C, Litvinov D, Willson R C, Lee T R (2013) Int. J. Mol. Sci. **14**:15977-16009

Kouchi A (1987) Nature **330**:550

Laurent S, Nicotra C, Gossuin Y, Roch A, Ouakssim A, Elst L V, Cornant M, Soleil P, Muller R N (2004) Phys. Stat. Sol. (c) **1**:3644-3650

Lee J-H, Huh Y-M, Jun Y-W, Seo J-W, Jang J-T, Song H-T, Kim S, Cho E-J, Yoon H-G, Suh J-S, Cheon J (2007) Nat. Med. **13**:95 – 99

Lee J-H, Jang J-T, Choi J-S, Moon S H, Noh S-H, Kim J-W, Kim J-G, Kim I-S, Park K I, Cheon J (2011) Nat. Nanotech. **6**:418–422

Leng Y, Sato K, Li J-G, Ishigaki T, Iijima M, Kamiya H, Yoshida T (2009) Powder Technology **196**:80–84

Li L, Jiang W, Luo K, Song H, Lan F, Wu Y, Gu Z (2013) Theranostics **3**:595-615

Liu H-L, Ko S B, Wu J-H, Jung M-H, Min J H, Lee J H, An B H, Kim Y K (2007) J. Magn. Magn. Mater. **310**:e815–e817

Lok C (2001) Nature **412**:372-374

Lu L, Zhang W, Wang D, Xu X, Miao J, Jiang Y (2010) Materials Letters **64**:1732–1734

Lu X, Niu M, Qiao R, Gao M (2008) J. Phys. Chem. B **112**:14390–14394

Maier-Hauff K, Rothe R, Scholz R, Gneveckow U, Wust P, Thiesen B, Feussner A, Deimling A von, Waldoefner N, Felix R, Jordan A (2007) J. Neurooncol. **81**:53–60

Maier-Hauff K, Ulrich F, Nestler D, Niehoff H, Wust P, Thiesen B, Orawa H, Budach V, Jordan A (2011) J. Neurooncol. **103**:317–324

Mehdaoui B, Meffre A, Lacrroic L-M,Carrey J, Lachaize S, Gougeon M, Respaud M, Chaudret B (2010) J. Magn. Magn. Mater. **322**:L49-L52

Nielsen O S, Horsman M, Overgaard J (2001) European Journal of Cancer **37**:1587-1589

Noh S-H, Na W, Jang J-T, Lee J-H, Lee E J, Moon S H, Lim Y, Shin J-S, Cheon J (2012) Nano Lett. **12**:3716–3721

O'Grady K, Bradbury A (1983) J. Magn. Magn. Mater **39**:91-94

Orendorff C J, Sau T K, Murphy C J (2006) Small **2**:636 – 639

Pankhurst Q A, Connolly J, Jones S K, Dobson J (2003) J. Phys. D: Appl. Phys. **36**:R167–R181

Pankhurst Q A, Thanh N T K, Jones S K, Dobson J (2009) J. Phys. D: Appl. Phys. **42**:224001

Parkes L M, Hodgson R, Tu L T, Tung L D, Robinson I, Fernig D G, Thanh N T K (2008) Contr. Med. Mol. Imag. **3**:150–156

Pratt A, Lari L, Hovorka O, Shah A, Woffinden C, Tear S P, Binns C, Kröger R (2014) Nat. Mater. **13**:26-30

Purushotham S, Ramanujan R V (2010) J. Appl. Phys. **107**:114701

Reimer P, Balzer T (2003) Eur. Radiol. **13**:1266 – 1276

Rosensweig R E (2002) J. Magn. Magn. Mater. **252**:370-374

Roussakow S (2013) Hindawi Publishing Corporation Conference Paper in Medicine Article ID 428027.

Rümenapp C, Gleich B, Haase A (2012) Pharm. Res. **29**:1165-1179

Salunkhe A B, Khot V M, Pawar S H (2014) Current Topics in Medical Chemistry **14**:1-23

Seo W S, Lee J H, Sun X, Suzuki Y, Mann D, Liu Z, Terashima M, Yang P C, McConnell M V, Nishimura D G, Dai H (2006) Nat. Mater. **5**:971 – 976

Shultz M D, Calvin S, Fatouros P P, Morrison S A, Carpenter E E (2007) J. Magn. Magn. Mater. **311**:464-468

Sun Q, Kandalam A K, Wang Q, Jena P, Kawazoe Y,Marquez M (2006) Physical Review B **73**:134409

Tong S, Hou S, Zheng Z, Zhou J, Bao G (2010) Nano Lett. **10**: 4607–4613

Vallejo-Fernandez G, Whear O, Roca A G, Hussain S, Timmis J, Patel V, O'Grady K (2013) J. Phys. D: Appl. Phys. **46**:312001

Varadan V K, Chen L and Xie J (2008) Magnetic Nanoparticles. Chapter 3 in *Nanomedicine: Design and Applications of Magnetic Nanomaterials, Nanosensors and Nanosystems*. Wiley

Verwey E J W. Overbeek J Th G (1948) *Theory of the stability of lyophobic colloids*, Amsterdam: Elsevier

Wang C, Xu C, Zeng H, Sun S (2009) Adv. Mater. **21**:3045-3052

Warner C L, Addleman R S, Cinson A D, Droubay T C, Engelhard M H, Nash M A, Yantasee W, Warner M G (2010) ChemSusChem. **3**:749-757

Weizenecker J, Gleich B, Rahmer J, Dahnke H, Borgert J (2009) Phys. Med. Biol. **54**:L1 – L10

Wilhelm C, Billotey C, Roger J,Pons J N, Bacri J-C, Gazeau F (2003) Biomaterials **24**:1001-1011

Xu Y-H, Wang J-P (2008) Adv. Mater. **20**:994-999

Yi Y, Zhang Y, Wang Y, Shen L, Jia M, Huang Y, Hou Z, Zhuang G (2014) Nanoscale Res. Lett. **9**:27

Yu M, Huang S, Yu K J, Clyne A M (2012) Int. J. Mol. Sci **13**:5554-5570

Zhang S, Chen X, Gu C, Zhang Y, Xu J, Bian Z, Yang D, Gu N (2009) Nanoscale

Res. Lett. **4**:70–77

Zhang Y, Kohler N, Zhang M (2002) Biomaterials **23**:1553–1561

Zhen G, Muir B W, Moffat B A, Harbour P, Murray K S, Moubaraki B, Suzuki K, Madsen I, Agron-Olshina N, Waddington L, Mulvaney P, Hartley P G (2011) J. Phys. Chem. C **115**:327–334